How small deviations in kinematics and body form dictate muscle performances in the finely tuned avian downstroke

Marc E. Deetjen[1], Diana D. Chin[1], Ashley M. Heers[1,2], Bret W. Tobalske[3], David Lentink[1,4*]

[1]*Department of Mechanical Engineering, Stanford University, Palo Alto, CA, USA.*

[2]*Department of Biological Sciences, California State University, Los Angeles, CA, USA.*

[3]*Division of Biological Sciences, University of Montana, Missoula, MT, USA.*

[4]*Faculty of Science and Engineering, University of Groningen, The Netherlands.*

[*]Corresponding author: David Lentink d.lentink@rug.nl

Keywords: animal locomotion, flight, muscle, work loop, aerodynamic force, wing kinematics

Subject area in eLife: Ecology

Impact statement: Doves improve their wingbeat efficacy without elevating maximum pectoralis power by angling their wings mid-downstroke to efficiently generate aerodynamic force while simultaneously tensioning the supracoracoideus tendon to assist the upstroke.

Abstract

Avian takeoff requires peak pectoralis muscle power to generate sufficient aerodynamic force during the downstroke. Subsequently the much smaller supracoracoideus recovers the wing during the upstroke. How the pectoralis work loop is tuned to power flight is unclear. We integrate wingbeat-resolved muscle, kinematic and aerodynamic recordings *in vivo* with a new mathematical model to disentangle how the pectoralis muscle overcomes wing inertia and generates aerodynamic force during takeoff in doves. Doves reduce the incidence of their wing mid-downstroke to efficiently generate aerodynamic force, resulting in an aerodynamic power dip, that allows transferring excess pectoralis power into tensioning the supracoracoideus tendon to assist the upstroke—improving the pectoralis work loop efficiency simultaneously. Integrating extant bird data, our model shows how the pectoralis of birds with faster wingtip speed need to generate proportionally more power. Finally, birds with disproportionally larger wing inertia need to activate the pectoralis earlier to tune their downstroke.

Introduction

Understanding how birds use their flight muscles to power slow flight is key to understanding their biomechanics and movement ecology, as well as skeletal muscle performance in general. During slow flight, negligible lift is induced by forward body motion, so instead, almost all the aerodynamic force is generated by the flapping motion of the wings. Hence, slow flight is one of the most energetically expensive modes of locomotion [1]–[4]. Furthermore, in generalist birds the downstroke muscle, the pectoralis, is of primary importance energetically: it is the largest muscle in the avian body. It exceeds the runner-up, the supracoracoideus, by a ratio of 4:1 to 5:1 [5]. Considering the pectoralis dominates power production during the stroke of the avian forelimb—in contrast to the distributed muscle groups that typically move vertebrate limbs [6], [7]—studying avian pectoralis function in isolation serves as an ideal model system for understanding peak skeletal muscle performance. Finally, mastering the first few downstrokes during takeoff represent critical steps towards full flight in both fledgling birds and avian precursors, so better understanding the factors which dictate how the downstroke of an adult bird functions can inform our understanding of the development of avian flight.

Because of the multifaceted importance of pectoralis function, much prior research has been conducted to measure the time-resolved power produced by this muscle *in vivo*. However, technological limitations have left our understanding incomplete [2], [3], [5], [8]–[13]. Measurements of both muscle stress and strain are needed to directly measure pectoralis power. However, the pectoralis has a broad

origin with a complex arrangement of muscle fibers, making global measurement of muscle fiber strain challenging. The current state-of-the-art recordings in birds measure muscle length changes with sonomicrometry [9], [12]. To measure muscle stress, the state-of-the-art solution is to attach a strain gauge to the deltopectoral crest (DPC), which is located where the pectoralis inserts on the humerus [3], [5], [8], [9], [14]. However, pull calibrations to correlate bone strain to muscle stress are complicated by multiple factors. One source of skew is misalignment between the changing pull axis of the muscle through the stroke *in vivo* and the pull axis of the force transducer used for the pull calibration *post mortem* [5], which was refined by Jackson and Dial [10]. Another calibration method for correlating muscle power with aerodynamic and inertial power integrated over a wingbeat cycle, relies on highly simplified aerodynamic models [15]. An *in vitro* alternative relies on electrical stimulation of bundles of muscle fibers [2], [16], but the heterogenous composition of the pectoralis leads to variability [17], and *in vivo* validation is lacking. Hence, fundamental questions about *in vivo* muscle function remain [18].

In contrast to the muscle architecture of large pectoralis muscle, which is well-suited for producing work to flap the wing, the function of its antagonist muscle, the supracoracoideus, is more ambiguous. It has pennate muscle fibers attached to a long tendon, making it better suited for producing force than work, which would facilitate storing and releasing significant amounts of elastic energy in the supracoracoideus tendon [19]–[22]. Measurements in pigeons (*Columba livia*) suggest this elastic storage may range between 28 and 60% of the net work of the supracoracoideus [5], which is thought to primarily elevate and supinate the wing. However, while the supracoracoideus is used in every flight mode [23], [24], birds are still able to takeoff without its use [25], [26]. In summary, how the avian flight apparatus moves the wing by tuning pectoralis and supracoracoideus muscle and tendon power release—to generate the net aerodynamic force required for flight—has yet to be resolved.

To resolve how the avian pectoralis work loop is tuned to generate aerodynamic force, we combine established *in vivo* muscle strain and activation measurement techniques with our new *in vivo* high-speed 3D shape reconstruction and aerodynamic force measurement techniques (Fig. 1), which we integrate with a new mathematical model derived from first principles. We used our high-speed, structured-light technique [27], [28] to 3D-reconstruct wing morphology, and we directly measured horizontal and vertical aerodynamic forces using our aerodynamic force platform (AFP) [29]–[33]. We simultaneously measured the time-resolved pectoralis activation and strain *in vivo* using electromyography and sonomicrometry [3] because no other reliable techniques were available and it is considered minimally invasive, especially compared to muscle stress recordings. Working within the constraints of our 3D-reconstruction technique, we focused on the second downstroke after takeoff,

because it was the first downstroke that well supported body weight after takeoff. First, we computed the time-resolved power and torque that the flight muscles need to sustain to overcome wing inertia and generate aerodynamic force. To account for elastic storage and understand how variations in the magnitude and timing of elastic storage in the supracoracoideus tendon would affect power generation in the pectoralis and supracoracoideus muscles, we derived a muscle mechanics model from first principles to integrate our *in vivo* data. Finally, we used our new integrative biomechanics model of the dove downstroke to gain comparative insight into muscle function by examining how it scales across species and can explain avian flight muscle functionality generally.

Results

Effects of angle of attack on aerodynamic power

During the second wingbeat we find there is a dip in the angle of attack during the middle of the downstroke when peak aerodynamic force is generated. This angle dip coincides with a peak in the power factor, the non-dimensional square root of lift-cubed to drag-squared ratio, which minimizes the aerodynamic power required to generate lift. During the downstroke, the angle of attack across the span of the wing (Figs. 2C, S4A) starts and end with peaks with a valley in-between: the first peak (54.0° ± 5.0°) is reached after 7.1% of the stroke and the second peak (68.4° ± 12.1°) is reached at 49.4% of the stroke (which corresponds to 10.9% before the end of the downstroke), with a large dip (30.5° ± 3.1°) in the middle at 27.7% of the stroke. Our aerodynamic force recordings show this dip in mid-downstroke angle of attack corresponds with a mid-downstroke dip in wing drag and peak in net aerodynamic force (Fig. 3B). Comparing the angle of attack (Fig. 2C) with the power factor (Fig. 3C) of the doves during the downstroke, the power factor peak (timing after start of downstroke: 29.8% of the stroke) corresponds to the mid-downstroke angle of attack dip. Of the two peaks in drag (Fig 3B), the second peak after the mid-downstroke dip is larger (drag peak scaled by bodyweight before mid-downstroke dip: 0.92 ± 0.22; after: 1.60 ± 0.46). This is caused by two factors: the corresponding angle of attack is higher and the wing area is larger. Examining the directional components of lift and drag, we find the dove primarily uses lift for weight support (stroke-averaged vertical aerodynamic force scaled by bodyweight for lift: 66.17% ± 10.81%; drag: 22.11% ± 4.62%). The secondary function of lift is to overcome drag (stroke-averaged horizontal aerodynamic force scaled by bodyweight for lift: 32.84% ± 9.96%; drag: -27.64% ±

4.64%). Drag primarily points backwards throughout the downstroke, and laterally at the beginning and end of the downstroke (the lateral forces of the wings cancel). Due to the small peaks in drag before and after the mid-downstroke dip, drag contributes to weight support at the beginning and end of the downstroke, so both lift and drag contribute to weight support during take-off. Finally, during the upstroke the dove folds its wings inward (Fig. 2D,E), producing very little aerodynamic force (aerodynamic force generated during upstroke scaled by bodyweight vertically: 11.28% ± 2.81%; horizontally: 2.68% ± 1.49%).

Due to the mid-downstroke dip in drag, there is a corresponding dip in aerodynamic power (Fig. 4A), because only the drag and wing velocity contribute to aerodynamic power (Eqn. S17). The dip in aerodynamic power is less pronounced than the dip in drag, because it corresponds with a peak in wing speed, but the uneven adjacent peaks remain (peak in aerodynamic power scaled by pectoralis mass before mid-downstroke dip: 513.0 ± 176.1 W/kg; after: 719.1 ± 175.0 W/kg; minimum dip: 460.4 ± 176.1 W/kg). This mid-downstroke dip in total aerodynamic power also corresponds to a dip in the lateral component of power, so that during mid-downstroke, the primary contribution to aerodynamic power is associated with the horizontal component of drag (Fig. S5A) due to the forward movement of the wing (Fig. 2F). As expected, the largest contribution to aerodynamic force is in the vertical direction (Fig. 3A), yet when it comes to aerodynamic power the vertical contribution is the smallest. This is because lift is much larger than drag in the vertical direction (Fig. S5C), and only overcoming drag requires aerodynamic power (per the definition of lift and drag with respect to velocity).

Overall, we find that peak aerodynamic force production occurs midstroke when drag attains a local minimum, causing a peak in efficiency (highest power factor).

Inertial versus aerodynamic power

Aerodynamic power dominates during the downstroke, whereas inertial power dominates the upstroke (Fig. 4B; Table S5). However, we observe inertial power evens out the two peaks in aerodynamic power adjacent to the mid-downstroke dip (peak in aerodynamic + inertial power scaled by pectoralis mass before mid-downstroke dip: 537.0 ± 221.5 W/kg; after: 580.0 ± 176.8 W/kg; minimum dip: 455.0 ± 287.0 W/kg). Whereas for the aerodynamic power the difference in the peaks is 206.1 ± 248.3 W/kg, with the addition of inertial power the difference in peaks reduces to 43.0 ± 283.4 W/kg.

Effects of elastic storage in the supracoracoideus tendon

We use our time-resolved muscle model to understand the effect which the amount and timing of elastic storage in the supracoracoideus tendon has on power generation in the pectoralis and supracoracoideus muscles (Fig. 5).

Varying elastic storage fraction in the supracoracoideus tendon reveals the power needed to tension the supracoracoideus tendon is small in comparison to the power generated by the pectoralis during the downstroke (Figs. 5, S7, Table S5). The pectoralis would need to generate 206.0 ± 49.6 W/kg (stroke-averaged positive power scaled by pectoralis mass) if no energy was stored in the supracoracoideus tendon. An increase of 24.9% ± 17.5% power generation in the pectoralis to store elastic energy during the downstroke (to 255.9 ± 62.7 W/kg) would be sufficient to fully power the upstroke. Storing only a fraction mid-downstroke muscle work instead is still sufficient to partially power the upstroke (Fig. S7Q,R). While our measurements and analysis cannot be used to deduce the energy storage fraction directly, anatomy [5], [19]–[22] and a direct measurement of the strain in the tendon [5], indicate a non-zero elastic energy storage fraction. Applying a storage fraction of 28-60% as measured in [5] to our model requires only an increase in pectoralis work of between 6.8% and 14.5%. Hence, elastic storage in the supracoracoideus tendon appears to be an effective solution to power the upstroke that simultaneously smooths the mid-stroke power output of the pectoralis.

Modelling variation in the timing of energy storage in the supracoracoideus tendon, we find that fine-tuning the timing improves the shape of the pectoralis work loop (Figs. 5, S8). Short storage time (Fig. 5C), results in a spike in pectoralis power near the end of the downstroke, which produces a low pectoralis work loop shape factor (Fig. 5E shape factor: 0.49 ± 0.14; see Fig. 5G for trends). On the other hand, when the storage time is appropriately spread out over the downstroke (Fig. 5D), the pectoralis work loop shape factor increases to a maximum value of 0.73 ± 0.11. While this maximum shape factor is achieved when the energy storage in the supracoracoideus tendon equals 90%, a shape factor of over 0.72 ± 0.11 can be achieved for any energy storage over 35% (Fig. 5F-G). For any energy storage over 35%, the maximum shape factor corresponds to a storage time of 31% of the stroke. The reason for this is related to the mid-downstroke dip in required muscle power (Fig. 4B) originating from the mid-downstroke dip in angle of attack and drag (Fig. 2C). When the energy storage in the supracoracoideus tendon is appropriately spread out during the downstroke, the peak in extra pectoralis power needed for tensioning overlaps with the dip in required muscle power from aerodynamic and inertial power. Hence, storing energy in the supracoracoideus tendon for 31% of the stroke has the effect of flatting out the mid-downstroke pectoralis power generation and improving the shape factor. Since a mid-

contraction dip in power generation is unnatural for muscles, tensioning the supracoracoideus tendon is key for proper wing stroke kinematics: instead of the wing continuing to accelerate mid-downstroke when velocity peaks, the wing reaches zero acceleration at this point, after which it decelerates to prepare for stroke reversal.

Directionality of pectoralis pulling on the humerus

Thus far we have focused on power, which is a one-dimensional parameter, but in order to determine in what direction the pectoralis needs to pull on the humerus to effectively flap the wing, we need to expand our analysis to moments (torques) in three dimensions (Fig. 6).

As is the case for the power analysis, aerodynamic moments dominate during the downstroke, whereas inertia dominates during the upstroke and near stroke reversal (Fig. S10). Additionally, an in-depth analysis of the three components of the aerodynamic contribution to muscle torque (see Section S3), shows that the components of lift and drag in the vertical world-coordinate direction are dominant.

By combining the required muscle moment with the position of the humerus time-resolved, we can analyze the direction that the pectoralis pulls on the humerus during the downstroke (Fig. 6D-E). For this we assume that the muscle moment is primarily generated by the pectoralis, although this is likely not entirely true if the supracoracoideus tendon is tensioned during the mid-to-late portion of the downstroke. Under this assumption, for the entire downstroke, in the mediolateral direction, the pectoralis pulled medially (Fig. 6D). Additionally, at the beginning of the downstroke, the pectoralis pulled in the cranioventral direction, and at the end of the downstroke, the pectoralis pulled in the caudodorsal direction.

Scaling analysis across extant birds

Based on scaling the gross parameters related to aerodynamic power, we modeled a scaling relationship to predict average pectoralis power across extant birds (Fig. 7A,C). We predict that average pectoralis power, ${}^{\mathrm{N}}\overline{P}^{\mathrm{pect}}$, divided by bodyweight, m_{body}, scales linearly with flapping frequency, f, and wingspan, $\left|\vec{\mathbf{r}}_{\mathrm{span}}\right|$ (from the shoulder joint to the wingtip):

$$\frac{{}^{\mathrm{N}}\overline{P}^{\mathrm{pect}}}{m_{\mathrm{body}}} = -0.59 + 18.74\left(f\left|\vec{\mathbf{r}}_{\mathrm{span}}\right|\right). \tag{1}$$

To compare the effects of aerodynamics and inertia on muscle power during the downstroke, we modeled a separate scaling relationship to predict the required timing of pectoralis power across

extant birds (Fig. 7B,D). Although inertial power does not contribute to average muscle power across the downstroke, because the positive and negative inertial power cancels, it does have the effect of shifting the distribution of required muscle power earlier in the stroke. Hence, for birds where the ratio of inertial to aerodynamic power is higher, the pectoralis muscle needs to provide power earlier in the downstroke. Quantitatively we predict that the midway point of the pectoralis power exertion, $T_{\mathrm{P,mid}}^{\mathrm{pect}}$ (Eqn. S75; percentage of stroke), equals:

$$T_{\mathrm{P,mid}}^{\mathrm{pect}} = 35.01 - 61.75\left\{\frac{m_{\mathrm{wing}}}{m_{\mathrm{body}}}\left(\frac{r_{\mathrm{gyr}}}{\left|r_{\mathrm{span}}\right|}\right)^{2}\left(f\left|r_{\mathrm{span}}\right|\right)f\right\}, \tag{2}$$

where m_{wing} is the mass of the wing, and r_{gyr} is the radius of gyration of the wing. A similar relationship holds for the midway point of the pectoralis force exertion, $T_{\mathrm{F,mid}}^{\mathrm{pect}}$ (Eqn. S76; percentage of stroke):

$$T_{\mathrm{F,mid}}^{\mathrm{pect}} = 31.90 - 59.06\left\{\frac{m_{\mathrm{wing}}}{m_{\mathrm{body}}}\left(\frac{r_{\mathrm{gyr}}}{\left|r_{\mathrm{span}}\right|}\right)^{2}\left(f\left|r_{\mathrm{span}}\right|\right)f\right\}. \tag{3}$$

Across a wide range of bird sizes (between 9.5 grams and 2140 grams), the variation in predicted pectoralis timing is small. Pectoralis midway power timing, $T_{\mathrm{P,mid}}^{\mathrm{pect}}$, falls between 23.0% and 32.7% and force timing, $T_{\mathrm{F,mid}}^{\mathrm{pect}}$, falls between 20.6% and 29.6%.

Discussion

Effects of angle of attack and energy storage on muscle performance

By holistically measuring the avian stroke, we provide novel insight into connections between flapping kinematics and the performance of flight muscles and tendons. Surprisingly, we find that in the region of the stroke where peak aerodynamic force occurs (Fig. 3A), aerodynamic power dips (Fig. 4A). This is because during mid-downstroke, the doves pronate their wings to reduce angle of attack (Fig. 2C), which results in a local minimum in drag combined with maximal lift (Fig. 3B), resulting in peak power factor (Fig. 3C). Furthermore, because aerodynamic power, and hence required total muscle power, dips mid-downstroke (Fig. 4B), the pectoralis power can be allocated to tension the supracoracoideus tendon, which simultaneously improves the pectoralis work loop shape factor (Fig. 5). This improved shape

factor flattens the dip in pectoralis power mid-downstroke (Fig. 5D). Consequently, the work loop is more rectangular (Fig. 5E): producing more total work at a more constant maximum power output level. Additionally, since a mid-contraction dip in power generation is sub-optimal for muscle mechanics [34], tensioning the supracoracoideus tendon is the most parsimonious interpretation of how our experimental and model outcomes can corroborate the generation of proper wing stroke kinematics. Specifically, instead of the wing continuing to accelerate mid-downstroke when velocity peaks, elastic energy storage in the supracoracoideus tendon enables the wing to reach zero acceleration midstroke, as kinematically required, after which the wing decelerates to prepare for stroke reversal. Finally, the efficient low angle-of-attack mid-downstroke facilitates energy storage in the supracoracoideus tendon, which is an energy-effective solution for powering the upstroke that simultaneously enables the pectoralis to generate work more efficiently—showing how the downstroke apparatus of doves benefits from being finely tuned.

The dove's mid-downstroke dip in angle of attack (30.5° ± 3.1°) has a cascading effect on drag, aerodynamic power, and energy storage that is especially pronounced compared to other species. For example, in parrotlets the mid-downstroke angle of attack is higher, roughly between 45° and 60° [27], under similar take-off conditions for the second wingbeat. In contrast, in barn owls flying at higher speeds after take-off, the angle of attack mid-downstroke is lower, roughly 30° at 5-6 m/s flight speed [35]. A comparison with hovering birds is more representative, because the advance ratio (ratio of forward flight speed to wingtip speed) of the doves during takeoff is 0.14 ± 0.01, which is close to hovering (advance ratio < 0.1 [36]). For this we harness data of other specialized flying vertebrates capable of sustained or short hovering flight: hummingbirds and small nectar and fruit bats [37]. The angle of attack of the doves is most similar to that of hovering hummingbirds, whose angle of attack is 36.9° ± 4.9° (across n = 88 individuals from 17 species) during mid-downstroke, with peaks at the beginning (51.3° ± 10.9°) and end (52.7° ± 9.9°) of the downstroke [37], notably the mid-downstroke dip is flatter for hummingbirds. In contrast the average mid-downstroke angle-of-attack in hovering bats is 52.2° ± 5.0° (across n = 16 individuals from two nectar and one fruit bat species, of which the latter has the highest angle-of-attack, [37]). Notably the bat's angle-of-attack trace-shape is more similar to that of doves. Based on our literature comparison we find that the recorded downstroke angle-of-attack of doves falls between the measurements reported for other species flying at similar speeds, with the exception of the dove's pronounced dip during the mid-downstroke. Before more species are studied with high-resolution methods, we cannot attribute this pronounced dip in angle-of-attack as a dove-specific specialization, hence we focus on the muscle-mechanical consequences of this wingbeat-

adaptation found in the dove. The immediate effect of this dip in angle of attack is a corresponding peak in power factor (non-dimensional lift$^{3/2}$ to drag ratio). This matches our expectation based on measurements of hummingbird wings (maximum power factor of 4.35 at 27.7° angle of attack [38]) and pigeon wings (maximum power factor of 6.41 at 30.2° angle of attack [39]). For both species, the power factor monotonically decreases at angles of attack greater than 26 degrees. The angle of attack is hence a critical factor that has a cascading effect on downstroke flight-apparatus tuning: the mid-downstroke dip in angle of attack causes a dip in drag combined with a peak in lift, resulting in peak power factor and a corresponding local minimum in aerodynamic power. Combined with the simultaneous local minimum in inertial power, this explains the local minimum in total required pectoralis power output mid-downstroke at a muscle length for which power output should ideally peak [34].

To comprehensively understand the functional consequence of tuning the downstroke, we use our muscle model to compute bounds on dove pectoralis power with and without elastic storage in the supracoracoideus tendon. Comparison with a variety of studies across species [2], [3], [5], [9]–[13], [40] reveals a wide scatter of estimated pectoralis power (Fig. S13). Some differences may be attributed to different flight modes and specie-specific adaptations, but the variance from measurement techniques also likely contributes. From the studies which vary flight speed [2], [3], we see that flight is more expensive at low speeds (percentage increase in power at lowest measured speed compared to minimum power at any speed for zebra finch: 90.9%, budgeriagar: 94.9%, cockatiel: 89.9%, dove: 45.2%, magpie: 142.5%) and at high speeds (percentage increase in power at highest measured speed compared to minimum power at any speed for zebra finch: 68.3%, budgeriagar: 47.5%, cockatiel: 214.1%, dove: 90.0%, magpie: 50.8%). However, this cannot explain the scatter between studies for the same species. For example, for three studies of pigeons at similar speeds (5.0 ± 0.5 m/s), the average positive pectoralis power scaled by pectoralis mass was 108 W/kg [9], 207 W/kg [12], and 273 W/kg [40], and for three studies of magpies at similar speeds (4.2 ± 0.3 m/s), the average pectoralis power was 68 W/kg [3] (net power), 85 W/kg [11] (positive power), and 308 W/kg [10] (net power). Many of these previous studies were limited by high-variance calibrations of muscle stress [10], so our more sophisticated external power measurement gives valuable insight, which can be used to anchor the pectoralis power estimate for doves. The only comparable study for doves is Tobalske *et al.* 2003 [3], which reports an average net pectoralis power of 179 W/kg for doves flying at 1 m/s. We measured an average net pectoralis power of between 182 ± 48 W/kg (no energy storage) and 232 ± 60 W/kg (full energy storage) for doves flying at 1.23 ± 0.13 m/s, meaning that, based on our measurements, Tobalske *et al.* 2003 [3] underestimated the pectoralis power by between 1.6% ± 26.6% (no elastic storage) and

277 29.4% ± 33.3% (elastic storage fully powers upstroke), which is small in comparison to the variance
278 among other studies. While we cannot, from the current measurements, determine exactly how much
279 energy is actually stored for upstroke, we can observe that utilizing energy storage in the
280 supracoracoideus tendon is an effective solution for powering the upstroke, partially because only a
281 small increase (24.9% ± 17.5%) in pectoralis power is needed for elastic storage to obtain a well-tuned
282 wingbeat.

283 A notable benefit of energy storage in the supracoracoideus tendon, is that it also improves the
284 shape factor of the pectoralis work loop. We find that for any energy storage fraction in the
285 supracoracoideus tendon above 35%, a pectoralis work loop shape factor of over 0.72 ± 0.11 can be
286 achieved (global maximum of 0.73 ± 0.10) if the energy storage is spread out appropriately over the
287 course of the downstroke (Fig. 5F-G). Compared to work loops previously reported from strain-gauge
288 measurements of muscle stress, which are relatively triangular (data from Tobalske et al. 2003 is plotted
289 in Fig. 5E for a dove in similar conditions; shape factor = 0.62 [3]) [10], our more rectangular work loops
290 suggest an improved generation of work, because the relative area of positive work is greater for a
291 rectangle than a triangle with the same maximum stress and strain.

292 We find additional evidence for energy storage in the supracoracoideus tendon based on the
293 computed pull direction of the pectoralis during the downstroke (Fig. 6). In particular, during the second
294 half of the downstroke, the pull angle (Fig. 6C) and pull direction (Fig. 6D-E) of the pectoralis would more
295 closely match previously-measured kinematics in chukars for wing-assisted incline running [4], if the
296 supracoracoideus tendon was tensioned in that region of the wing stroke. While we should not expect
297 the chukar kinematics to exactly match our results, as they originate from a different species and
298 behavior (i.e. level flight *versus* wing-assisted incline running), the pull angle and direction do align well
299 in the first half of the downstroke, which was unaffected by supracoracoideus tendon tensioning. In the
300 second half of the downstroke, which could be affected by tensioning the tendon, the pectoralis of the
301 chukars pulled in a caudoventral direction, whereas our measurements of the total flight muscle torque
302 indicate a caudodorsal pull direction. Similarly, the pull angle of the pectoralis on the humerus generally
303 agrees with the chukar kinematics in the first half of the downstroke, but diverges in the second half of
304 the downstroke. Tensioning the tendon may explain both of these discrepancies because, firstly, the
305 anatomy of the supracoracoideus makes it well positioned to produce a dorsal force near the end of
306 downstroke, whereas this is impossible for the pectoralis. Secondly, if tensioning the supracoracoideus
307 tendon increased the required pectoralis moment in the second half of the downstroke, then the
308 pectoralis pull angle would be higher than is plotted in Fig. 6C. While elastic tensioning of the

309 supracoracoideus tendon seems likely [5], future work measuring the supracoracoideus pull angle and
310 direction is needed to verify these predictions. Additional future work could measure the heterogeneous
311 recruitment of the muscle fibers in the pectoralis through the downstroke to refine the muscle moments
312 and stresses we calculated here.

313 Overall, we see multifaceted evidence and benefits of extra pectoralis power production during
314 the mid-to-late downstroke to tension the supracoracoideus tendon, which can then power much of the
315 upstroke. In addition to reducing the work that the supracoracoideus muscle needs to produce, energy
316 storage in the tendon enhances the pectoralis work loop shape, due to efficient aerodynamic force
317 production mid-downstroke, caused by a dip in the angle of attack. Elastic storage also enables the
318 pennate supracoracoideus to generate force instead of power, for which its muscle fiber architecture is
319 more suited. The interactions between kinematics and muscle activity are critical to understanding bird
320 flight, hence it is valuable to study how it shifts for birds with different morphologies and flight styles.
321

322 Comparative effects of wing aerodynamics and inertia in extant birds

323 For doves, aerodynamic power is dominant during the downstroke, and the smaller inertial power
324 dominates during the upstroke.

325 In contrast, hummingbirds produce a similar amount of aerodynamic power during upstroke and
326 downstroke (Fig. S14A), and inertial power is dominant throughout the stroke (Fig. S14B). The increased
327 influence of inertia is likely due to the higher wingbeat frequency of the hummingbirds (79 Hz; [13]) as
328 compared to the doves (9.8 Hz; Table 2). Unsurprisingly, the masses of the pectoralis and
329 supracoracoideus muscles are more similar in hummingbirds (approximately 2:1 ratio [13]) than doves
330 (ratio of 4.60 ± 0.93), because hummingbirds need more total muscle power during the upstroke than
331 doves (Fig. S14C).

332 However, for bird species with more similar flying styles, the differences in muscle function and
333 timing are more nuanced. Based on our scaling analysis, we find that average pectoralis power scaled
334 linearly with bodyweight and wingtip speed (Fig. 7A,C; Eqn. 1). This helps to explain why flapping
335 frequency and wingspan are inversely related across species [41]: to maintain a reasonable average
336 muscle power requirement, birds with longer wings need to flap slower. The effect of inertia on the
337 other hand, is to impact the timing of the pectoralis power, even while the average pectoralis power is
338 unaffected (Fig. 7B,D; Eqn. 2). When the effects of inertia relative to aerodynamics are increased (higher
339 wing to body mass ratio, wing mass more distally positioned, higher flapping frequency, longer wing
340 length), pectoralis power needs to be produced earlier in the downstroke. Across over three orders of

magnitude of extant bird sizes (between 9.5 grams and 2140 grams), the timing shift is small, covering a range of less than 10% of the stroke. Hence, it is difficult to determine whether previous studies measuring electrical activation timing of the pectoralis confirm this result (Fig. 7D). However, based on our detailed mechanistic analysis, we have built new intuition for why pectoralis power (and force) should in principle be timed slightly earlier or later to tune the downstroke well. Overall, the interplay between kinematics and wing physiology is a critical factor in determining muscle function, and across a vast array of bird species with similar flight styles, the variance in timing and relative magnitude of muscle power production is small, and thus hard to measure, but functionally relevant.

Conclusions

Our integration of *in vivo* measures of muscle activation and strain using established methods combined with novel measures of wing shape and aerodynamic force provides new insight into how the complex interplay between inertia and aerodynamics shapes wing kinematics and muscle function. While the inertial power for doves is less than the aerodynamic power, inertia plays a critical role in dictating pectoralis power production timing and dominates the required power during the upstroke. This upstroke muscle power requirement can be met by the pectoralis muscle storing elastic energy in the supracoracoideus tendon during the mid-to-late downstroke so it can be released during the upstroke. Counterintuitively, when fine-tuned correctly, this extra power production to tension the supracoracoideus tendon actually improves the effectiveness of the pectoralis muscle work loop by maximizing its work loop shape factor. Storing energy by tensioning the supracoracoideus tendon mid-downstroke effectively flattens pectoralis power production, because it fills the aerodynamic power dip due to the marked reduction in angle of attack midstroke, which improves the aerodynamic efficiency of the wing. Future studies should seek to simultaneously measure contractile behavior in the supracoracoideus [5] and the strain in its tendon to provide direct tests of our predictions of elastic energy storage. This feat has not yet been performed in bird flight because the supracoracoideus tendon cannot be studied minimally invasively, underscoring the value of our corroborated model. Additionally, it would be valuable for a complete picture of whole-animal energetics to have measures of metabolic power [42] to compare it with muscle and aerodynamic power to determine avian flight efficiency.

Materials and Methods

Dove flight experiments

The experimental setup (Fig. S1) consisted of three time-synchronized systems which imaged the 3D surface of the dove (Fig. 1C), measured the aerodynamic forces produced by the dove (Fig. 1A,B), and measured the activation and lengthening of the pectoralis muscles of four doves (Fig. 1A,B). To image the 3D wing surface of each dove at 1000 Hz, we used a structured-light system [27], [28]. We measured the vertical and horizontal aerodynamic forces produced by the dove at 2000 Hz using an aerodynamic force platform [31], [43] (AFP). Finally, sampling at 10,000 Hz, we used electromyography (EMG) to measure the electrical activation of the pectoralis and sonomicrometry to measure the strain of the pectoralis. We analyzed the second wingbeat after takeoff for four 2-year-old near-white Ringneck doves (*Streptopelia risoria*; 3 males, 1 female; statistics summarized in Table 1), which were trained to fly between perches (1.6 cm diameter) 0.65 m apart inside of the AFP. We recorded 5 flights from each dove while measuring the muscle activity for a total of 20 flights. To assess the effect of surgery and the recording cable on flight behavior, we also recorded doves 3 and 4 during five pre-surgery flights, and dove 3 during five post-surgery flights, but without the cable needed to measure muscle activity attached (Fig. S2). The perches were mounted 0.36 m above the bottom plate of the AFP, and the residual descent angle between the takeoff and landing perch was 2 degrees. Training involved light tapping on the tail to initiate a flight to the other perch. Some flights were rejected as outliers due to inaccurately eliciting a flight or equipment failure (noisy or missing sonomicrometry signal; insufficient suspended cable length allotment). All experiments were approved by and in accordance with Stanford University's Institutional Animal Care and Use Committee.

Muscle activation and strain measurements

To measure the electrical activation and strain of the left and right pectoralis muscles, we surgically implanted EMG electrodes and sonomicrometry crystals using standard methods for the pectoralis of birds [9], [44]. Recordings were made by connecting a shielded cable to the back plug on the dorsal side of the dove. We loosely suspended the cable, weighing approximately 26.1 g, above the dove (Fig. S1). Sonomicrometry signals were converted into fiber lengths, $L_{\mathrm{pect,f}}$, by calibrating at 0, 5, and 10 mm, which we used to compute fiber strain:

401 $$\gamma_{\text{pect,f}} = \frac{L_{\text{pect,f}}}{L_{\text{pect,f,rest}}} - 1, \quad (4)$$

402 where $L_{\text{pect,f,rest}}$ is the muscle's resting length during perching. For more information, see Section S4.

403

404 ## Aerodynamic force measurements

405 We determined the time-resolved aerodynamic force vector generated by each wing of the dove by
406 measuring the net aerodynamic forces in the horizontal (back to front; x) and vertical (z) directions as in
407 Deetjen et al. 2020 [33] (Figs. 1A,B, S1). We then combined these 2D forces with our 3D wing kinematics
408 measurements to reconstruct the final, lateral (right to left), component of the full 3D force vector (Fig.
409 1C). The vertical and horizontal aerodynamic forces of the dove were measured using a 2D AFP [31],
410 [43]. The 2D AFP measures vertical forces by instrumenting the floor and ceiling of a flight chamber with
411 carbon fiber composite panels. Similarly, the horizontal forces are measured with two instrumented
412 panels on the front and back sides of the flight chamber (1 m length × 1 m height × 0.6 m width). Each of
413 the four panels is connected in a statically determined manner to three Nano 43 sensors (six-axis, SI-9-
414 9.125 calibration; ATI Industrial Automation) sampling at 2000 Hz with a resolution of 2 mN. We also
415 measured takeoff and landing forces by mounting the perches on carbon fiber beams, each of which
416 was connected in a statically determined manner to three Nano 43 sensors set on mechanically isolated
417 support structures. The force measurements were filtered using an eighth-order Butterworth filter with
418 a cutoff frequency of 80 Hz for the plates and 60 Hz for the perches, or about 8 and 6 times the flapping
419 frequency of a dove, respectively. This enabled us to filter out noise from the setup, because the natural
420 frequencies of the force plates were all above 90 Hz, and the perches had natural frequencies above 70
421 Hz. Validation of the setup is detailed in Section S5.

422

423 ## 3D surface and kinematics measurements

424 We measured the 3D surface of the head, tail, and left wing of the dove, as well as multiple marker
425 points on the dove at 1000 Hz using the same methods as described in our methods paper: Deetjen et
426 al. 2020 [33]. The 3D surface of the dove (Fig. 1C) was reconstructed using our automated structured
427 light method [27] (five cameras and five projectors calibrated together using our automated calibration
428 method [28]). We decreased the sampling speed (from 3200 Hz in [27]) and thickened the projected
429 stripes to improve lighting contrast to converge on the recording setup settings described in [33].
430 Additionally, we manually tracked the following 12 feature points using triangulation: ninth primary

wingtip, seventh secondary feather, shoulder, wrist, middle of the back, left and right feet, left and right eyes, tip and base of the beak, and top of the head (Fig. 1C). For the ninth primary, shoulder, wrist, back, and the top of the head, we attached square retro-reflective marker tape and identified their centers when they were visible. The remaining positions were estimated with a combination of manual annotation and interpolation, and we smoothed the 3D reconstructed points using the 'perfect smoother' [45] to reduce noise when taking derivatives. We combined the collected 12 kinematics (marker) points and the surface data to fit a smooth morphing surface to the body, tail, and wings of the dove. Finally, we assumed bilateral symmetry for the right wing because we focused our cameras and projectors on the left wing to maximize resolution.

Modeling the distributed mass of the dove

We modeled the distributed mass of the wings and body of the dove as a series of point masses which move based on the tracked kinematics. For each wing, we used 20 point masses which were distributed along the wing. We fixed the location of the shoulder joint relative to the body of the dove (average of tracked shoulder positions relative to the body) and formed a V-shaped path from the shoulder joint to the wrist joint to the ninth primary feather. The point masses were then placed proportionally along this path. The masses of each point mass were determined using a scaling of the mass distribution along the wing given by Berg [46].

Modeling power and momentum

We developed two separate dynamics models to gain different insights into the time-resolved activity of the flight muscles. The first model is a 1D power balance of the entire dove (see Section S7 for derivation), by which we compute the time-resolved power that the dove's muscles must have generated in order to produce the kinematics and aerodynamic forces that we observed. Combined with the measured pectoralis strain rate, we computed the pectoralis force magnitude during the downstroke, assuming it is the primary muscle producing power. The second model is a 3D angular momentum balance of the wing (see Section S8 for derivation), by which we compute the time-resolved 3D moment vector (torque) that must have acted on the wing in order to produce the observed kinematics and aerodynamics forces. We then used the information gained from both of these models, together with skeletal measurements, to compute the time-resolved 3D force vector produced by the pectoralis during downstroke, along with its pull angle on the humerus (see Section S9 for derivation).

462 See Fig. S11 for a side-by-side comparison and summary of the two models, and how they are used in
463 concert to compute the pull angle of the pectoralis.
464

465 Disentangling pectoralis and supracoracoideus power

466 To understand the effects that varying amounts of elastic storage in the supracoracoideus tendon would
467 have on power generation in the pectoralis and supracoracoideus muscles, we developed a time-
468 resolved muscle-tendon model. The output of this model is a breakdown of the time-resolved power
469 generated, absorbed, stored, or released by the pectoralis and supracoracoideus. The sum of these four
470 power modes across the two muscles equals the total computed muscle power at each time-step. While
471 other muscles are involved in power generation, we simplify the model by assuming that the pectoralis
472 and supracoracoideus generate all the necessary power. This assumption is justified because their
473 masses significantly exceed that of the other muscles in the dove [5]. Using this assumption, it is clear
474 that positive, mid-downstroke power can be attributed to the pectoralis, and positive, mid-upstroke
475 power can be attributed to the supracoracoideus. However, two modeling challenges remain. First,
476 during stroke-reversal, *in vivo* measurements indicate that activation of the pectoralis and
477 supracoracoideus overlaps [5], adding some ambiguity in those regions. We addressed this using
478 common-sense rules for muscle power generation: e.g. muscles only generate positive power when they
479 are shortening (see Section S10 for details). Second, the anatomy of the supracoracoideus tendon, along
480 with *in vivo* measurements, provides evidence that it stores elastic energy during the late downstroke
481 and releases it after stroke reversal to aid the supracoracoideus during upstroke [5]. Because the exact
482 nature of this energy storage is unknown, we analyzed the effect that different amounts and timing of
483 energy storage would have on power distribution (see Section S11 for details).
484

485 Scaling analysis across extant birds

486 We scaled our aerodynamic, inertial, and muscle measurements for doves across multiple extant birds,
487 to estimate comparative patterns of power output during slow flight. Assuming that aerodynamic forces
488 scale with body weight, wing velocity scales with flapping frequency times wingspan, and using our
489 derived modeling equations, we traced the effects of aerodynamics and inertia to formulate key scaling
490 parameters that dictate muscle performance. In particular, the aerodynamic power is proportional to
491 the wingtip velocity (note the force associated with aerodynamic power is proportional to bodyweight,
492 we thus do not dissect its dependence on velocity squared explicitly), and the inertial power is
493 proportional to the wing mass ratio (ratio of wing mass to bodyweight), the wing radius of gyration ratio

(ratio of radius of gyration to wingspan) squared, the wing length, and the wingbeat frequency. For more details see Section S12.

Figures

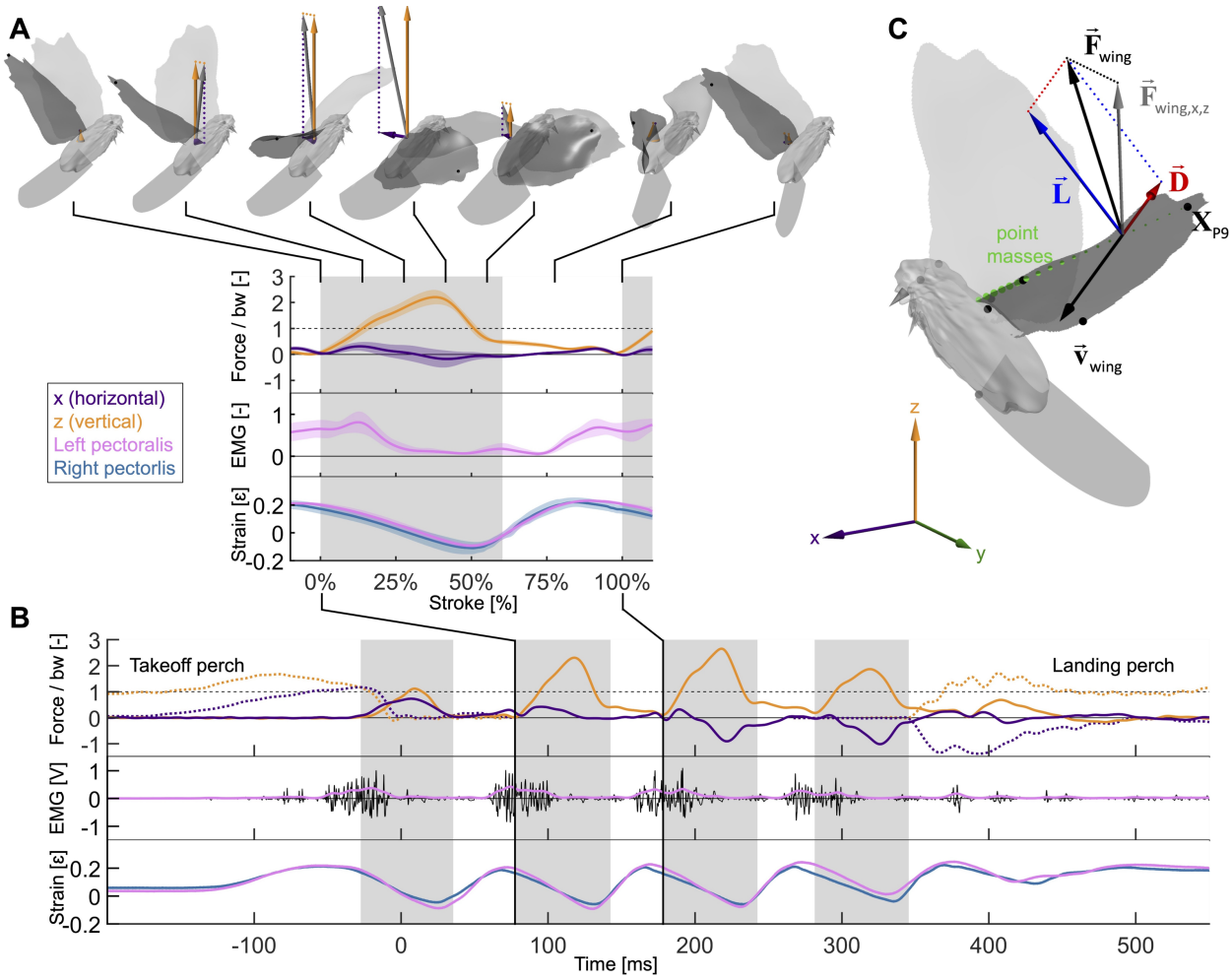

Figure 1. Wingbeat-resolved aerodynamic forces, pectoralis activation and contraction, and 3D surface reconstruction of four doves (N = 4) in slow hovering flight (n = 5). (A) Inset showing the average 2nd wingbeat ($N \times n$ = 20 flights total) net horizontal (x, purple) and vertical (z, orange) aerodynamic force, electrical activation (EMG, pink) of the left pectoralis (right pectoralis signal was unreliable), and strain of the left (pink) and right (blue) pectoralis. (Gray region: downstroke; color shaded regions: standard deviation; force normalized by bodyweight: bw; statistics and plot definitions apply to all figures unless stated differently). The dove's 3D reconstructed surface and recorded aerodynamic force during each

stroke phase (flight direction mirrored to match temporal direction). (B) The same data from A are plotted for a single representative flight from takeoff to landing. The dotted lines represent horizontal and vertical perch forces during takeoff and landing. In addition to the lowpass filtered (pink) EMG signal, the raw signal is plotted in black. (C) Using our high-speed structured-light system [27], [28], we imaged the 3D surface of the bird (right wing copied from left assuming bilateral symmetry) and generated surface fits for the dove's body and tail [33]. The total 3D aerodynamic force ($\vec{\mathbf{F}}_{\text{wing}}$, black) is the sum of the measured horizontal (x) and vertical (z) components ($\vec{\mathbf{F}}_{\text{wing,x,z}}$, gray) combined with the computed lateral (y) component (dotted line connecting $\vec{\mathbf{F}}_{\text{wing}}$ and $\vec{\mathbf{F}}_{\text{wing,x,z}}$). Using the 3D surface model (depicted at 17% of 2nd wingbeat) we illustrate the reconstruction of Drag ($\vec{\mathbf{D}}$, red) and lift ($\vec{\mathbf{L}}$, blue) based on drag pointing opposite to wing velocity ($\vec{\mathbf{v}}_{\text{aero}}$, black) and being perpendicular to lift ($\vec{\mathbf{L}}$, blue), with drag and lift acting perpendicular to the vector connecting the shoulder joint to the ninth primary wingtip ($\mathbf{X}_{\text{p9}}$). Along this vector the mass of the wing is discretized using 20 point masses (green spheres; volume proportional to mass). Using triangulation, 12 body landmarks were manually tracked; black dots: ninth primary wingtip ($\mathbf{X}_{\text{p9}}$), seventh secondary feather, shoulder joint, wrist; gray dots: middle of the back (next to shoulder), left and right feet, left and right eyes, top of the head; gray cone: tip and base of the beak.

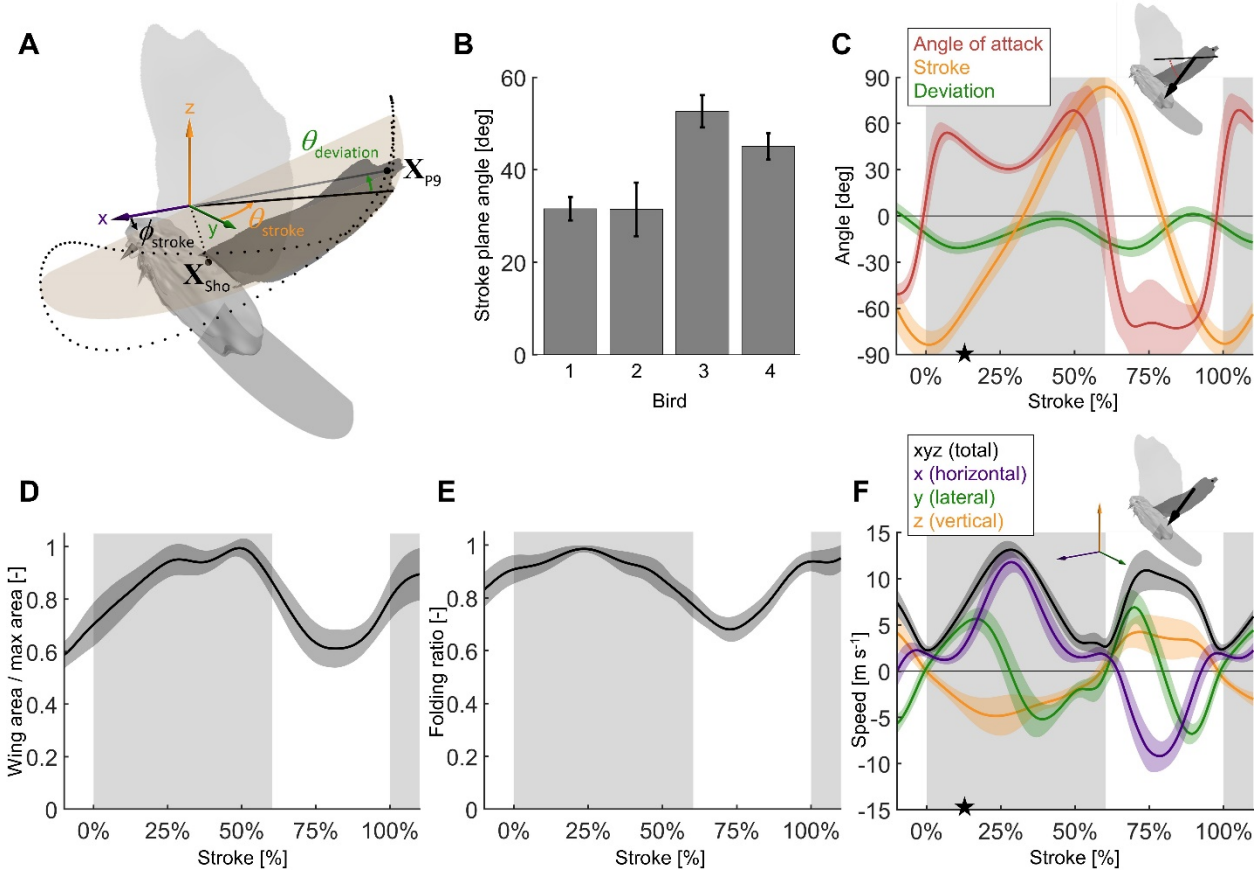

Figure 2. Measured wingbeat kinematics show wing area, extension, and speed are maximal mid-downstroke, while the wing angle of attack reaches a local minimum. (A) The stroke plane (light orange) fits the path of the vector originating from the shoulder joint and extending to the 9th primary feather tip ($\mathbf{X}_{P9}$, wingtip) during the wingbeat, which we use to define wing kinematics with three angles. First, the stroke plane is pitched down with respect to the horizontal by angle ϕ_{stroke} (rotated about the y axis). Second, the wing's stroke angle in the stroke plane is θ_{stroke} (with respect to the y axis). Finally, the stroke angle deviates out of the stroke plane by angle $\theta_{deviation}$. (B) The average stroke plane differs across the four doves while being consistent for each individual dove. (C) The wing stroke angle (orange), stroke deviation angle (green), and wing angle of attack (red) are consistent (low variance) across all flights and all four individuals. The only exception is the angle of attack during the upstroke. The avatar shows the angle of attack (red dotted line) definition: angle between wing chord (thin) and velocity vector (thick). The star on the stroke axis in Figures 2-4 represents the avatar displayed (at 17% of the 2nd wingbeat). (D) The wing surface area normalized with the fully extended area reaches a plateau between mid-downstroke and the start of the upstroke. (E) The wing folding ratio shows

wingspan reduction relative to the fully extended wing mid-downstroke. (F) The net wing speed (black) peaks mid-downstroke and mid-upstroke. The x-velocity component dominates net speed: x (horizontal; purple), y (lateral; green), and z (vertical; orange). The avatar shows the 3D wing velocity vector.

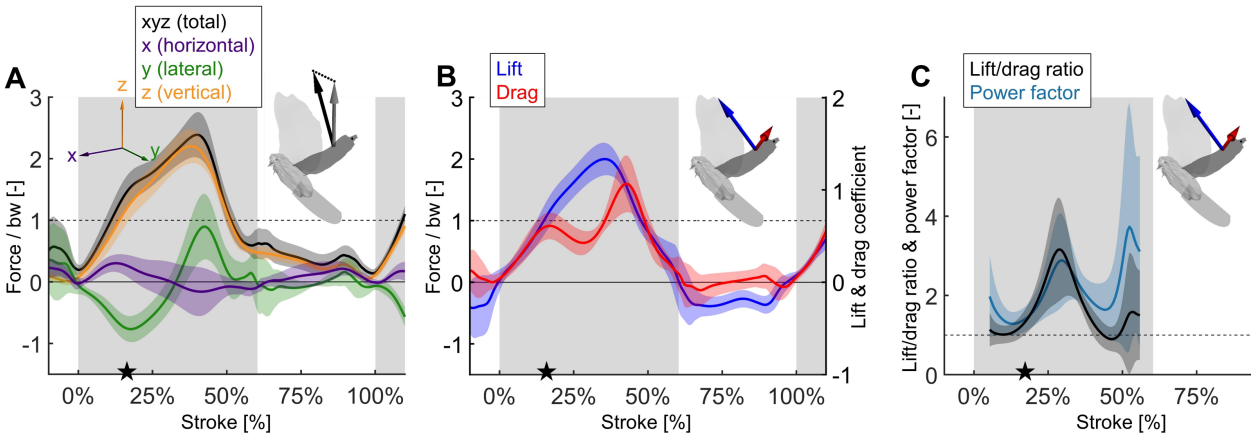

Figure 3. Mid-downstroke the lift peaks while drag reaches a local minimum, which coincides with a dip in angle of attack (Fig. 2C), causing the power factor (non-dimensional lift$^{3/2}$/drag) to reach a local maximum while the wing attains peak speed (Fig. 2F). This reduces the aerodynamic power needed to generate peak lift during mid-downstroke and support bodyweight (bw; used to normalize force). (A) Net aerodynamic force magnitude (black) peaks mid-downstroke and is composed of the recorded large vertical (z) and small horizontal (x) force as well as the computed lateral (y) force. The avatar shows both the 2D measured aerodynamic force vector ($\vec{F}_{wing,x,z}$; gray) and the net 3D vector ($\vec{F}_{wing}$; black). (B) During mid-downstroke, the lift force (blue) peaks while the drag force (red) dips. Lift is defined positive with respect to the wing surface normal, hence negative lift opposes gravity during the upstroke because the wing is inverted. (C) The glide ratio (lift/drag) and power factor (non-dimensional lift$^{3/2}$/drag) peak mid-downstroke when force and velocity peak. Glide ratio also peaks at stroke reversal, but because both force and velocity are small, and stroke reversal causes a kinematic singularity, it is of secondary interest. Similarly, because dividing by near-zero drag values is mathematically ill-defined, the upstroke plot has been removed.

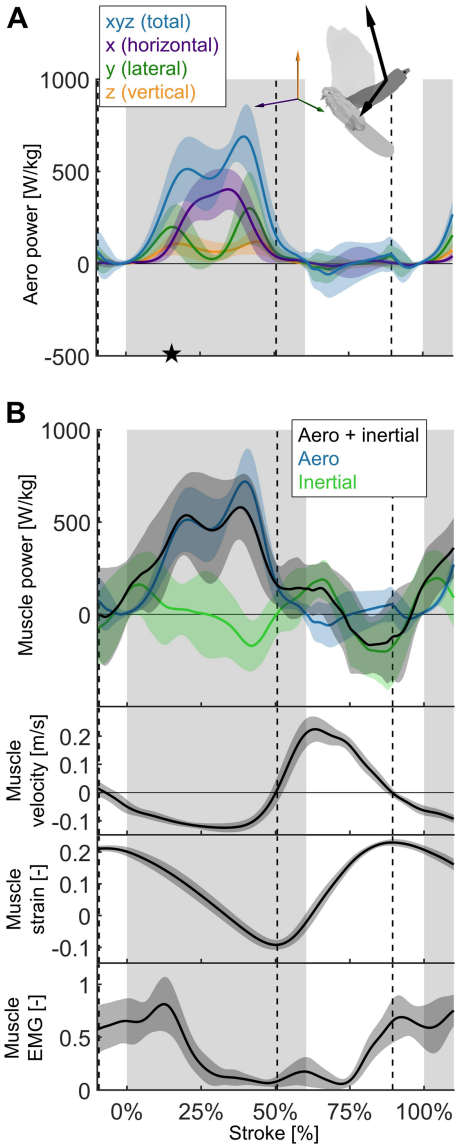

Figure 4. Mid-downstroke the aerodynamic power reaches a local minimum due to a dip in drag (Fig. 3B). Whereas aerodynamic power dominates the downstroke, inertial power dominates the upstroke. Considering wing acceleration is minimal mid-stroke, the total power (aerodynamic plus inertial) that the flight muscles need to generate dips midstroke. (A) The mid-downstroke dip in total aerodynamic power (blue) is composed out of horizontal (x), lateral (y), and vertical (z) power. The primary source of aerodynamic power stems from the horizontal contribution of drag (x, purple) because the wing moves forward (Fig. 2F) while generating a dominant opposing drag force (Fig. S5A). Because lift dominates drag in the vertical direction (Fig. S5C), and lift acts perpendicular to wing velocity (making the dot product zero), the vertical component of aerodynamic power (z, orange) is the smallest despite large vertical aerodynamic force (Fig. 3A). The avatar illustrates the wing velocity and net aerodynamic force

vectors. (B) The total power (black) the flight muscles need to generate is dominated by the aerodynamic power (matching blue line) during the downstroke, and by the inertial power (matching green line) during the upstroke. The onset of electrical activation of the pectoralis (muscle EMG) lines up with the onset of pectoralis shortening (decreasing muscle strain, negative muscle velocity) near the end of the upstroke (starting mid-upstroke). Notably, pectoralis shortening velocity reaches zero (dashed vertical line; also in subsequent plots) right before the start of the upstroke, when the required muscle power is low (and plateaus), and the supracoracoideus is known to take over [5].

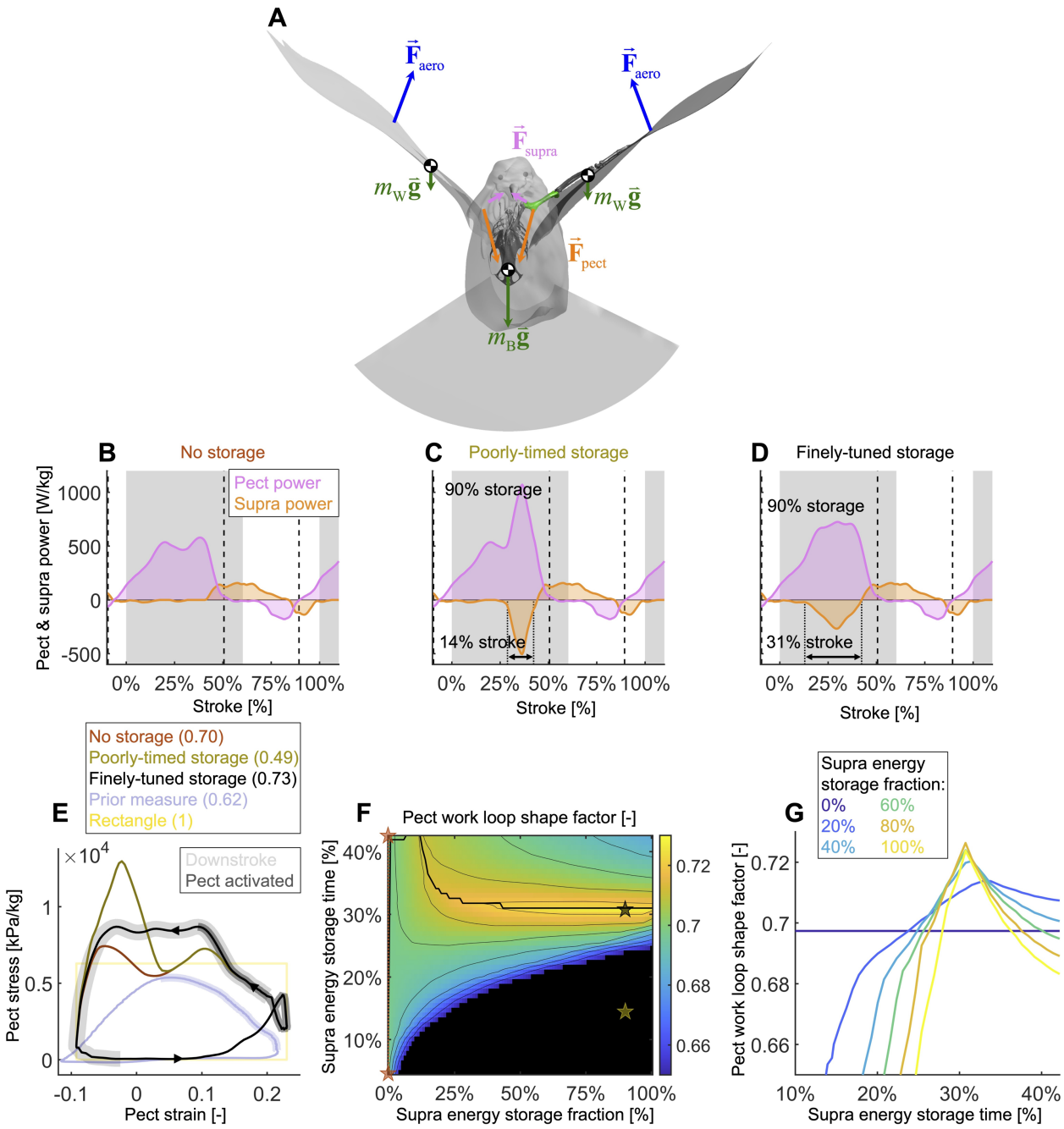

Figure 5. Finely-tuned energy storage in the supracoracoideus tendon simplifies the function of both major flight muscles: tendon energy release during the upstroke reduces the power the supracoracoideus needs to generate and simplifies its function to primarily generating force, while tendon energy storage during the downstroke makes the power output and stress level of the pectoralis more uniform. (**A**) External and internal force balance of the entire bird (shown) used to derive our 1D power balance by combining it with the associated kinematic velocities (not shown); see equations in Fig. S11. Approximately all internal flight forces and associated power are produced by the two primary

flight muscles, the pectoralis (orange; $\vec{\mathbf{F}}_{\text{pect}}$) and the supracoracoideus (pink; $\vec{\mathbf{F}}_{\text{supra}}$), which move the mass of the body (green; m_{B}: modeled as a point mass) and wings (green; m_{W}: modeled as 20 point masses displayed in Fig. 1C) to generate the wings' aerodynamic forces (blue; $\vec{\mathbf{F}}_{\text{aero}}$) and thus power to sustain flight. (**B**-**D**) The pectoralis (pink) generates positive power during the downstroke and acts like a brake to absorb negative power during the late-upstroke (power is normalized by pectoralis mass). The supracoracoideus (orange) generates and/or releases positive power during the upstroke (also normalized by pectoralis mass). Any energy released by the supracoracoideus tendon during the upstroke must first be stored during the downstroke, which is plotted as negative power (rate of energy storage; negative orange trace). (B) Without energy storage in the supracoracoideus tendon, there is an unfavorable mid-downstroke dip in the required pectoralis output power. (C) If energy storage is poorly timed during the downstroke, the required pectoralis output power unfavorably spikes. (D) If the timing and quantity of energy storage is finely-tuned, the pectoralis work loop is more favorably shaped mid-downstroke, as it more closely approximates the theoretically ideal rectangular work loop (yellow rectangle in €: drawn with the same area and strain range). (**E**-**G**) The shape factor of the pectoralis work loop is improved by finely-tuning the timing and quantity of elastic energy storage. (E) The finely-tuned elastic storage shown in (D) corresponds with the black work loop and results in the highest pectoralis shape factor for the range of elastic storage parameters we simulated in (F): 0.73 (numbers between parenthesis in (E): shape factor; dark gray shading: electrical pectoralis activation; light gray shading: downstroke phase). The shape factors of both the no-storage (brown; (B)) and finely-tuned storage (black; (D)) cases exceed prior shape factor measurement, using a strain gauge mounted on the deltopectoral crest (DPC) of the humerus to estimate pectoralis stress (light blue), of doves flying similarly slow [3]. (G) Work loop shape-factor as a function of elastic energy storage timing and fraction (color codes energy storage fraction): see Figs. S7-9 for a detailed overview.

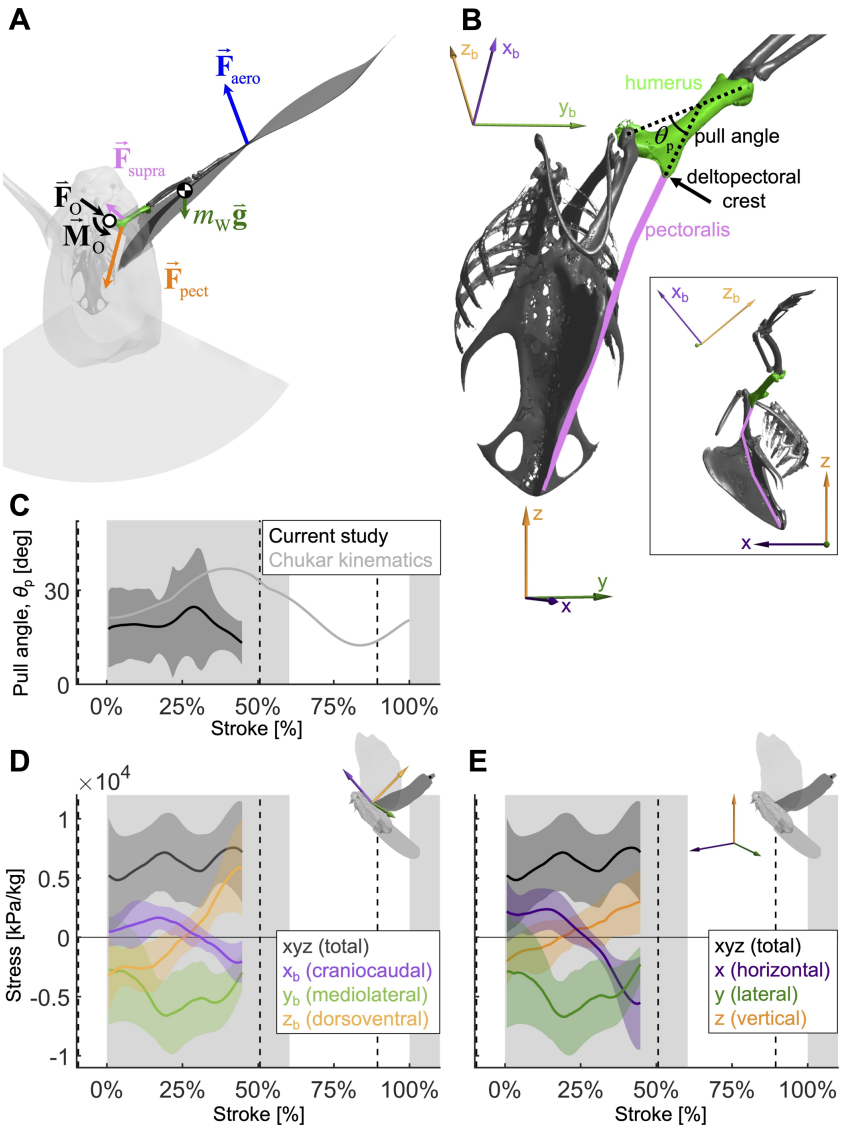

Figure 6. To quantify how the recruitment of the pectoralis muscle changes during the downstroke, we consider the balance of 3D angular momentum by calculating the associated torques. (A) The forces are the same we used in the 1D power balance (Fig. 5A), but instead of considering the entire bird we evaluate the balance around the left shoulder joint. Consequently body mass becomes irrelevant, and instead a reaction force ($\vec{\mathbf{F}}_0$; cancels out) and moment ($\vec{\mathbf{M}}_0$; assumed small compared to other torques) at the shoulder joint appear. (B) The pull angle between the humerus and the pectoralis, θ_p, dictates how effectively the pectoralis exerts torque on the wing. The inset shows the corresponding lateral view with subscript "b" referencing the body frame while no subscript indicates world frame. The pull angle depends both on the humerus orientation during the wingbeat and pectoralis muscle fiber recruitment. (C) During downstroke the pectoralis pull angle is low, consequently pectoralis force and contraction

speed are converted into lower net torque around the shoulder joint and higher angular velocity of the wing. The pull angle harnessed by doves in slow flight (black line) is lower than chukars running up an incline assisted by wingbeats (gray line). Integrating the outcome of our work loop analysis showing that tensioning the supracoracoideus tendon during the second half of the downstroke finely-tunes the wingbeat, we find that the required pectoralis moment increases the pectoralis pull angle to values higher than plotted here (not able to precisely plot because we did not measure the pull direction of the supracoracoideus), shifting the curve towards chuckar values. (D,E) The pectoralis pull direction matches the general pull direction for chukars during wing-assisted incline running [4], with the exception of the dorsal direction during the end of downstroke. This discrepancy may be due to tensioning of the supracoracoideus tendon, which would account for the pull in the dorsal direction. The 3D vector direction (purple: $+x_b$: cranial, $-x_b$: ventral; green: $+y_b$: medial, $-y_b$: lateral; orange: $+z_b$: dorsal, $-z_b$: ventral) and stress magnitude (black), associated with the pectoralis pull on the humerus, were computed using the pull angle and the modeled position of the humerus under the assumption that it is the only muscle generating a moment on the wing during the downstroke.

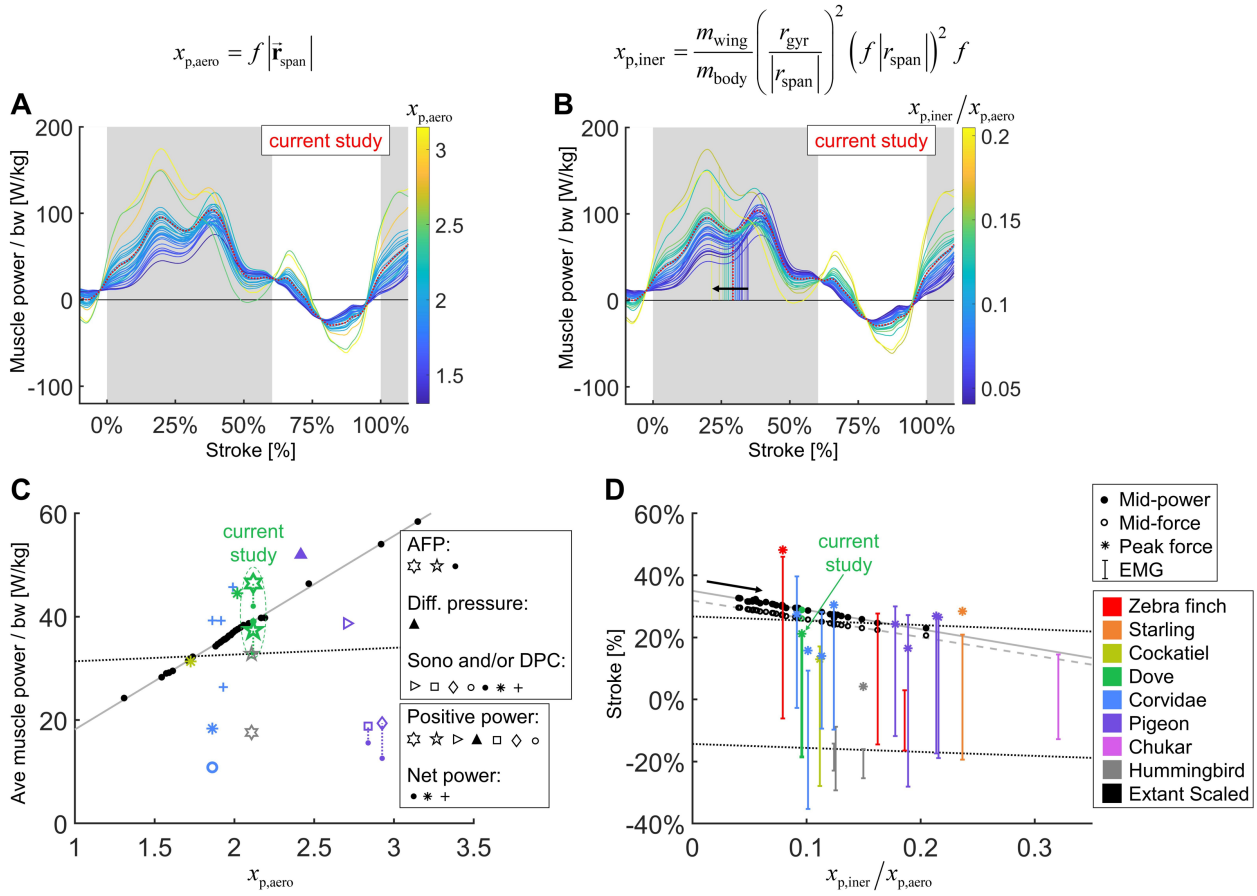

Figure 7. We integrate body morphological and kinematic scaling laws across extant birds with our aerodynamic, inertial, and muscle power measurement for doves, informed by our model, to find and anchor relationships that predict how average muscle power and timing should scale. (A-B) Averaged data from the current study is plotted in red, which is scaled based on extant bird data (other colored lines; power scaled by bodyweight: bw). (C-D) Data from the current study is plotted in green, and scaled extant bird data is plotted in black. Data measured directly in other studies at similar flight speeds (1.23 $m \cdot s^{-1}$) are plotted in multiple colors and marker types, which are explained in detail in the caption of corresponding Fig. S13. (A,C) The stroke-averaged muscle power scaled by bodyweight is proportional to wingtip velocity and the aerodynamic power scaling parameter, $x_{\mathrm{p,aero}}$. Stroke-averaged pectoralis power data from literature (fitted with dotted black line) is too scattered to confirm the trendline from our scaling analysis (solid gray line). (B,D) Because wing inertia dominates aerodynamic scaling, the pectoralis needs to activate earlier at larger scale (and vice versa). Hence, the timing of power and force production within the stroke scale according to the ratio of the inertial and aerodynamic power scaling parameters, $x_{\mathrm{p,iner}} / x_{\mathrm{p,aero}}$. The colored vertical lines in B are plotted at the midway point of pectoralis power exertion (Eqn. S75). This same midway point is plotted as filled dots in D with a solid gray linear-fit line. The midway point of pectoralis force exertion (Eqn. S76) is plotted as empty dots in D with a dashed gray linear-fit line. EMG timing data (colored solid lines with hashes at the start and end; starting points fitted with lower dotted black line) and corresponding peak pectoralis force data (asterisks; fitted with upper dotted black line) from literature are too scattered to confirm the subtle trendlines from our scaling analysis (solid and dashed gray lines).

Tables

Table 1. Morphological data for doves. (*N* = 4 doves).

Variable	Mean ± s.d.
Body mass [g]	161.6 ± 11.4
Wing span (tip to tip outstretched) [cm]	50.03 ± 2.28
Wing radius (tip to shoulder outstretched) [cm]	22.58 ± 1.13
Single wing area (outstretched) [cm^2]	182.6 ± 20.2
Tail area (outstretched) [cm^2]	140.1 ± 17.8
Aspect ratio [-]	6.89 ± 0.48
Single pectoralis mass [g]	14.66 ± 1.97
Pectoralis fasicle length [mm]	17.12 ± 1.43
Pectoralis fasicle angle [deg]	33.58 ± 2.85
Pectoralis PCSA [mm^2]	690.1 ± 92.8
Distance between pectoralis sonomicrometry crystals [mm]	12.27 ± 1.70
Single supracoracoideus mass [g]	3.26 ± 0.57

Table 2. Measured kinematics and contractile properties for the second stroke after takeoff. Positive yaw angle corresponds with the dove yawing to the left. The advance ratio is computed using the formula in Ellington 1984 [36] (*N* = 4 doves; *n* = 5 flights each).

Variable	Mean ± s.d.
Flight speed [$m \cdot s^{-1}$]	1.23 ± 0.13
Downstroke length [ms]	61.80 ± 4.73
Upstroke length [ms]	40.65 ± 3.88
Flapping frequency [Hz]	9.80 ± 0.62
Yaw angle [deg]	1.62 ± 6.33
Advance ratio [-]	0.14 ± 0.01
Max pectoralis strain [ε]	0.23 ± 0.01
Max pectoralis velocity [$m \cdot s^{-1}$]	0.24 ± 0.04

Supplementary

Supplemental Results

Section S1: Effects of surgery

While many studies involving surgical procedures have been conducted to study the pectoralis [2], [3], [5], [8]–[10], [14], [15], [47], few quantified the change in flight performance due to the surgery [44]. While we primarily analyzed the second wingbeat that the doves made after takeoff after undergoing surgery, we recognize that this may constrain our understanding of dove flight in general. Hence, we first analyzed the effects of the surgical procedure and muscle recording cable on the overall flight dynamics for one dove for which we made recordings before as well as after the surgical procedures.

For this one dove, surgery consistently changed the way it took off and flew (Fig. S2). After the surgery, the dove pushed off from the takeoff perch with similar vertical force (vertical impulse before: 0.39 ± 0.03; after: 0.34 ± 0.03), but substantially less forward force (horizontal impulse before: 0.81 ± 0.03; after: 0.56 ± 0.05; gravity was subtracted from vertical impulses; all impulses were scaled by bodyweight and integration time). During flight, the dove produced a smaller braking force after the surgery (horizontal impulse before: -0.09 ± 0.02; after: -0.03 ± 0.01). Additionally, the dove used more wingbeats to fly the same distance, resulting in a higher flapping frequency (before: 8.28 ± 0.19 Hz; after: 9.20 ± 0.15 Hz), and a different first stroke. The first downstroke was smaller in magnitude (maximum force scaled by bodyweight before: 2.18 ± 0.13; after: 1.09 ± 0.05) and began 14.4 ± 4.6 milliseconds before release from the perch rather than 54.9 ± 12.7 milliseconds after release from the perch.

The effects of the suspended recording cable were less pronounced than the effects of surgery, although still noticeable. The mass of the entire cable was 26.1 grams, but the extra mass moved by the dove was only an average of 10.9 ± 3.8 grams (6.4% ± 2.2% of bodyweight) based on bodyweight measurements recorded while the dove was sitting on the takeoff perch. When the dove was carrying the extra mass of the cable, it pushed off from the takeoff perch in a more forward direction (vertical impulse scaled by bodyweight before: 0.34 ± 0.03; after scaled by bodyweight plus cable: 0.29 ± 0.05; horizontal impulse scaled by bodyweight before: 0.56 ± 0.05; after scaled by bodyweight plus cable: 0.64 ± 0.03). Once airborne, the dove produced greater vertical impulse (before: -0.28 ± 0.04; after: -0.23 ± 0.06), and greater forward impulse (before: -0.03 ± 0.01; after: 0.02 ± 0.03), while flapping more frequently (before: 9.20 ± 0.15 Hz; after: 9.62 ± 0.22 Hz). However, all of these flight differences are small compared to the differences caused by the surgery.

When we compare the aerodynamic forces produced before and after surgery by dove three (Fig. S2 and Table S2), we find an increase in flapping frequency after surgery which mirrors the differences in flight performance reported for a small passerine [44]. Additionally, after surgery, we consistently observed a modified takeoff pattern: the dove pushed off with less forward force, and its first downstroke was earlier and produced less aerodynamic force. Overall, the flight performance of the dove was substantially altered by the surgery, and to a lesser degree, by the weight increase due to the attached recording cable. However, these changes are analogous to changing the task the dove needs to accomplish, similar to changing flight distance, speed, or angle. Our results therefore quantify this particular, post-surgery flight condition, rather than flight in general.

Section S2: Flight styles among individuals

The four doves used somewhat different flight strategies from one another (Figs. 2B, S3), yet parameters during the second downstroke were similar across 20 flights (Figs. 1A, 2, Table S3). During takeoff, dove 1 pushed off with the most force, while dove 4 pushed off with the least force in both the vertical (vertical impulse for dove 1: 0.34 ± 0.04; dove 4: 0.23 ± 0.06) and horizontal directions (horizontal impulse for dove 1: 0.77 ± 0.06; dove 4: 0.44 ± 0.04; gravity was subtracted from vertical impulses; impulses herein are dimensionless as they were scaled by bodyweight (N) and integration time (s)). Because dove 1 pushed off with greater forward force, it could start braking earlier in the flight than dove 4, which still needed to produce forward thrust during the second stroke after takeoff (horizontal impulse for dove 1: -0.09 ± 0.01; dove 4: 0.17 ± 0.03). This may explain the difference in stroke plane angle during the second downstroke for the two doves (Fig. 2B; dove 1: 31.6° ± 2.5°; dove 4: 45.07° ± 2.8°), even though there is not substantial variation in the other kinematic angles among the doves (Fig. 2C): whereas the aerodynamic force magnitude needed was similar for both doves due to weight support, the force direction was different. The vertical force during the second stroke was additionally influenced by the timing and number of strokes the doves took (number of strokes between takeoff and landing for dove 1: 4; dove 2: 5; dove 3: 4; dove 4: 5), but, overall, we found that the vertical aerodynamic force was relatively consistent during the second stroke (vertical impulse for all doves: 0.86 ± 0.09; gravity not subtracted here for clarity).

During the second stroke, the pectoralis muscle performance was consistent across the 20 flights (Figs. 1A, S3). The electrical activation of the pectoralis began during the middle portion of the upstroke, 7.07 ± 5.10 milliseconds before the pectoralis began shortening, which occurred 10.54 ± 2.86 milliseconds before the beginning of the downstroke (defined by kinematic stroke reversal: see stroke

angle in Fig. 2C). The electrical activation then lasted 37.63 ± 7.66 milliseconds and ended 68.57 ± 3.38 milliseconds before the pectoralis completed contracting, which occurred 11.06 ± 1.99 milliseconds before the end of the downstroke. The pectoralis shortened for 59.62 ± 3.84 milliseconds during the stroke which lasted 102.45 ± 6.59 milliseconds (downstroke: 61.80 ± 4.73 milliseconds). Furthermore, we see that the timing of the pectoralis contraction corresponds with the majority of aerodynamic force production.

Section S3: Analysis of 3D muscle torques

Using the 3D angular momentum balance model (Fig. 6), we can compute the time-resolved moment vector (torques) generated by the pectoralis muscle during the downstroke. Due to the complexity of 3D moments, we consider each of the three components of muscle torque on the wing separately.

First, we consider the moment in the roll axis (x_b points in the cranial direction and is aligned with the thoracic vertebrae of the dove; Figs. 6B, S10B). During the majority of the downstroke, the flight muscles pulled ventrally on the wing (average ventral moment during downstroke: 0.140 ± 0.013 N-m) to oppose lift and drag, whose world z-axis components each point vertically up (Fig. S5C). Just before the end of the downstroke, and 1.97 ± 1.91 milliseconds before the pectoralis began lengthening, inertial effects from decelerating the wing were associated with a small dorsal moment (average dorsal moment at the end of the downstroke: 0.057 ± 0.026 N-m). As is the case for power, inertia dominated during the upstroke.

Second, we consider the moment in the pitch axis (y_b points laterally towards the distal wing, perpendicular to the thoracic vertebrae; Fig. S10C), in which the effects of aerodynamics dominated over inertia. When we examine the lift and drag forces (Figs. 4, S5), we again see that the vertical direction was the most important during the downstroke because forces in the lateral direction created no y_b moment, and the horizontal forces were small (15.5% ± 4.1% of the stroke-averaged net aerodynamic force during the downstroke). At the beginning of the downstroke, the wing was at the posterior of the bird, creating a positive aerodynamic torque in the y_b axis, which was balanced by a negative muscle moment in the y_b axis (flight muscle acting to supinate the wing). At the end of the downstroke, the wing was at the anterior of the bird, with a negative aerodynamic torque. Hence, the total muscle moment in the pitching axis acted to first supinate (average supination moment during beginning of downstroke: 0.047 ± 0.010 N-m), then pronate (average pronation moment during end of downstroke: 0.068 ± 0.026 N-m), the wing during the downstroke. Since the pectoralis is thought mainly

763 to pronate the wing, it appears that other flight muscles are driving the small supination moment at the
764 beginning of the downstroke.

765 Finally, we consider the moment in the yaw axis (z_b points in the dorsal direction; Fig. S10D),
766 where aerodynamics again dominate the downstroke. To gain a more holistic view of the relationship
767 between the moment in the yaw axis and the horizontal, lateral, and vertical world components of lift
768 and drag, it is helpful to examine Fig. S10E-G, where we plot the 3D moments in the world coordinate
769 system. The aerodynamic moment in the vertical world axis was small throughout the downstroke
770 (average magnitude: 0.029 ± 0.009 N-m), because the vertical lift and drag create no moment in the
771 vertical direction (Fig. S10G). Therefore, the yaw aerodynamic moment originated primarily from the
772 moment in the horizontal world axis, rotated about the lateral world axis by the amount that the dove
773 pitches its body forward. The net effect was to generate an average muscle moment of 0.063 ± 0.017 N-
774 m in the caudal direction during the downstroke.

775 As is the case for the power analysis, the effects of the aerodynamics dominated during the
776 downstroke, whereas inertia dominates during the upstroke and near stroke reversal. Furthermore, for
777 all three components of the aerodynamic moment, we find that the components of lift and drag in the
778 vertical world direction were dominant.

779

780 Supplemental Methods

781 Section S4: Muscle activation and strain measurement details

782 To measure the electrical activation and strain of the left and right pectoralis muscles, we surgically
783 implanted EMG electrodes and sonomicrometry crystals using standard methods for the pectoralis of
784 birds [9], [44]. The doves were anesthetized using isoflurane by inhalation. Then, each pair of
785 sonomicrometry crystals (2.0 mm; Sonometrics, Inc., London, ON, Canada) and each custom-made, fine-
786 wire bipolar EMG hook electrode (0.5 mm bared tips with 2 mm spacing; California Fine Wire, Inc.,
787 Grover Beach, CA, USA) were implanted parallel to the fascicle axis of the mid-anterior region of
788 sternobrachial portion of pectoralis at a depth of approximately 4 mm beneath the superficial fascia of
789 the muscle. Before suturing (4-0 coated Vicryl) all of the openings, the sonomicrometry signals were
790 tested to ensure good signal quality. Then, all of the electrodes were sutured down a few millimeters
791 away from the exit point on the superficial fascia of the pectoralis, to prevent movement independent
792 of the fascicles. We left a small loop in the EMG electrode at the surface of the muscle to limit low-
793 frequency noise. The electrode and transducer wires were tunneled under the skin along a narrow path
794 from the ventral incision, along the lateral side of the dove, to the dorsal surface where the wires

terminated into a back plug. The back plug was secured to the dove's back by suturing the base of the plug to intervertebral ligaments, and it was custom-made (prior to surgery) using terminal strips and epoxy. The skin was sutured closed around the back plug. After the experiments, the doves were euthanized using an overdose of isoflurane. All surgical procedures were in accordance with Stanford University's Institutional Animal Care and Use Committee and followed established methods and protocols [2], [3], [5], [9], [10], [15], [47].

Recordings were made by connecting a shielded cable (flexible wires sheathed approximately every 30 cm; diameter 7 mm) to the back plug on the dorsal side of the dove. We loosely suspended the cable above the dove (Fig. S1), and the length of the cable that was suspended was approximately 76 mm, weighing 26.1 g. The cable was connected to an Ultrasound Dimension Gauge (UDG; Sonometrics, Inc., London, ON, Canada) to measure the sonomicrometry signals, and to a differential AC amplifier (Model 1700; A-M Systems, Sequim, WA, USA) to measure the EMG signals. All signals were recorded at 10,000 Hz using a Digidata 1550A A/D converter (Axon Instruments, Union City, CA, USA). Sonomicrometry signals were converted into fiber lengths, $L_{\mathrm{pect,f}}$, by calibrating at 0 mm, 5 mm, and 10 mm, and assuming the speed of sound transmission is 1590 m·s^{-1} when the muscle is at 37 degrees Celsius [48]. Then, these fiber lengths were converted into fiber strain, $\gamma_{\mathrm{pect,f}}$, using Eqn 4. We corrected for a time delay of 2 ms (2.0% of the stroke) based on the time delay in the UDG, whereas the EMG signals did not have any time lag. To compare the EMG signals across all flights, we filtered the rectified signal with a second order butterworth filter with a cutoff frequency of 50 Hz. While we recorded EMG signals for both the left and right pectoralis muscles, the right signal was unreliable, so we only include data from the left EMG.

Section S5: Aerodynamic force measurement validation

The 2D AFP setup [31], [43] was validated by tethering a quadcopter to an instrumented beam and then comparing vertical and horizontal forces measured by the beam with forces measured by the AFP, as reported in [31]. Over a period of 10 seconds and a sampling rate of 1000 Hz, the impulse ratio and the mean force ratio of the 2D AFP to the beam were both 1.00 ± 0.02 (n = 10 trials) in the vertical direction and 1.00 ± 0.01 in the horizontal direction (n = 20 trials). Additionally, for a flight that starts and ends at rest, we expect that the total vertical impulse imparted by the legs and wings should equal full bodyweight support [29], and that the net horizontal impulse should equal zero. Integrating the forces from takeoff to landing for the dove's flight, we measured a vertical impulse ratio (impulse from legs and

wings divided by impulse due to bodyweight, bw) of 1.03 ± 0.02, and a horizontal impulse (impulse from legs and wings divided by bodyweight) of 0.02 ± 0.02 bw·s for 15 flights where the doves did not have an external cable attached to the back. For the 20 flights where the doves had a cable attached, we measured a vertical impulse ratio of 1.01 ± 0.02, and a horizontal impulse of 0.08 ± 0.02 bw·s. The horizontal impulse is greater than zero when the cable is attached, because the dove did positive work to pull the cable forward.

Section S6: Aggregate aerodynamic and kinematic parameters

To compare all flights and understand the underlying dynamics, we reduced the highly resolved 3D surface and kinematic measurements, in combination with the measured aerodynamic forces, into simplified aerodynamic and kinematic parameters which summarize the time-resolved state of entire wing.

To facilitate this simplification, we divided the wing into blade elements spaced 1 mm apart in the spanwise direction. For each blade element (J total blade elements, index j), we computed: 1) the surface area, S_{j}, 2) the chordline vector from the trailing edge to the leading edge, 3) the velocity vector at the quarter-chord location (25% chord length behind the leading edge; measured relative to the Newtonian reference frame, N), ${}^{\mathrm{N}}\vec{\mathbf{v}}^{\mathrm{j}}$, which includes the velocity components of both the flapping and morphing motion of the wing, and 4) the angle of attack induced by wing motion, α_{j}, which is the angle between the chordline and velocity vectors (Fig. 2A,C).

We computed many of the simplified wing parameters using the spanwise blade element measurements and the 3D kinematics measurements. From the spanwise blade element measurements, we computed representative wing measurements which are the weighted averages of the blade element values (derived in Deetjen et al. 2020 [33]):

$$\vec{\mathbf{v}}_{\mathrm{wing}} = \frac{\sum_{\mathrm{j}=1}^{\mathrm{J}} S_{\mathrm{j}} \left| {}^{\mathrm{N}}\vec{\mathbf{v}}^{\mathrm{j}} \right|^2 \, {}^{\mathrm{N}}\vec{\mathbf{v}}^{\mathrm{j}}}{\sum_{\mathrm{j}=1}^{\mathrm{J}} S_{\mathrm{j}} \left| {}^{\mathrm{N}}\vec{\mathbf{v}}^{\mathrm{j}} \right|^2} \,, \tag{S1}$$

$$\alpha_{\mathrm{wing}} = \frac{\sum_{\mathrm{j}=1}^{\mathrm{J}} S_{\mathrm{j}} \left| {}^{\mathrm{N}}\vec{\mathbf{v}}^{\mathrm{j}} \right|^2 \alpha_{\mathrm{j}}}{\sum_{\mathrm{j}=1}^{\mathrm{J}} S_{\mathrm{j}} \left| {}^{\mathrm{N}}\vec{\mathbf{v}}^{\mathrm{j}} \right|^2} \,. \tag{S2}$$

The weight for each blade element is the surface area times the velocity magnitude squared. To precisely track the position and orientation of the wing, we defined the stroke plane angle, ϕ_{stroke}, stroke angle, θ_{stroke}, deviation angle, $\theta_{\text{deviation}}$, and twist angle, θ_{twist}, of the wing (Fig. 2A). The stroke plane was linearly fit using the path swept by the tip of the ninth primary feather across the full wingbeat, where a positive stroke plane angle corresponds to a stroke plane which is pitched down. The stroke angle and deviation angle are defined relative to the stroke plane according to Fig. 2A, and the twist angle is the angle between the chordline vector at the root and the chordline vector along the span of the wing. Finally, we also computed time-resolved parameters to describe wing morphing. The semi-wing surface area, S_{wing}, is the area of a single wing:

$$S_{\text{wing}} = \sum_{\text{j=1}}^{\text{J}} S_{\text{j}}, \tag{S3}$$

which we used to calculate the aspect ratio, AR_{wing}, of the wing:

$$AR_{\text{wing}} = \frac{b_{\text{wing}}^2}{S_{\text{wing}}}, \tag{S4}$$

where the wing radius, b_{wing}, is the length of the V-shaped path from the shoulder joint to the wrist joint to the ninth primary feather. The folding ratio, FR_{wing}, of the wing:

$$FR_{\text{wing}} = \frac{\left|\vec{\mathbf{r}}_{\text{span}}\right|}{\max\left|\vec{\mathbf{r}}_{\text{span}}\right|}, \tag{S5}$$

depends on the span vector, $\vec{\mathbf{r}}_{\text{span}}$, which is the vector from the shoulder joint to the ninth primary feather. The max function finds the maximum value across the stroke.

To compute the lift and drag forces and the lateral (right to left) aerodynamic forces produced by the wing (Fig. 1C), we utilized the measured vertical and horizontal aerodynamic forces, in addition to the 3D surface and kinematic measurements. From the derivation in Deetjen et al. 2020 [33], the directions of lift, $\hat{\mathbf{L}}_{\text{L}}$, and drag, $\hat{\mathbf{D}}_{\text{L}}$, for the entire left wing are:

$$\hat{\mathbf{D}}_{\text{L}} = -\frac{\sum_{\text{j=1}}^{\text{n}} S_{\text{j}} \left|{}^{\text{N}}\vec{\mathbf{v}}^{\text{j}}\right| {}^{\text{N}}\vec{\mathbf{v}}^{\text{j}}}{\left|\sum_{\text{j=1}}^{\text{n}} S_{\text{j}} \left|{}^{\text{N}}\vec{\mathbf{v}}^{\text{j}}\right| {}^{\text{N}}\vec{\mathbf{v}}^{\text{j}}\right|}, \tag{S6}$$

$$\hat{\mathbf{L}}_{\mathrm{L}} = \pm \frac{\hat{\mathbf{D}}_{\mathrm{L}} \times \vec{\mathbf{r}}_{\mathrm{span}}}{\left|\hat{\mathbf{D}}_{\mathrm{L}} \times \vec{\mathbf{r}}_{\mathrm{span}}\right|}. \tag{S7}$$

To compute the magnitude of lift, L, and drag, D, on both wings, we included the net measured horizontal, $F_{\mathrm{AFP,x}}$, and vertical, $F_{\mathrm{AFP,z}}$, aerodynamic forces:

$$D = \frac{\left(\hat{L}_{\mathrm{L,x}} \cos^2\theta - \hat{L}_{\mathrm{L,y}} \cos\theta \sin\theta\right) F_{\mathrm{AFP,z}} - \hat{L}_{\mathrm{L,z}} F_{\mathrm{AFP,x}}}{2\bar{S}}, \tag{S8}$$

$$L = -\frac{\left(\hat{D}_{\mathrm{L,x}} \cos^2\theta - \hat{D}_{\mathrm{L,y}} \cos\theta \sin\theta\right) F_{\mathrm{AFP,z}} - \hat{D}_{\mathrm{L,z}} F_{\mathrm{AFP,x}}}{2\bar{S}}, \tag{S9}$$

$$\bar{S} = \left(\hat{L}_{\mathrm{L,x}} \cos^2\theta - \hat{L}_{\mathrm{L,y}} \cos\theta \sin\theta\right) \hat{D}_{\mathrm{L,z}} - \hat{L}_{\mathrm{L,z}} \left(\hat{D}_{\mathrm{L,x}} \cos^2\theta - \hat{D}_{\mathrm{L,y}} \cos\theta \sin\theta\right), \tag{S10}$$

where the x and z subscripts indicate the components of the lift and drag unit vectors, and θ is the yaw angle of the dove. A positive yaw angle corresponds with the dove yawing to the left. Finally, we summed the lift and drag vectors to compute the total 3D aerodynamic force vector produced by the wing, $\vec{\mathbf{F}}_{\mathrm{wing}}$:

$$\vec{\mathbf{F}}_{\mathrm{wing}} = D\widehat{\mathbf{D}} + L\widehat{\mathbf{L}}. \tag{S11}$$

Near stroke reversal, these equations encounter a singularity, so we smoothed the angle of attack, and lift and drag forces in these regions using the `perfect smoother' [45] with smoothing weights, W, based on the same approach as in Deetjen et al. 2020 [33]:

$$W = 1 - \max\left\{0, \min\left\{1, \frac{\log\left|\bar{S}\right| - \log c_1}{\log c_0 - \log c_1}\right\}\right\}, \tag{S12}$$

with $c_0 = 0.15$ and $c_1 = 0.35$.

Section S7: 1D power balance of the entire dove

To compute the time-resolved power that the dove's muscles must have produced, we balanced the muscle power with the effects of the aerodynamic forces and inertia.

To do this, we first needed to decide what the most effective scope to analyze power is: power balance of a single wing of the dove, or power balance of the entire dove. To aid in this decision, we examined the definition of power, ${}^{\mathrm{N}}P^{\mathrm{B}}$, for a system B (a collection of point masses and rigid bodies: scope of the power analysis) in the Newtonian reference frame N:

$$ {}^{\mathrm{N}}P^{\mathrm{B}} = \frac{d\,{}^{\mathrm{N}}K^{\mathrm{B}}}{dt}, \tag{S13} $$

where ${}^{\mathrm{N}}K^{\mathrm{B}}$ is the kinetic energy of system B in reference frame N. Specifying what system B encompasses was needed to clarify how terms relating to the muscles, aerodynamics, and inertia would be incorporated into this high-level equation. One possible way to define system B was as a system that contains only point masses and rigid bodies which model a single wing of the dove. This definition is advantageous because it eliminates the term related to the kinetic energy of the body, which involves the second derivative of the position of the body. However, the disadvantage of this definition is that an extra power term appeared which we could not measure. That is, we had no method to measure the reaction force on the shoulder joint, which contributed to power because it was an external force acting on the wing. The only alternative way to eliminate this term was to assume that the shoulder joint itself moved in a Newtonian reference frame (constant velocity and no rotation), which is a large over-simplification. Instead, we defined system B to contain the entire dove, and accepted the difficulty in computing the second derivative of the position of the body, which could add noise to the results. With the scope of the power balance decided, we expanded each side of Eqn. S13 to incorporate the effects of the muscles, aerodynamics, and inertia.

The kinetic energy on the right side of Eqn. S13 is made up of the distributed masses of the wings and body. This term expands to:

$$ {}^{\mathrm{N}}K^{\mathrm{B}} = \frac{1}{2}\sum_{\mathrm{i}=1}^{\mathrm{I}_{\mathrm{W,B}}}\left(m_{\mathrm{i}}\,{}^{\mathrm{N}}\vec{\mathbf{v}}^{\mathrm{i}} \cdot {}^{\mathrm{N}}\vec{\mathbf{v}}^{\mathrm{i}} + {}^{\mathrm{N}}\boldsymbol{\omega}^{\mathrm{B_i}} \cdot \vec{\mathbf{I}}^{\mathrm{B_i}} \cdot {}^{\mathrm{N}}\boldsymbol{\omega}^{\mathrm{B_i}} \right), \tag{S14} $$

where m_{i} is the mass of the ith of $\mathrm{I}_{\mathrm{W,B}}$ point masses in the body and wings, ${}^{\mathrm{N}}\vec{\mathbf{v}}^{\mathrm{i}}$ is the velocity vector of the center of mass of the ith point mass in the Newtonian reference frame, ${}^{\mathrm{N}}\boldsymbol{\omega}^{\mathrm{B_i}}$ is the angular velocity of the reference frame of the ith body in system B relative to the Newtonian reference frame, and $\vec{\mathbf{I}}^{\mathrm{B_i}}$ is the moment of inertia of the ith body in system B relative to the center of mass of that body. Since we modeled the dove using point masses, Eqn. S14 simplifies to:

$$ {}^{\mathrm{N}}K^{\mathrm{B}} = \frac{1}{2}\sum_{\mathrm{i}=1}^{\mathrm{I}_{\mathrm{W,B}}} m_{\mathrm{i}}\,{}^{\mathrm{N}}\vec{\mathbf{v}}^{\mathrm{i}} \cdot {}^{\mathrm{N}}\vec{\mathbf{v}}^{\mathrm{i}}. \tag{S15} $$

The power term on the left side of Eqn. S13 is made up of the external power exerted on the dove and the internal power produced by the dove. Assuming that all the internal power produced by the dove was accounted for by the two pectorales and supracoracoideuses, the dove's power expands to:

$$ {}^{\mathrm{N}}P^{\mathrm{B}} = 2\,{}^{\mathrm{N}}P^{\mathrm{pect}} + 2\,{}^{\mathrm{N}}P^{\mathrm{supra}} - {}^{\mathrm{N}}P^{\mathrm{aero}} - {}^{\mathrm{N}}P^{\mathrm{g}}, \tag{S16} $$

where $-{}^{\mathrm{N}}P^{\mathrm{aero}}$ is the power done by external aerodynamic forces, $-{}^{\mathrm{N}}P^{\mathrm{g}}$ is the power done by external gravitational forces, ${}^{\mathrm{N}}P^{\mathrm{pect}}$ is the internal power produced by each pectoralis muscle, and ${}^{\mathrm{N}}P^{\mathrm{supra}}$ is the internal power produced by each supracoracoideus muscle. We derived the aerodynamic power in Deetjen et al. 2020 [33]:

$$ {}^{\mathrm{N}}P^{\mathrm{aero}} = -2\vec{\mathbf{F}}_{\mathrm{aero}} \cdot \vec{\mathbf{v}}_{\mathrm{wing}}, \tag{S17} $$

where $\vec{\mathbf{F}}_{\mathrm{aero}}$ is the overall aerodynamic force on the wing, and $\vec{\mathbf{v}}_{\mathrm{wing}}$ is the representative wing velocity vector computed using Eqn. S1. The gravitational power is the summation of the gravity forces on each point mass dotted with their velocity vectors:

$$ {}^{\mathrm{N}}P^{\mathrm{g}} = -\sum_{\mathrm{i}=1}^{\mathrm{I_{W,B}}} m_{\mathrm{i}}\vec{\mathbf{g}} \cdot {}^{\mathrm{N}}\vec{\mathbf{v}}^{\mathrm{i}}, \tag{S18} $$

where $\vec{\mathbf{g}}$ is the gravity vector. This equation can be simplified, showing that only the velocity in the z direction is relevant for gravitational power:

$$ {}^{\mathrm{N}}P^{\mathrm{g}} = \sum_{\mathrm{i}=1}^{\mathrm{I_{W,B}}} m_{\mathrm{i}} g\, {}^{\mathrm{N}}v_{\mathrm{z}}^{\mathrm{i}}, \tag{S19} $$

where g is the magnitude of gravity and ${}^{\mathrm{N}}v_{\mathrm{z}}^{\mathrm{i}}$ is the vertical component of the velocity vector.

To compare the effects on required muscle power from terms related to inertia *versus* aerodynamics, we grouped all of the terms related to inertia together, and named the resulting term inertial power:

$$ {}^{\mathrm{N}}P^{\mathrm{inertia}} = \frac{d\,{}^{\mathrm{N}}K^{\mathrm{B}}}{dt} + {}^{\mathrm{N}}P^{\mathrm{g}}, \tag{S20} $$

$$ {}^{\mathrm{N}}P^{\mathrm{inertia}} = \frac{1}{2}\frac{d}{dt}\left(\sum_{\mathrm{i}=1}^{\mathrm{I_{W,B}}} m_{\mathrm{i}}\,{}^{\mathrm{N}}\vec{\mathbf{v}}^{\mathrm{i}} \cdot {}^{\mathrm{N}}\vec{\mathbf{v}}^{\mathrm{i}}\right) + \sum_{\mathrm{i}=1}^{\mathrm{I_{W,B}}} m_{\mathrm{i}} g\, {}^{\mathrm{N}}v_{\mathrm{z}}^{\mathrm{i}}. \tag{S21} $$

Hence, the total muscle power simply equals the inertial power plus the aerodynamic power:

$$ 2\,{}^{\mathrm{N}}P^{\mathrm{pect}} + 2\,{}^{\mathrm{N}}P^{\mathrm{supra}} = {}^{\mathrm{N}}P^{\mathrm{inertia}} + {}^{\mathrm{N}}P^{\mathrm{aero}}, \tag{S22} $$

which could be computed using the aerodynamic forces and kinematics that we measured. During the mid-downstroke, the pectoralis primarily produces the power, so we eliminated the supracoracoideus term.

In order to convert the muscle power into force and stress, we incorporated the strain measured *in vivo* and other parameters measured during dissection. The power produced by the pectoralis equals the total force generated by the pectoralis measured at the attachment point, F_{pect}, times the rate of change of the length of the entire pectoralis, $\dot{L}_{\text{pect}}$:

$$^{\text{N}}P^{\text{pect}} = F_{\text{pect}}\dot{L}_{\text{pect}}. \tag{S23}$$

Since the pectoralis is not uniform along its length, we computed the rate of change of its length using measurements taken from the *in vivo* experiment and during the dissection:

$$\dot{L}_{\text{pect}} = \cos\left(\bar{\alpha}_{\text{pect,f}}\right)\dot{\gamma}_{\text{pect,f}}\bar{L}_{\text{pect,f}}, \tag{S24}$$

where $\bar{\alpha}_{\text{pect,f}}$ is the average measured muscle fiber angle (dissection), $\bar{L}_{\text{pect,f}}$ is the average measured muscle fiber length (dissection), and $\dot{\gamma}_{\text{pect,f}}$ is the measured strain rate of the muscle fibers assuming uniform strain throughout the muscle (*in vivo*). To convert the muscle force to the average muscle stress, σ_{pect}, we calculated the Physiological Cross-Sectional Area (PCSA) [49], which is the area of the cross section of the pectoralis perpendicular to its fibers:

$$\sigma_{\text{pect}} = \frac{F_{\text{pect}}}{\text{PCSA}_{\text{pect}}}, \tag{S25}$$

$$\text{PCSA}_{\text{pect}} = \frac{m_{\text{pect}}}{\rho_{\text{pect}}\left(\bar{L}_{\text{pect,f}}\right)}. \tag{S26}$$

For muscle density, we use $\rho_{\text{pect}} = 1060$ kg·m^{-3} [5], and m_{pect} is the average mass of the left and right pectorales of each dove measured during dissection.

Section S8: 3D angular momentum balance of the wing

To compute the time-resolved 3D moment vector (torque) that the dove's muscles must have produced, we balanced the muscle moment with the effects of the aerodynamic forces and inertia. We used this result, together with the pectoralis force magnitude, computed by balancing 1D power, to compute the pull angle of the pectoralis on the humerus during downstroke.

Like the power balance derivation, we needed to decide what the most effective scope to analyze angular momentum is: a single wing of the dove, or the entire dove. We decided to analyze the angular momentum of a single wing of the dove because fortunately, whereas the reaction force at the

shoulder joint is problematic for the power balance, it cancels out for the angular momentum balance. The base form of the 3D angular momentum balance equation is:

$$\vec{\mathbf{M}}^{\mathrm{W/O}} = \frac{{}^{\mathrm{N}}d\,{}^{\mathrm{N}}\vec{\mathbf{H}}^{\mathrm{W/O}}}{dt} + {}^{\mathrm{N}}\vec{\mathbf{v}}^{\mathrm{O}} \times {}^{\mathrm{N}}\vec{\mathbf{L}}^{\mathrm{W}}, \tag{S27}$$

where $\vec{\mathbf{M}}^{\mathrm{W/O}}$ is the sum of the moments on the wing (W: a system of particles and rigid bodies) about the shoulder joint (point O: fixed on the wing), ${}^{\mathrm{N}}\vec{\mathbf{H}}^{\mathrm{W/O}}$ is the angular momentum of the wing about the shoulder joint in the Newtonian reference frame, $\frac{{}^{\mathrm{N}}d}{dt}$ is the time derivative in the Newtonian reference frame, ${}^{\mathrm{N}}\vec{\mathbf{v}}^{\mathrm{O}}$ is the velocity of the shoulder joint in the Newtonian reference frame, and ${}^{\mathrm{N}}\vec{\mathbf{L}}^{\mathrm{W}}$ is the linear momentum of the wing in the Newtonian reference frame. Reaction forces at the shoulder joint do not create any moment about that shoulder joint, so we canceled that term. We eliminated any reaction torques by modelling the shoulder joint as a freely-rotating ball and socket joint with negligible friction. We also assumed negligible internal wing forces, such as muscles which bend the wrist or elbow. With the scope of the angular momentum balance decided, we expanded each side of Eqn. S27 to incorporate the effects of the muscles, aerodynamics, and inertia.

The terms on the right side of Eqn. S27 all relate to the distributed mass of the wing. The linear momentum of the wing in the Newtonian reference frame is:

$${}^{\mathrm{N}}\vec{\mathbf{L}}^{\mathrm{W}} = \sum_{\mathrm{i}=1}^{\mathrm{I_W}} m_{\mathrm{i}}\,{}^{\mathrm{N}}\vec{\mathbf{v}}^{\mathrm{i}}, \tag{S28}$$

where m_{i} is the ith of $\mathrm{I_W}$ bodies (or point masses) on the wing, and ${}^{\mathrm{N}}\vec{\mathbf{v}}^{\mathrm{i}}$ is the velocity vector of the ith body in the Newtonian reference frame. The angular momentum of the wing about the shoulder joint in the Newtonian reference frame is:

$${}^{\mathrm{N}}\vec{\mathbf{H}}^{\mathrm{W/O}} = \sum_{\mathrm{i}=1}^{\mathrm{I_W}} \left(\vec{\vec{\mathbf{I}}}^{\mathrm{W_i}} \cdot {}^{\mathrm{N}}\boldsymbol{\omega}^{\mathrm{W_i}} + \vec{\mathbf{r}}^{\mathrm{i/O}} \times m_{\mathrm{i}}\,{}^{\mathrm{N}}\vec{\mathbf{v}}^{\mathrm{i}} \right), \tag{S29}$$

where ${}^{\mathrm{N}}\boldsymbol{\omega}^{\mathrm{W_i}}$ is the angular velocity of the reference frame of the ith body in system W (the wing) relative to the Newtonian reference frame, $\vec{\vec{\mathbf{I}}}^{\mathrm{W_i}}$ is the moment of inertia of the ith body in system W relative to the center of mass of that body, and $\vec{\mathbf{r}}^{\mathrm{i/O}}$ is the position vector from the shoulder joint to the ith body in system W. Because we modeled the dove's wings using point masses, we simplified to:

$$ {}^{N}\vec{\mathbf{H}}^{W/O} = \sum_{i=1}^{I_W} \vec{\mathbf{r}}^{i/O} \times m_i \, {}^{N}\vec{\mathbf{v}}^{i} . \tag{S30} $$

Next, we expanded the left-hand side of Eqn. S27 which is the sum of the moments on the wing. This is made up of aerodynamic, gravitational, and muscle torques:

$$ \vec{\mathbf{M}}^{W/O} = \vec{\mathbf{M}}^{W/O}_{pect} + \vec{\mathbf{M}}^{W/O}_{supra} - \vec{\mathbf{M}}^{W/O}_{aero} + \vec{\mathbf{M}}^{W/O}_{g} , \tag{S31} $$

where $\vec{\mathbf{M}}^{W/O}_{aero}$ is the aerodynamic moment, $\vec{\mathbf{M}}^{W/O}_{g}$ is the gravitational moment, $\vec{\mathbf{M}}^{W/O}_{pect}$ is the pectoralis moment, and $\vec{\mathbf{M}}^{W/O}_{supra}$ is the supracoracoideus moment. Each of these terms equals the cross product of the vector from the shoulder joint to the location where the force acts crossed with the force vector. Hence, the gravitational moment term can be written as:

$$ \vec{\mathbf{M}}^{W/O}_{g} = \sum_{i=1}^{I_W} \vec{\mathbf{r}}^{i/O} \times \left(m_i \vec{\mathbf{g}} \right). \tag{S32} $$

This concludes the expansion of all terms related to mass in the angular momentum balance, and to summarize them, we defined a parameter called the inertial moment:

$$ \vec{\mathbf{M}}^{W/O}_{inertia} = \frac{{}^{N}d \, {}^{N}\vec{\mathbf{H}}^{W/O}}{dt} + {}^{N}\vec{\mathbf{v}}^{O} \times {}^{N}\vec{\mathbf{L}}^{W} - \vec{\mathbf{M}}^{W/O}_{g} , \tag{S33} $$

$$ \vec{\mathbf{M}}^{W/O}_{inertia} = \frac{{}^{N}d}{dt} \left(\sum_{i=1}^{I_W} \vec{\mathbf{r}}^{i/O} \times m_i \, {}^{N}\vec{\mathbf{v}}^{O} \right) + {}^{N}\vec{\mathbf{v}}^{O} \times \sum_{i=1}^{I_W} m_i \, {}^{N}\vec{\mathbf{v}}^{i} - \sum_{i=1}^{I_W} \vec{\mathbf{r}}^{i/O} \times \left(m_i \vec{\mathbf{g}} \right) . \tag{S34} $$

By grouping terms in this manner, the total muscle moment equals the inertial moment plus the aerodynamic moment:

$$ \vec{\mathbf{M}}^{W/O}_{pect} + \vec{\mathbf{M}}^{W/O}_{supra} = \vec{\mathbf{M}}^{W/O}_{inertia} + \vec{\mathbf{M}}^{W/O}_{aero} , \tag{S35} $$

similar to Eqn. S22 for the power balance.

The aerodynamic moment was challenging to compute because aerodynamic forces acted continuously along the wing. In order to solve for the aerodynamic moment simply in terms of the aerodynamic force on the wing and known parameters, we modeled the wing using blade elements:

$$ \vec{\mathbf{M}}^{W/O}_{aero} = -\sum_{j=1}^{J} \vec{\mathbf{r}}^{j/O} \times \vec{\mathbf{F}}_{aero,j} , \tag{S36} $$

where $\vec{\mathbf{r}}^{\,j/O}$ is the position vector from the shoulder joint to the quarter-chord location (a quarter of the way from the leading edge to the trailing edge) on the jth of J blade elements, and $\vec{\mathbf{F}}_{aero,j}$ is the aerodynamic force on the jth blade element. We expanded $\vec{\mathbf{F}}_{aero,j}$ to:

$$\vec{\mathbf{F}}_{aero,j} = -0.5\rho S_j \left(C_{L,j}\hat{\mathbf{L}}_j + C_{D,j}\hat{\mathbf{D}}_j \right) \left| {}^{N}\vec{\mathbf{v}}^{\,j} \right|^2, \tag{S37}$$

where the jth blade element has surface area, S_j, lift coefficient, $C_{L,j}$, lift direction, $\hat{\mathbf{L}}_j$, drag coefficient, $C_{D,j}$, drag direction, $\hat{\mathbf{D}}_j$, and velocity ${}^{N}\vec{\mathbf{v}}^{\,j}$. Assuming that the lift and drag coefficients and directions are spanwise invariant ($C_{L,j} = C_L$, $\hat{\mathbf{L}}_j = \hat{\mathbf{L}}$, $C_{D,j} = C_D$, and $\hat{\mathbf{D}}_j = \hat{\mathbf{D}}$ for all j), this reduces to:

$$\vec{\mathbf{M}}_{aero}^{W/O} = \sum_{j=1}^{J} \vec{\mathbf{r}}^{\,j/O} \times \left(0.5\rho S_j \left(C_L\hat{\mathbf{L}} + C_D\hat{\mathbf{D}} \right) \left| {}^{N}\vec{\mathbf{v}}^{\,j} \right|^2 \right), \tag{S38}$$

and further simplifies to:

$$\vec{\mathbf{M}}_{aero}^{W/O} = 0.5\rho \left(\sum_{j=1}^{J} S_j \left| {}^{N}\vec{\mathbf{v}}^{\,j} \right|^2 \vec{\mathbf{r}}^{\,j/O} \right) \times \left(C_L\hat{\mathbf{L}} + C_D\hat{\mathbf{D}} \right). \tag{S39}$$

In order to incorporate the total measured aerodynamic force on the wing, $\vec{\mathbf{F}}_{aero}$ into the equation for the aerodynamic moment, we simplified the aerodynamic moment to:

$$\vec{\mathbf{M}}_{aero}^{W/O} = -\vec{\mathbf{R}}^{AM/O} \times \vec{\mathbf{F}}_{aero} + \vec{\mathbf{T}}_O, \tag{S40}$$

where $\vec{\mathbf{R}}^{AM/O}$ is the position vector from the shoulder joint to the aerodynamic moment center, and $\vec{\mathbf{T}}_O$ accounts for extra torque due to paired, non-aligned forces. We assumed $\left|\vec{\mathbf{T}}_O\right| = 0$ based on the assumption that all of the lift and drag forces point in the same direction, and primarily act at locations along the wing that form a straight line starting at the shoulder joint. Using blade elements, we expanded $\vec{\mathbf{F}}_{aero}$, giving:

$$\vec{\mathbf{M}}_{aero}^{W/O} = \vec{\mathbf{R}}^{AM/O} \times \sum_{j=1}^{J} 0.5\rho S_j \left(C_{L,j}\hat{\mathbf{L}}_j + C_{D,j}\hat{\mathbf{D}}_j \right) \left| {}^{N}\vec{\mathbf{v}}^{\,j} \right|^2, \tag{S41}$$

and then simplified by assuming spanwise invariance in lift and drag coefficients and direction:

$$\vec{\mathbf{M}}_{aero}^{W/O} = 0.5\rho \left(\sum_{j=1}^{J} S_j \left| {}^{N}\vec{\mathbf{v}}^{\,j} \right|^2 \right) \vec{\mathbf{R}}^{AM/O} \times \left(C_L\hat{\mathbf{L}} + C_D\hat{\mathbf{D}} \right). \tag{S42}$$

By comparing Eqns. S39 and S42, we solved for $\vec{\mathbf{R}}^{AM/O}$:

$$0.5\rho\left(\sum_{j=1}^{J} S_j \left|{}^{N}\vec{\mathbf{v}}^{j}\right|^2 \vec{\mathbf{r}}^{j/O}\right)\times\left(C_L\hat{\mathbf{L}}+C_D\hat{\mathbf{D}}\right)=0.5\rho\left(\sum_{j=1}^{J} S_j \left|{}^{N}\vec{\mathbf{v}}^{j}\right|^2\right)\vec{\mathbf{R}}^{AM/O}\times\left(C_L\hat{\mathbf{L}}+C_D\hat{\mathbf{D}}\right), \quad \text{(S43)}$$

$$\vec{\mathbf{R}}^{AM/O}=\frac{\sum_{j=1}^{J} S_j \left|{}^{N}\vec{\mathbf{v}}^{j}\right|^2 \vec{\mathbf{r}}^{j/O}}{\sum_{j=1}^{J} S_j \left|{}^{N}\vec{\mathbf{v}}^{j}\right|^2}. \quad \text{(S44)}$$

The full expansion of the aerodynamic moment is:

$$\vec{\mathbf{M}}_{aero}^{W/O}=-\left(\frac{\sum_{j=1}^{J} S_j \left|{}^{N}\vec{\mathbf{v}}^{j}\right|^2 \vec{\mathbf{r}}^{j/O}}{\sum_{j=1}^{J} S_j \left|{}^{N}\vec{\mathbf{v}}^{j}\right|^2}\right)\times\vec{\mathbf{F}}_{aero}, \quad \text{(S45)}$$

which closely resembles Eqn. S17 for aerodynamic power. By incorporating this equation for the aerodynamic moment, Eqn. S35 can be used to solve for the moment that the flight muscles together must generate.

In order to compute the angle that the pectoralis pulls on the humerus, we used the computed pectoralis force magnitude from the 1D power balance and the muscle moment from the 3D angular momentum balance. We started by expanding the pectoralis moment:

$$\vec{\mathbf{M}}_{pect}^{W/O}=\vec{\mathbf{r}}^{P/O}\times\vec{\mathbf{F}}_{pect}, \quad \text{(S46)}$$

where $\vec{\mathbf{r}}^{P/O}$ is the vector from the shoulder joint to the deltopectoral crest where the pectoralis pulls on the humerus, and where $\vec{\mathbf{F}}_{pect}$ is the total pectoralis force. While the directions of $\vec{\mathbf{r}}^{P/O}$ and $\vec{\mathbf{F}}_{pect}$ were unknown and changed continuously through the stroke, we knew the magnitudes of both: $\left|\vec{\mathbf{r}}^{P/O}\right|$ from dissection and $\left|\vec{\mathbf{F}}_{pect}\right|$ from the 1D power balance. Hence, we used the following equation, derived from Eqn. S46, to solve for the effective pull ratio, $\sin\theta_p$, and the pectoralis pull angle on the humerus, θ_p:

$$\left|\vec{\mathbf{M}}_{pect}^{W/O}\right|=\sin\theta_p\left|\vec{\mathbf{r}}^{P/O}\right|\left|\vec{\mathbf{F}}_{pect}\right|, \quad \text{(S47)}$$

$$\theta_p=\sin^{-1}\left(\frac{\left|\vec{\mathbf{M}}_{pect}^{W/O}\right|}{\left|\vec{\mathbf{r}}^{P/O}\right|\left|\vec{\mathbf{F}}_{pect}\right|}\right). \quad \text{(S48)}$$

The next section details how we used this result to compute the full 3D pectoralis force vector.

Section S9: Determining the pectoralis pull direction

To determine the direction in which the pectoralis pulls on the humerus, we overlaid the skeleton of a dove on the measured 3D surface (Figs. 6, S10). Using Computed Tomography (CT), we scanned a dove skeleton of similar mass (170.2 g) to the four doves in this study, and then scaled the dimensions for each of the four doves to match the size of the dove we CT scanned. The scaling factor was the one third power of the ratio of each of the four dove's masses to the CT-scanned dove's mass. We assumed that the bones in the body of the dove (ribs, sternum, furcula, coracoid, and scapula) do not move relative to each other during flight. In reality, they do move, but not substantially compared to the movement of the wings [4], [50]. We also assumed that the bones in the wing consist of three rigid bone segments connected to each other: 1) the brachium (humerus), 2) the antebrachium (radius and ulna), and 3) the manus (radiale + ulnare + carpometacarpus + phalanges). The positions and orientations of the reference frames (joint axes) associated with each bone segment were determined based on the inertial axes of the bones and the joint anatomy [4], [50]. We assumed that all wing joints were free to rotate with 3 degrees of freedom and no translational degrees of freedom (measurements show that translation of the joints relative to the reference frame is minimal for modeling purposes) [4], [50]. The positioning of each joint was determined based on the centers of rotation [51] when previously-measured kinematics in chukars (*Alectoris chukar*; kinematics measured using X-Ray Reconstruction of Moving Morphology, i.e., XROMM) [4] were applied to the dove model. Muscle paths were modeled based on dissection of the CT-scanned dove. Pins were pushed into the body through the pectoralis and supracoracoideus in multiple locations along the central tendons, and pictures were taken *in situ* for multiple wing positions. Then the pectoralis and supracoracoideus were removed from the body, and the positions of the pins were re-photographed to visualize the paths of the tendons with respect to the skeleton. These paths were used to construct a simplified musculoskeletal model in SIMM (Software for Interactive Musculoskeletal Modeling), using wrapping surfaces to prevent the muscles from passing through bone.

We overlaid the musculoskeletal model, made up of four skeletal sections (one for the body and three for the left wing) onto the 3D surface of the dove during each flight in four stages.

1. First, we determined the position and orientation of the skeleton relative to the 3D surface of the body. We matched the orientation of the vertebral column with the pitch and yaw angles of 3D surface fit of the body (assuming zero roll), and we matched the plane of symmetry of the skeletal and 3D surface bodies. We positioned the skeletal shoulder joint as close as possible to

the average position (relative to the body of the dove) of the manually tracked shoulder joint, subject to the previous constraints.

2. Second, we rotated the humerus about the shoulder joint (rigidly attached to the dove's body) and the radius/ulna about the elbow joint (rigidly attached to the end of the humerus) until the end of the radius/ulna (the wrist joint) best matched the manually tracked wrist of the flying doves. Since rotation about the long axis of the humerus and the long axis of the radius/ulna do not impact the final position of the wrist from a purely geometric perspective (in reality, long axis rotation of the humerus partially determines how much abduction or adduction occurs at the elbow, which in turn determines the position of the wrist), this left two rotational axes of consequence for each bone segment: hence four rotational parameters to fit. Constraining the wrist joint to match between the skeletal and 3D surface models generates three constraints. For the fourth constraint, we rotated the humerus and radius/ulna so the deltopectoral crest and dorsal surfaces of the radius and ulna were approximately in the plane of the 3D surface of the wing. We then solved for these four rotational angles using a nonlinear least-squares regression, and smoothed the result [45], to find the orientations of the humerus and radius/ulna.
3. Third, we oriented the manus such that the most distal phalanx pointed toward the ninth primary wingtip (which was tracked).
4. Fourth, we allowed the humerus to rotate in the long axis so that the moment generated by the pectoralis best matched the required muscle moment, $\vec{\mathbf{M}}_{\text{pect}}^{\text{W/O}}$ when the pectoralis was shortening.

Using the overlaid skeleton, the pectoralis force magnitude, the pectoralis moment, and the pectoralis pull angle, we computed the time-resolved 3D force vector of the pectoralis. Examining Eqn. S46, the overlaid skeleton provides the missing information necessary to determine the vector from the shoulder joint to the deltopectoral crest where the pectoralis pulls on the humerus, $\vec{\mathbf{r}}^{\text{P/O}}$. With this information, we solved for the direction of the pectoralis force, $\vec{\mathbf{F}}_{\text{pect}} \Big/ \left|\vec{\mathbf{F}}_{\text{pect}}\right|$:

$$\frac{\vec{\mathbf{F}}_{\text{pect}}}{\left|\vec{\mathbf{F}}_{\text{pect}}\right|} = -R\left(\frac{\vec{\mathbf{M}}_{\text{pect}}^{\text{W/O}}}{\left|\vec{\mathbf{M}}_{\text{pect}}^{\text{W/O}}\right|}, -\theta_{\text{p}}\right) \cdot \frac{\vec{\mathbf{r}}^{\text{P/O}}}{\left|\vec{\mathbf{r}}^{\text{P/O}}\right|}, \tag{S49}$$

where $R(\mathbf{a}, \theta)$ is a function which outputs a rotation matrix corresponding to a rotation about axis $\mathbf{a}$ by an angle of θ. In other words, the direction of $\vec{\mathbf{F}}_{\text{pect}}$ is found by rotating the negative direction of $\vec{\mathbf{r}}^{\text{P/O}}$

about the direction of $\vec{\mathbf{M}}_{\text{pect}}^{\text{W/O}}$ by an angle of $-\theta_{\text{p}}$. Note that in order to compute the direction of $\vec{\mathbf{r}}^{\text{P/O}}$, only the orientation of the humerus is needed. The other skeletal segments (radius/ulna and manus) are computed for visualization purposes in the figures.

Section S10: Rules for modeling muscle power overlap

To address the modeling challenge of disentangling pectoralis and supracoracoideus muscle power during stroke-reversal, we considered the case where there is no elastic energy storage, and the muscles only generate or absorb power. Based on the sonomicrometry measurements of the pectoralis and total computed muscle power, each time-step during the stroke fell into one of four categories: 1) Positive total muscle power while the pectoralis was shortening. This was the case for much of the downstroke and indicated that the pectoralis was generating power. However, near stroke reversal, low pectoralis muscle velocity prevented high levels of power generation (see Eqn. S23). Hence, we restricted the maximum force production of pectoralis in stroke-reversal regions based on the maximum force produced by the pectoralis during the mid-downstroke. Any leftover total power is categorized as supracoracoideus power generation. 2) Negative total muscle power while the pectoralis was shortening. This was the case at the end of the upstroke and indicated that the supracoracoideus was acting as a brake by absorbing power. 3) Positive total muscle power while the pectoralis was lengthening. This was the case for much of the upstroke and indicated that the supracoracoideus was generating power. 4) Negative total muscle power while the pectoralis was lengthening. This was the case during the latter half of the upstroke when the wing was decelerating and indicated that the pectoralis was acting as a brake and absorbing power. However, similar to case 1, if pectoralis muscle velocity was too low to absorb the entirety of the total muscle power, we attributed the remainder to supracoracoideus power absorption.

Section S11: Modeling energy storage in the supracoracoideus tendon

To model energy storage in the supracoracoideus tendon, we considered how different amounts and timing of elastic energy storage in the tendon would impact the power distribution between the pectoralis and supracoracoideus. The two tuning parameters we varied are: 1) the proportion of supracoracoideus power which was elastically stored and released, and 2) the time period over which energy was stored in the supracoracoideus tendon. When we increased the first tuning parameter, we proportionally shifted the distribution of supracoracoideus power from generated to released (upstroke), and from absorbed to stored (downstroke). The power generated by the pectoralis was

correspondingly increased to ensure sufficient energy for the supracoracoideus tendon to store during the downstroke. To account for hysteresis effects [5] in the supracoracoideus tendon, the integrated extra power produced by the pectoralis must exceed the energy released by the supracoracoideus tendon by 7%. In order to estimate the temporal distribution of energy storage in the supracoracoideus, we assumed that the supracoracoideus lengthens according to measurements of ascending flight in pigeons (Fig. 2 of Tobalske and Biewener 2008 [5]). Specifically, we matched the timing of the pectoralis strain between our measurements and their measurements, in order to match the supracoracoideus strain and find when the supracoracoideus finishes lengthening. This timing, combined with our timing tuning parameter, defined the region of the stroke over which the supracoracoideus stores energy. Next, we assumed that the shape of the force-length curve of the supracoracoideus tendon matched the curve given in Millard *et al*. 2013 [52]. With this timing, strain, and force shape information, we calculated the shape of the power curve for the supracoracoideus tendon as a function of stroke percentage. We then scaled the magnitude of the power curve according to the amount of energy the supracoracoideus needed to store. By varying these two tuning parameters, we examined the effects of elastic energy storage in the supracoracoideus tendon on muscle performance.

Section S12: Scaling analysis across extant birds

We scaled our aerodynamic, inertial, and muscle measurements for doves across multiple extant birds, to estimate comparative patterns of power output during slow flight.

For each extant bird analyzed, we scaled our results for doves by modifying all relevant variables (see Tables S6-S10 for details), and plugging them directly into the relevant equations. We scaled the following variables based on extant data of 27 birds measured in literature [46]: body mass, m_{body}, wing mass (single wing), m_{wing}, wing moment of inertia (single wing), I_{wing}, wingspan (distance from shoulder joint to wingtip; single wing), $\left|\vec{\mathbf{r}}_{\text{span}}\right|$, distance from the shoulder joint to the center of gravity of the wing (single wing), $\left|\vec{\mathbf{r}}_{\text{wing,cg}}\right|$, wing area (single wing), S_{wing}, and wingbeat frequency, f. For four additional birds where data was missing, we used data from other sources [10], [53], scaled isometrically to match the body mass. For pectoralis mass (single pectoralis), m_{pect}, we isometrically scaled data in literature to match the body mass [5], [44], [53]. Finally, we assumed the following relationships for the following variables: time step for integration, Δt:

$$\Delta t \propto f^{-1}, \tag{S50}$$

aerodynamic force, $\vec{\mathbf{F}}_{\text{aero}}$:

$$\vec{\mathbf{F}}_{\text{aero}} \propto m_{\text{body}}, \tag{S51}$$

wing velocity (distributed), ${}^{\text{N}}\vec{\mathbf{v}}^{\text{i}}_{\text{wing}}$:

$${}^{\text{N}}\vec{\mathbf{v}}^{\text{i}}_{\text{wing}} \propto f\left|\vec{\mathbf{r}}_{\text{span}}\right|, \tag{S52}$$

and body velocity, ${}^{\text{N}}\vec{\mathbf{v}}_{\text{body}}$ equivalent to the doves. We calculated the point mass distribution in the wing, $m_{\text{wing,i}}$, using a least-squares fit to match wing mass, inertia, and center of gravity data. Additionally, to compare pectoralis electrical activation timing to our scaling parameters in Fig. 7D, we used the same procedure for 17 birds (Tables S7, S9-S10) [5], [8], [10], [11], [13]–[15], [44], [46], [53]–[59].

To interpret the scaling relationships, we traced the effects of scaling parameters in the aerodynamic power and moment equations. For aerodynamic power, we started with Eqns. S1 and S17 combined for some bird:

$${}^{\text{N}}P^{\text{aero}} = 2\vec{\mathbf{F}}_{\text{aero}} \cdot \left(\frac{\sum_{\text{j=1}}^{\text{J}} S_{\text{j}} \left| {}^{\text{N}}\vec{\mathbf{v}}^{\text{j}} \right|^2 {}^{\text{N}}\vec{\mathbf{v}}^{\text{j}}}{\sum_{\text{j=1}}^{\text{J}} S_{\text{j}} \left| {}^{\text{N}}\vec{\mathbf{v}}^{\text{j}} \right|^2} \right). \tag{S53}$$

Next, for each variable, we replaced it with an equivalent expression by utilizing the scaling relationships:

$${}^{\text{N}}P^{\text{aero}} = 2\tilde{\vec{\mathbf{F}}}_{\text{aero}} \frac{m_{\text{body}}}{\tilde{m}_{\text{body}}} \cdot \left(\frac{\sum_{\text{j=1}}^{\text{J}} \tilde{S}_{\text{j}} \frac{S_{\text{wing}}}{\tilde{S}_{\text{wing}}} \left| {}^{\text{N}}\tilde{\vec{\mathbf{v}}}^{\text{j}} \frac{f\left|\vec{\mathbf{r}}_{\text{span}}\right|}{\tilde{f}\left|\tilde{\vec{\mathbf{r}}}_{\text{span}}\right|} \right|^2 {}^{\text{N}}\tilde{\vec{\mathbf{v}}}^{\text{j}} \frac{f\left|\vec{\mathbf{r}}_{\text{span}}\right|}{\tilde{f}\left|\tilde{\vec{\mathbf{r}}}_{\text{span}}\right|}}{\sum_{\text{j=1}}^{\text{J}} \tilde{S}_{\text{j}} \frac{S_{\text{wing}}}{\tilde{S}_{\text{wing}}} \left| {}^{\text{N}}\tilde{\vec{\mathbf{v}}}^{\text{j}} \frac{f\left|\vec{\mathbf{r}}_{\text{span}}\right|}{\tilde{f}\left|\tilde{\vec{\mathbf{r}}}_{\text{span}}\right|} \right|^2} \right), \tag{S54}$$

where variables with a tilde represent a second bird. When we reduced this expression, we recovered the equation for aerodynamic power for the second bird:

$${}^{\text{N}}P^{\text{aero}} = \left(\frac{m_{\text{body}}}{\tilde{m}_{\text{body}}} \frac{f\left|\vec{\mathbf{r}}_{\text{span}}\right|}{\tilde{f}\left|\tilde{\vec{\mathbf{r}}}_{\text{span}}\right|} \right) 2\vec{\mathbf{F}}_{\text{aero}} \cdot \left(\frac{\sum_{\text{j=1}}^{\text{J}} \tilde{S}_{\text{j}} \left| {}^{\text{N}}\tilde{\vec{\mathbf{v}}}^{\text{j}} \right|^2 {}^{\text{N}}\tilde{\vec{\mathbf{v}}}^{\text{j}}}{\sum_{\text{j=1}}^{\text{J}} \tilde{S}_{\text{j}} \left| {}^{\text{N}}\tilde{\vec{\mathbf{v}}}^{\text{j}} \right|^2} \right), \tag{S55}$$

which led us to the scaling relationship for aerodynamic power:

$$\frac{{}^{\text{N}}P^{\text{aero}}}{{}^{\text{N}}\tilde{P}^{\text{aero}}} = \frac{m_{\text{body}}}{\tilde{m}_{\text{body}}} \frac{f\left|\vec{\mathbf{r}}_{\text{span}}\right|}{\tilde{f}\left|\tilde{\vec{\mathbf{r}}}_{\text{span}}\right|}, \tag{S56}$$

$$ {}^{\mathrm{N}}P^{\mathrm{aero}} \propto m_{\mathrm{body}} f \left| \vec{\mathbf{r}}_{\mathrm{span}} \right| . \tag{S57} $$

We then rearranged this equation to form interpretable parameters:

$$ \frac{{}^{\mathrm{N}}P^{\mathrm{aero}}}{m_{\mathrm{body}}} \propto f \left| \vec{\mathbf{r}}_{\mathrm{span}} \right| , \tag{S58} $$

where $f \left| \vec{\mathbf{r}}_{\mathrm{span}} \right|$ is proportional to wingtip speed. Using the same technique, we find the scaling relationship for the aerodynamic moment:

$$ \frac{\vec{\mathbf{M}}_{\mathrm{aero}}^{\mathrm{W/O}}}{m_{\mathrm{body}}} \propto \left| \vec{\mathbf{r}}_{\mathrm{span}} \right| . \tag{S59} $$

Interpreting the effects of the scaling relationships on the inertial power and moments was more challenging. For inertial power, we started with Eqn. S21 for some bird:

$$ {}^{\mathrm{N}}P^{\mathrm{inertia}} = \frac{1}{2} \frac{d}{dt} m_{\mathrm{body}} {}^{\mathrm{N}}\vec{\mathbf{v}}_{\mathrm{body}} \cdot {}^{\mathrm{N}}\vec{\mathbf{v}}_{\mathrm{body}} + \frac{1}{2} \frac{d}{dt} \left(\sum_{\mathrm{i}=1}^{\mathrm{I_W}} m_{\mathrm{wing,i}} {}^{\mathrm{N}}\vec{\mathbf{v}}_{\mathrm{wing}}^{\mathrm{i}} \cdot {}^{\mathrm{N}}\vec{\mathbf{v}}_{\mathrm{wing}}^{\mathrm{i}} \right) + \sum_{\mathrm{i}=1}^{\mathrm{I_{W,B}}} m_{\mathrm{i}} g \, {}^{\mathrm{N}}v_{\mathrm{z}}^{\mathrm{i}} , \tag{S60} $$

where the point masses representing the body and wings were expanded from Eqn. S21. The gravity power was negligible so we ignored it, and the scaling relationship for the inertial power due to the movement of the body is simple:

$$ {}^{\mathrm{N}}P_{\mathrm{body}}^{\mathrm{inertia}} \propto m_{\mathrm{body}} , \tag{S61} $$

because the body velocity was unchanged in our scaling analysis. However, the inertial term for the wing is more complex because of the time derivative and because the point masses do not scale proportionately. To incorporate the moment of inertia of the wing, which does scale proportionately, we expanded the velocity terms. We started by assuming that the stroke angle, ϕ, could be written as:

$$ \phi = -\Phi \cos\left(2\pi f t\right), \tag{S62} $$

where Φ is the stroke amplitude angle. We then differentiated the stroke angle so that the velocity of the point masses could be written as:

$$ {}^{\mathrm{N}}\vec{\mathbf{v}}_{\mathrm{wing}}^{\mathrm{i}} = \dot{\phi} \vec{\mathbf{r}}_{\mathrm{wing}}^{\mathrm{i/O}} = \Phi 2\pi f \sin\left(2\pi f t\right) \vec{\mathbf{r}}_{\mathrm{wing}}^{\mathrm{i/O}} . \tag{S63} $$

When we plugged this into the power equation:

$$ {}^{\mathrm{N}}P_{\mathrm{wing}}^{\mathrm{inertia}} = \frac{1}{2} \frac{d}{dt} \left(\sum_{\mathrm{i}=1}^{\mathrm{I_W}} m_{\mathrm{wing,i}} \left| \Phi 2\pi f \sin\left(2\pi f t\right) \vec{\mathbf{r}}_{\mathrm{wing}}^{\mathrm{i/O}} \right|^2 \right), \tag{S64} $$

and simplified:

$$ {}^{\mathrm{N}}P_{\mathrm{wing}}^{\mathrm{inertia}} = \frac{1}{2} \left(\Phi 2\pi f\right)^2 \frac{d}{dt} \left(\sin^2\left(2\pi f t\right) \sum_{\mathrm{i}=1}^{\mathrm{I_W}} m_{\mathrm{wing,i}} \left| \vec{\mathbf{r}}_{\mathrm{wing}}^{\mathrm{i/O}} \right|^2 \right), \tag{S65} $$

we found that the moment of inertia of the wing appeared:

$$ {}^{\mathrm{N}}P_{\mathrm{wing}}^{\mathrm{inertia}} = \frac{1}{2}\left(\Phi 2\pi f\right)^2 \frac{d}{dt}\left(\sin^2\left(2\pi ft\right) I_{\mathrm{wing}}\right). \tag{S66} $$

After differentiating the expression, we arrived at the following simplified equation:

$$ {}^{\mathrm{N}}P_{\mathrm{wing}}^{\mathrm{inertia}} = 8\Phi^2\pi^3 f^3 I_{\mathrm{wing}} \sin\left(2\pi ft\right), \tag{S67} $$

from which we can easily see that:

$$ {}^{\mathrm{N}}P_{\mathrm{wing}}^{\mathrm{inertia}} \propto f^3 I_{\mathrm{wing}}. \tag{S68} $$

Assuming that the inertial power from the wing dominated the inertial power from the body, we can summarize in the following interpretable format:

$$ \frac{{}^{\mathrm{N}}P^{\mathrm{inertia}}}{m_{\mathrm{body}}} \propto \frac{m_{\mathrm{wing}}}{m_{\mathrm{body}}}\left(\frac{r_{\mathrm{gyr}}}{\left|r_{\mathrm{span}}\right|}\right)^2 \left(f\left|r_{\mathrm{span}}\right|\right)^2 f, \tag{S69} $$

where r_{gyr} is the radius of gyration of the wing ($I_{\mathrm{wing}} = m_{\mathrm{wing}} r_{\mathrm{gyr}}^2$). For the inertial moment, we conducted a similar analysis, assuming that the angular momentum term dominated, producing the following scaling relationship:

$$ \frac{\vec{\mathbf{M}}_{\mathrm{inertia}}^{\mathrm{W/O}}}{m_{\mathrm{body}}} \propto \frac{m_{\mathrm{wing}}}{m_{\mathrm{body}}}\left(\frac{r_{\mathrm{gyr}}}{\left|r_{\mathrm{span}}\right|}\right)^2 \left(f\left|r_{\mathrm{span}}\right|\right)^2. \tag{S70} $$

For easier discussion of the different scaling factors which relate to inertial and aerodynamic power and moments, we defined new scaling parameters. We defined the aerodynamic power scaling parameter, $x_{\mathrm{p,aero}}$, which is proportional to the wingtip velocity as:

$$ x_{\mathrm{p,aero}} = f\left|\vec{\mathbf{r}}_{\mathrm{span}}\right|. \tag{S71} $$

We defined the aerodynamic moment scaling parameter, $x_{\mathrm{m,aero}}$, as the wingspan:

$$ x_{\mathrm{m,aero}} = \left|\vec{\mathbf{r}}_{\mathrm{span}}\right| = \frac{x_{\mathrm{p,aero}}}{f}. \tag{S72} $$

We defined the inertial power scaling parameter, $x_{\mathrm{p,iner}}$, as proportional to the product of the wing mass ratio, times the wing radius of gyration ratio squared, times the wingtip velocity squared, times the wingbeat frequency:

$$ x_{\mathrm{p,iner}} = \frac{m_{\mathrm{wing}}}{m_{\mathrm{body}}}\left(\frac{r_{\mathrm{gyr}}}{\left|r_{\mathrm{span}}\right|}\right)^2 \left(f\left|r_{\mathrm{span}}\right|\right)^2 f. \tag{S73} $$

Finally, we defined the inertial moment scaling parameter, $x_{\mathrm{m,iner}}$, as proportional to the product of the wing mass ratio, times the wing radius of gyration ratio squared, times the wingtip velocity squared:

$$x_{\mathrm{m,iner}} = \frac{m_{\mathrm{wing}}}{m_{\mathrm{body}}}\left(\frac{r_{\mathrm{gyr}}}{\left|r_{\mathrm{span}}\right|}\right)^2\left(f\left|r_{\mathrm{span}}\right|\right)^2 = \frac{x_{\mathrm{p,iner}}}{f}. \tag{S74}$$

Additionally, in Fig. 7B,D we use the following expression to quantify the midway point of the pectoralis power exertion, $T_{\mathrm{P,mid}}^{\mathrm{pect}}$:

$$T_{\mathrm{P,mid}}^{\mathrm{pect}} = \frac{\int_{t_{\mathrm{Down\text{-}start}}}^{t_{\mathrm{Down\text{-}end}}} {}^{\mathrm{N}}P^{\mathrm{pect}} t\,dt}{\int_{t_{\mathrm{Down\text{-}start}}}^{t_{\mathrm{Down\text{-}end}}} {}^{\mathrm{N}}P^{\mathrm{pect}}\,dt} \times 100\%, \tag{S75}$$

and the midway point of the pectoralis force exertion, $T_{\mathrm{F,mid}}^{\mathrm{pect}}$:

$$T_{\mathrm{F,mid}}^{\mathrm{pect}} = \frac{\int_{t_{\mathrm{Down\text{-}start}}}^{t_{\mathrm{Down\text{-}end}}} {}^{\mathrm{N}}F^{\mathrm{pect}} t\,dt}{\int_{t_{\mathrm{Down\text{-}start}}}^{t_{\mathrm{Down\text{-}end}}} {}^{\mathrm{N}}F^{\mathrm{pect}}\,dt} \times 100\%, \tag{S76}$$

where $t_{\mathrm{Down\text{-}start}}$ and $t_{\mathrm{Down\text{-}end}}$ are the starting and ending times of the downstroke. To convert the ratio into a percentage, we multiply by 100%, since these points represent timing relative to stroke percentage.

Supplementary Figures

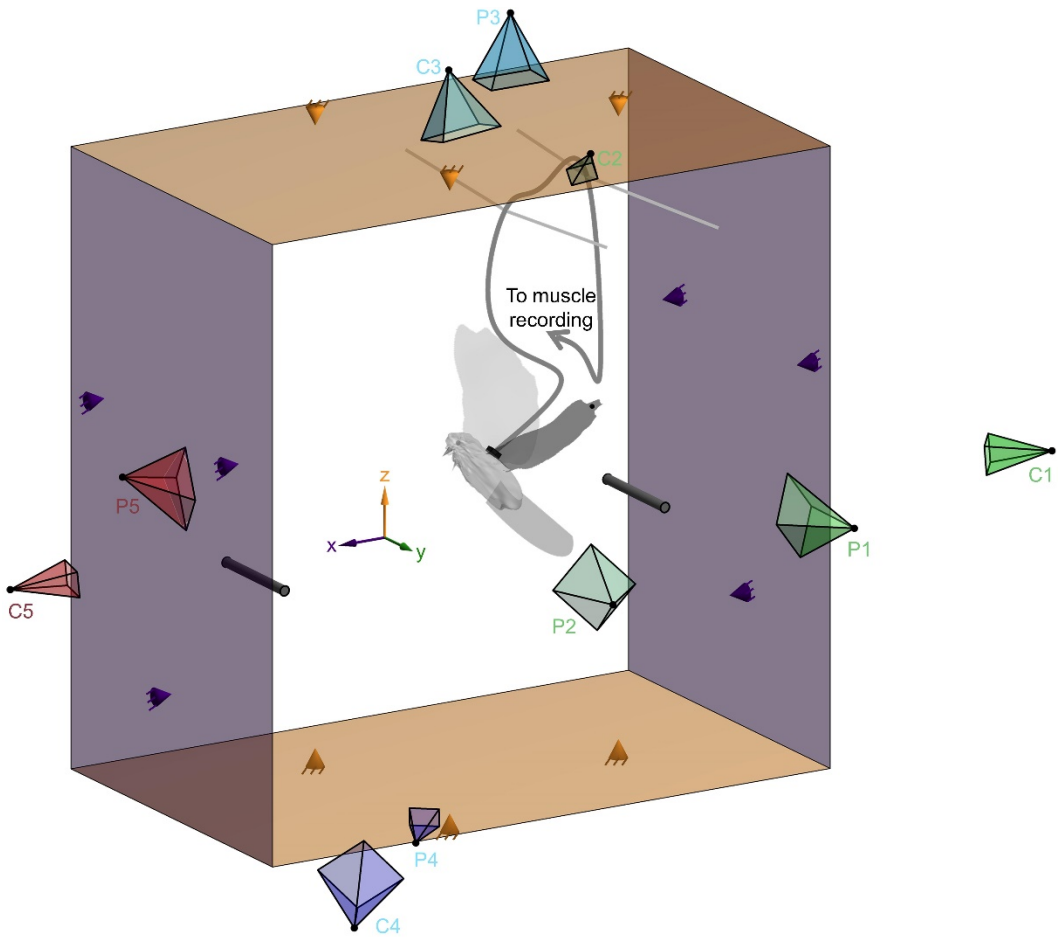

Figure S1. Simultaneous measurement of the electrical activation and strain of the pectoralis muscle, the horizontal and vertical aerodynamic forces, and the 3D wing, body and tail surface of doves in slow forward flight enabled us to reconstruct the aerodynamic work loop of the pectoralis. The dove flew from the right perch to the left perch inside the 2D aerodynamic force platform (AFP) [31]–[33], [43], [60]. Force panels above and below the dove (orange) measured the time-resolved vertical aerodynamic force, and panels behind and in front of the dove (purple) measured the time-resolved horizontal aerodynamic force generated by the dove to fly. Each of the four panels was connected in a statically determined manner to three force sensors (orange and purple cones). Five pairs of high-speed cameras (C1–C5; cameras further from the dove appear smaller) and projectors (P1–P5) imaged the body, tail and left wing of the dove from different view angles during the second stroke after takeoff [27]. We assumed bilateral symmetry for the right wing, because we focused our cameras and projectors on the left wing, during the second stroke after takeoff, to optimally resolve the wing's 3D surface during a full wingbeat. The wire (dark gray curving line) used to measure the electrical activation (electromyography) and strain (sonomicrometry) of the pectoralis muscle was attached to the back plug (black rectangle). The plug was secured to the back by suturing its base to intervertebral ligaments. This wire was loosely supported by strings mounted near the top of the AFP (two light gray lines), exiting the AFP through a small hole in the acrylic side panel (labeled "to muscle recording").

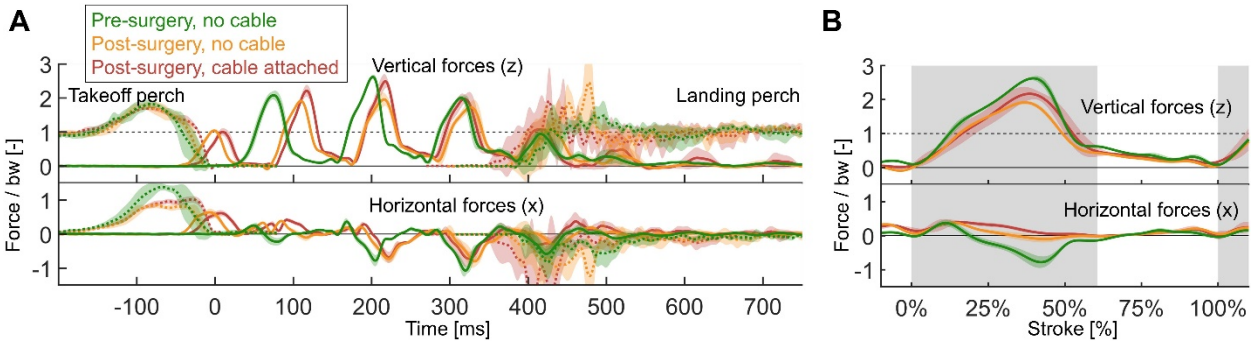

Figure S2. Comparison of aerodynamic and perch forces prior to surgery and after surgery shows that the surgery substantially altered the flight performance. Pre-surgery flights are plotted in green, post-surgery flights without the recoding cable connected to the dove are plotted in yellow, and post-surgery flights with the connected muscle recording cable (EMG and sonomicrometry) are plotted in red. For all three flight scenarios, we averaged five flights from dove 3. (Plots show average and standard deviation across 5 flights; gray region indicates second downstroke after takeoff). (A) The aerodynamic and perch forces across the entire flight (similar to Figs. 1B, S3). (B) The aerodynamic forces generated by the second wingbeat (similar to Fig. 1A) during which we 3D reconstructed the dove's body surface in flight.

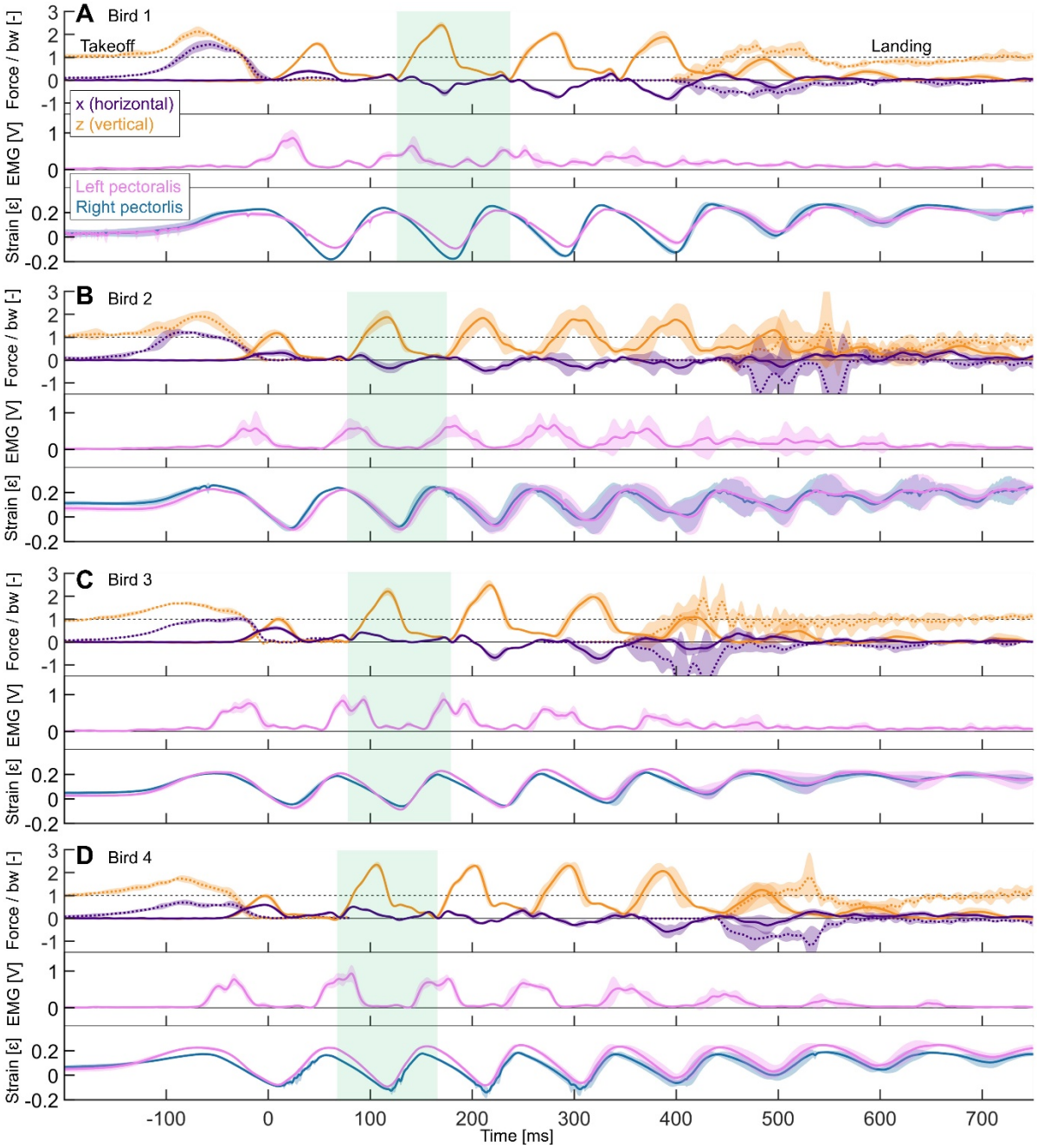

Figure S3. Measured data is plotted for each of the four doves individually, averaged over five flights per dove. (Shaded regions: standard deviation). The data plotted is similar to Fig. 1B where data from a single flight was plotted. For each dove, we plot the horizontal (x, purple) and vertical (z, orange) aerodynamic forces (solid lines), the horizontal and vertical takeoff and landing forces (dotted lines), the pectoralis electrical activation (pink: left pectoralis), and the pectoralis strain (pink: left pectoralis; blue: right pectoralis). Manual temporal alignment is based on the instant the dove takes off. All summary figures use data from the second wingbeat after takeoff (green shaded regions). (A) Five averaged flights

by dove 1. (B) Five averaged flights by dove 2. (C) Five averaged flights by dove 3. (D) Five averaged flights by dove 4.

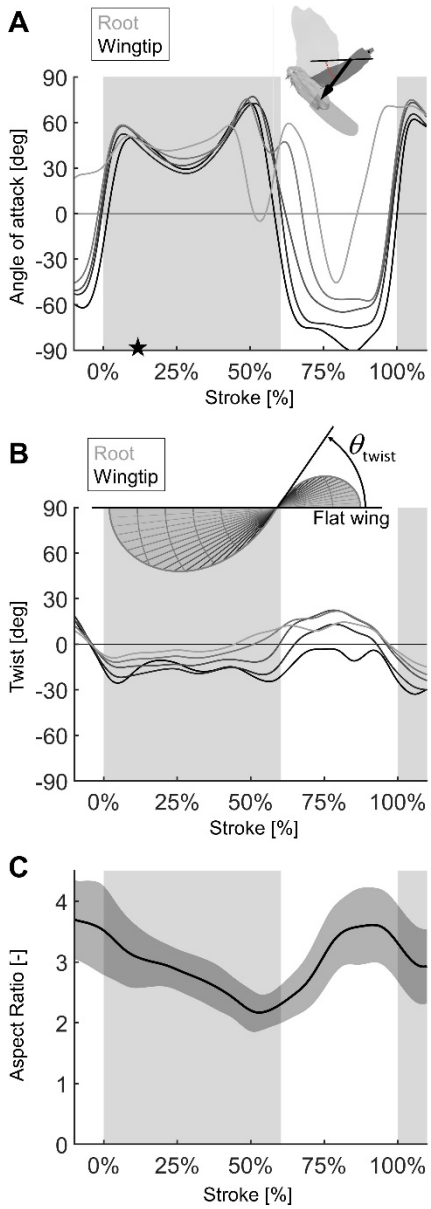

Figure S4. Stroke-resolved wing morphing parameters during the second wingbeat, measured using 3D wing surface reconstruction. (*N* = 4 doves; *n* = 5 flights each; gray region indicates second downstroke after takeoff). (A) The angle of attack induced by flapping motion varies through the stroke, and in a lesser degree, along the span. We computed the angle of attack for each blade element as the angle between the chordline of the blade element (avatar: thin black line) and the velocity vector (avatar: thick black line) and plot the results at 20% (labeled as root), 40%, 60%, 80%, and 100% (labeled as tip)

of the wing radius. (B) Wing twist, the angle between the chord vector at the root and the chord vector along the span of the wing, is plotted at 20% (labeled as root), 40%, 60%, 80%, and 100% (labeled as tip) of the wing radius. The diagram shows a twisted elliptical wing viewed with the wingspan axis out of the page. (C) The aspect ratio of the wing was computed using Eqn. S4 and quantifies the ratio of the wingspan squared and the wing surface area. Hence, the normalized aspect ratio is Fig. 2E squared divided by Fig. 2D. The aspect ratio peak near the end of the upstroke corresponds to the dove beginning to re-extend its wing to prepare for the downstroke, even while its feathers are still splayed to maintain low surface area.

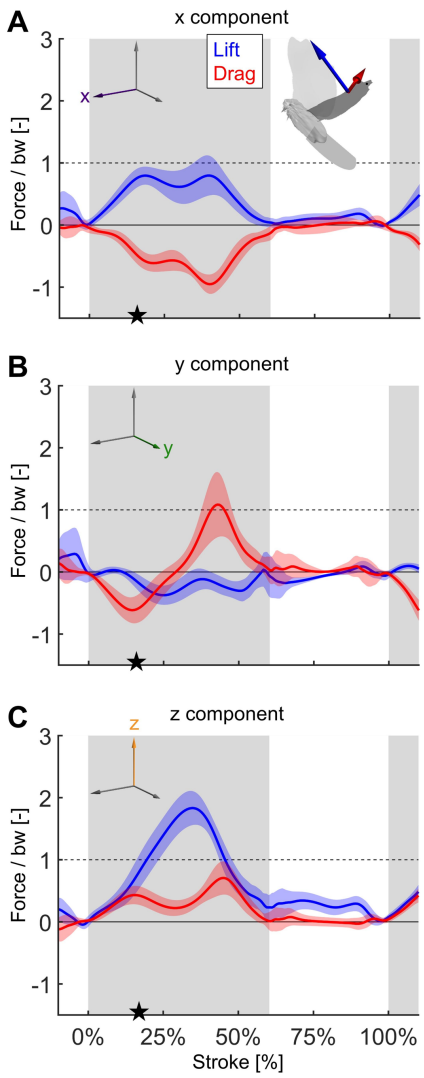

Figure S5. The components of lift and drag expand our understanding from Fig. 3B. (A) The horizontal component of lift points forward to overcome the horizontal component of drag throughout the stroke. (B) The lateral component of drag peaks near the end of downstroke, which together with the peak in

the horizontal and vertical components contributes to slowing down the wing. (C) The vertical drag component contributes substantially, 22.1%, to weight support over the stroke. The stroke-averaged vertical force normalized by bodyweight is 87.3%, showing the second wingbeat does not fully support bodyweight. Body weight is supported for the entire flight using the combined work of the legs and wings. See Tables S4 and S5 for a complete breakdown of stroke-averaged aerodynamic forces across all experiments.

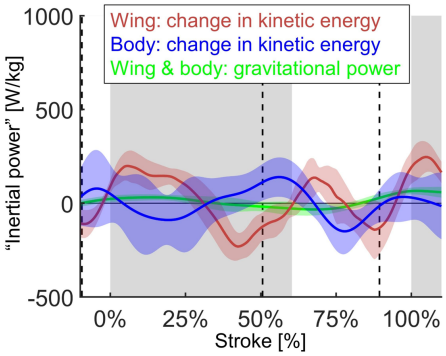

Figure S6. The inertial power is the sum of three components. The first component, gravitational power (green; negative gravitational power plotted), which accounts for the combined mass of the wings and body of the bird moving vertically, is comparatively small (11.6% ± 2.8% stroke-averaged magnitude compared to total inertial power). In contrast, the second component, the inertial power due to the acceleration of the wings (red) contributes substantially (48.5% ± 10.5% stroke-averaged magnitude compared to total inertial power). Muscle power to accelerate the wing at the beginning of downstroke and upstroke is positive, and negative when decelerating the wing at the end of the downstroke. The final component is the inertial power due to small accelerations of the body of the bird (blue). Because the mass of the body is high compared to the wing, and because the second derivative of position is highly sensitive, the standard deviation is high for this component of inertial power (the stroke-averaged standard deviation is 69.9% of the average magnitude). The effect of this final component is to shift the phase of the inertial power earlier in the stroke than if only the wings were considered (earlier by 10.5% ± 5.8% of the stroke). The result is that the zero-crossings of the inertial power are more closely aligned with the zero-crossings of the pectoralis muscle velocity (Fig. 4B).

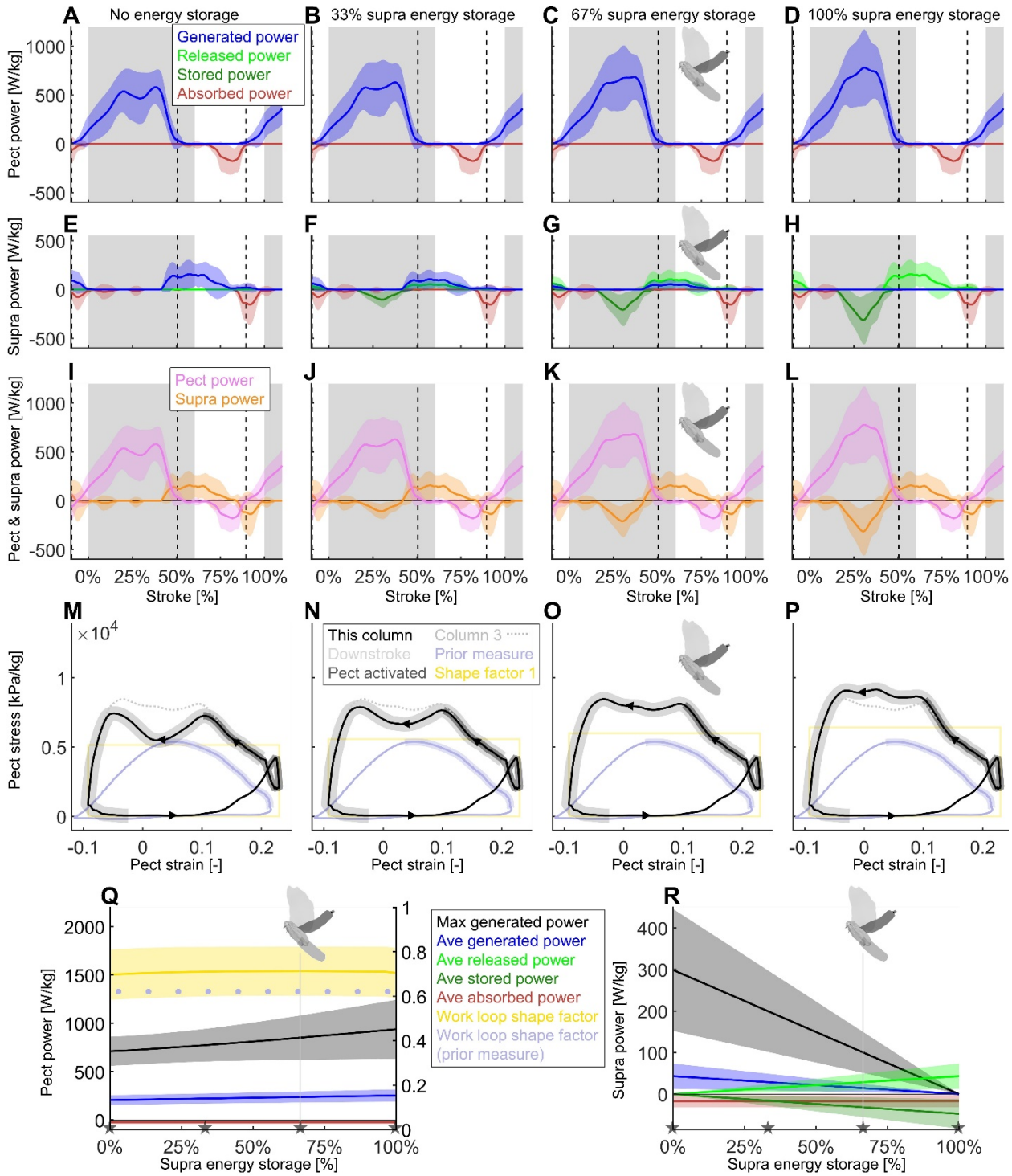

Figure S7. Using our energy storage model (Fig. 5A), we analyze how differing amounts of energy storage in the supracoracoideus tendon would affect how the total time-resolved required muscle power (Fig. 4B) is split between the pectoralis and supracoracoideus. To isolate the effect of energy storage amount, which is an important question in literature [5], we set the timing of the energy storage constant for now. Specifically, we vary the prescribed fraction of power that the supracoracoideus

1361 tendon stores for release during the upstroke, and model the pectoralis to produce and transfer this
1362 extra power into the supracoracoideus tendon during the mid-to-late downstroke. We find that a power
1363 increase of 24.9% ± 17.5% in the pectoralis muscle would enable it to fully power the upstroke by
1364 tensioning the supracoracoideus tendon during the downstroke. The color-scheme for the two positive
1365 and two negative power modes are: blue for generated power (the muscle needs to fully produce this
1366 positive power), bright green for released power (the muscle has elastic energy stored up that it can
1367 release as positive power), dark green for stored power (the muscle elastically stores negative power),
1368 and red for dissipated power (the muscle absorbs this negative power, acting as a brake). (*N* = 4 doves; *n*
1369 = 5 flights each; gray region indicates second downstroke after takeoff; all power scaled by pectoralis
1370 mass; vertical dashed lines indicate pectoralis strain rate equals zero). (A-D) The mid-downstroke dip in
1371 power generated by the pectoralis (pect), is flattened as extra power is generated and transferred to
1372 tension the supracoracoideus. (E-H) When the pectoralis tensions the supracoracoideus tendon during
1373 the downstroke, the supracoracoideus (supra) does not need to generate as much power during the
1374 upstroke. (I-L) Time-resolved pectoralis (pink) and supracoracoideus (orange) total power, each scaled
1375 by the pectoralis mass, is summarized from rows one and two respectively. Total power equals the
1376 summation of the power from the four power modes. By transferring pectoralis power into the
1377 supracoracoideus tendon and storing it as potential energy, the pectoralis power buildup does not have
1378 to dip midstroke. (M-P) The shape factor (ratio of the observed area to the area of a rectangle with the
1379 same range of stress and strain; yellow rectangle shows the work loop with a shape factor of one with
1380 the same range of strain) of the pectoralis work loop improves locally as the energy storage fraction
1381 increases and flattens the mid-downstroke dip in pectoralis power. The modeled work loop of the
1382 pectoralis (black) is compared to the work loop for 67% supracoracoideus energy storage (column 3,
1383 light gray; corresponds to the dove avatar in Q and R). The portions of the work loop corresponding to
1384 electrical activation of the pectoralis are shaded in dark gray, while the downstroke is shaded light gray.
1385 We also compare our derived pectoralis work loop to the work loop measured for doves in similar
1386 conditions using a strain gauge mounted on the deltopectoral crest (DPC) of the humerus to estimate
1387 pectoralis stress (light blue) [3]. The present pectoralis work loop shape factor is 0.70 according to our
1388 baseline recordings (no elastic storage added) whereas the earlier value based on DPC strain gauge
1389 recordings was 0.62. The strain gauge-based recordings also underestimate the required stress level to
1390 sustain the external aerodynamic and inertial power in vivo (especially considering our analysis excludes
1391 minor additional internal musculoskeletal power transfer losses). (Q) As the fraction of elastically-stored
1392 supracoracoideus power increases, the stroke-averaged absorbed pectoralis power remains constant,

while the stroke-averaged generated power increases by up to 24.9% ± 17.5%. The maximum generated pectoralis power (black) increases even more (31.9%), based on the peak required to tension the supracoracoideus tendon during the late downstroke. Notably the pectoralis work loop shape factor remains relatively constant throughout, because its value lower than 1 is primarily caused by the simultaneous pectoralis strain rate and power buildup around the start of the downstroke (5C). (R) As the fraction of elastically-stored supracoracoideus power increases, the stroke-averaged released power increases linearly, allowing the stroke-averaged generated power and maximum generated power (black) to decrease linearly. The gray stars in Q and R correspond to the four storage cases in the associated columns A–P.

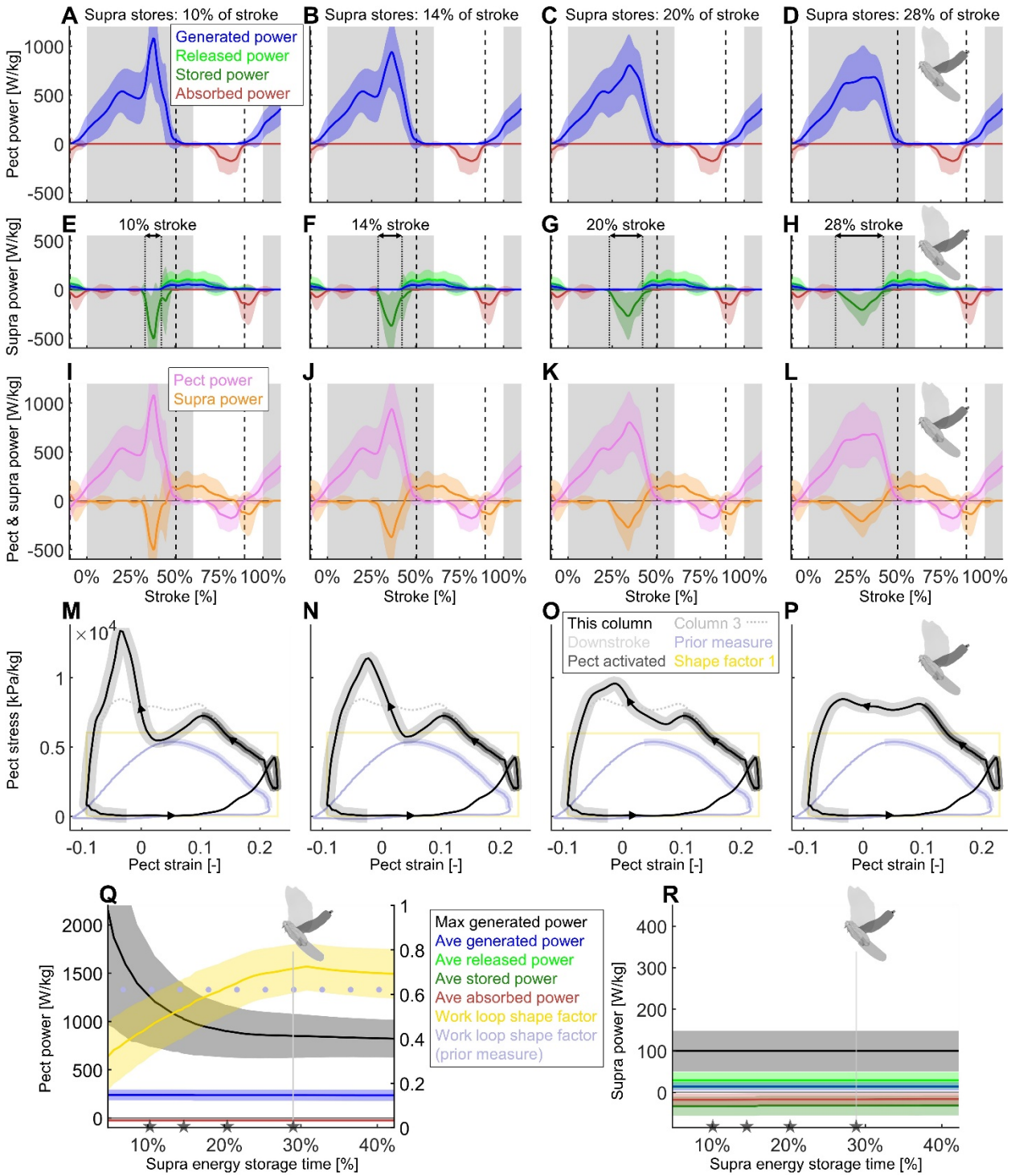

Figure S8. Using our energy storage model (Fig. 5A), we find that spreading out the energy storage in the supracoracoideus tendon during the downstroke substantially improves the shape factor of the pectoralis muscle work loop by better flattening the mid-downstroke dip in required muscle power (Fig. 4B)—resulting in a peak shape factor of 0.73. Whereas in Fig. S7, we varied the energy storage fraction, now we hold energy storage constant at 67% (column 3 of Fig. S7), and vary the less considered and

more nuanced timing of the energy storage in the supracoracoideus tendon during the downstroke. (Format of this figure is the same as Fig. S7; column 4 of this figure is identical to column 3 of Fig. S7: dove avatar in Q and R indicates identical parameters from column 3 of Fig. S7). (E-H) Vertical dotted lines are added to highlight the varying timing of energy storage in the supracoracoideus tendon. (A,E,I,M) If the supracoracoideus tendon is tensioned rapidly (10% the length of the stroke; 17% the length of the downstroke), this causes a costly late-downstroke spike in pectoralis power generation. (B,F,J,N) If the supracoracoideus tendon is tensioned over a longer portion of the downstroke (14% the length of the stroke; 23% of the downstroke), late-downstroke spike in pectoralis power generation is lessened. (C,G,K,O) This trend continues as the supracoracoideus tensioning is spread out more (20% the length of the stroke; 33% of the downstroke). (D,H,L,P) If the supracoracoideus tendon is tensioned over 28% of the stroke (46% of the downstroke), the spike in pectoralis power needed for energy storage overlaps the mid-downstroke dip in required muscle power (Fig. 4B). Hence, the mid-downstroke pectoralis power is smoother, and more closely resembles direct pectoralis power measurements for other birds [5]. (Q,R) The stroke-averaged power remains constant when all that changes is the timing of the elastic storage. However, the peak generated pectoralis power is higher when the elastic storage region is short. (Q) The pectoralis work loop shape factor is maximized when the supracoracoideus storage time is more spread out over the downstroke. The gray stars in Q and R correspond to the four storage cases in the associated columns A–P.

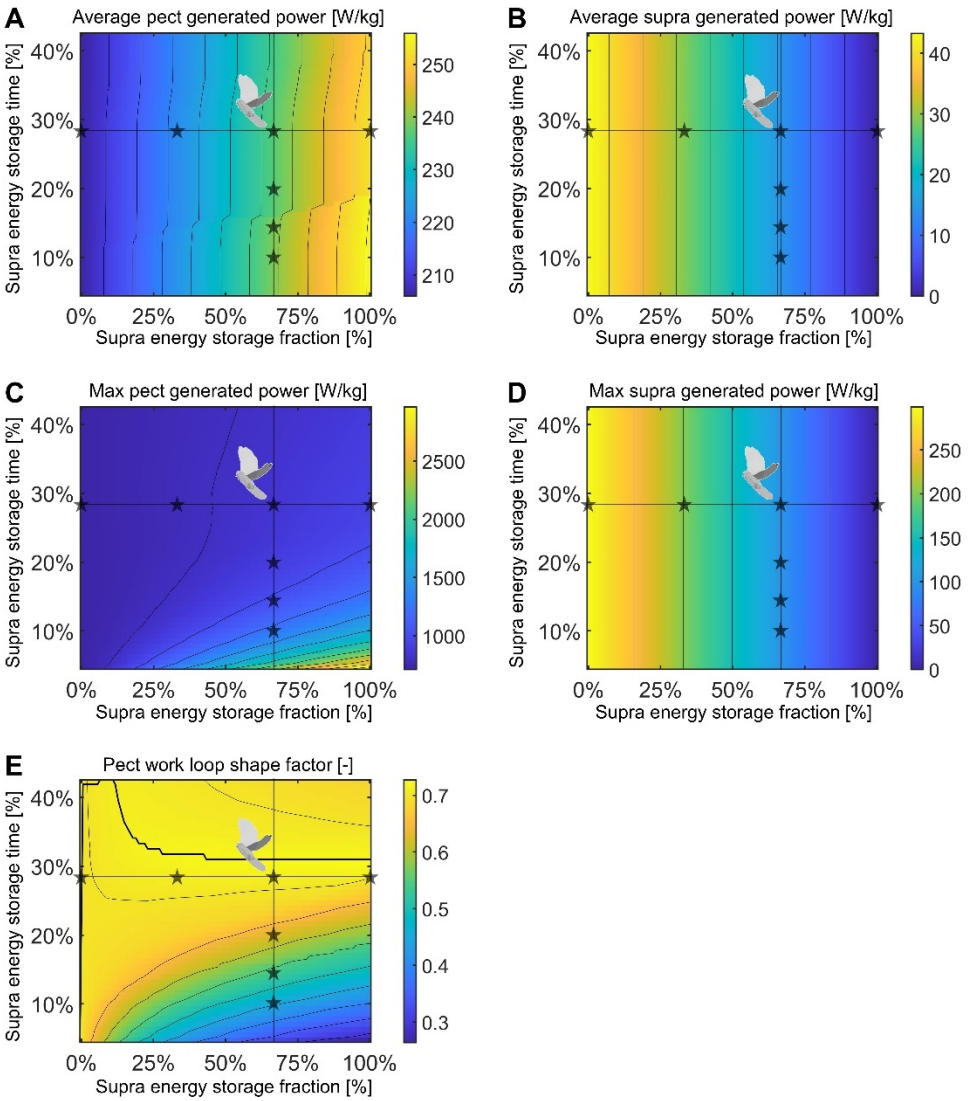

Figure S9. Using our energy storage model (Fig. 5A), we find that for supracoracoideus energy storage fractions above 35%, a pectoralis work loop shape factor of over 0.72 can be achieved by spreading the storage time in the supracoracoideus tendon out over 31% of the stroke. To gain insight into the tradeoffs between generated muscle power and elastic energy release, we vary two parameters in this model: the fraction of supracoracoideus power which is elastically stored and released (x-axis; columns in Fig. S7 correspond to stars along the horizontal lines; 100 grid points), and the time period over which energy is stored in the supracoracoideus tendon (y-axis; columns in Fig. S8 correspond to stars along the vertical lines; 51 grid points). (A) The stroke-averaged pectoralis generated power is mostly a function of the energy storage fraction, and increases gradually as energy storage is increased. (B) The stroke-averaged supracoracoideus generated power is only a function of the energy storage fraction, and decreases linearly as energy storage is increased. (C) The maximum pectoralis generated power rapidly

peaks when the energy storage fraction is high and the energy storage time period is short. (D) The maximum supracoracoideus generated power is only a function of the energy storage fraction, and decreases linearly as energy storage is increased. (E) Pectoralis work loop shape factors (ratio of the observed area to the area of a rectangle with the same range of stress and strain) near the maximum shape factor of 0.73 can be achieved at multiple different energy storage fractions. The maximum shape factor for each energy storage fraction is plotted as a thick black line.

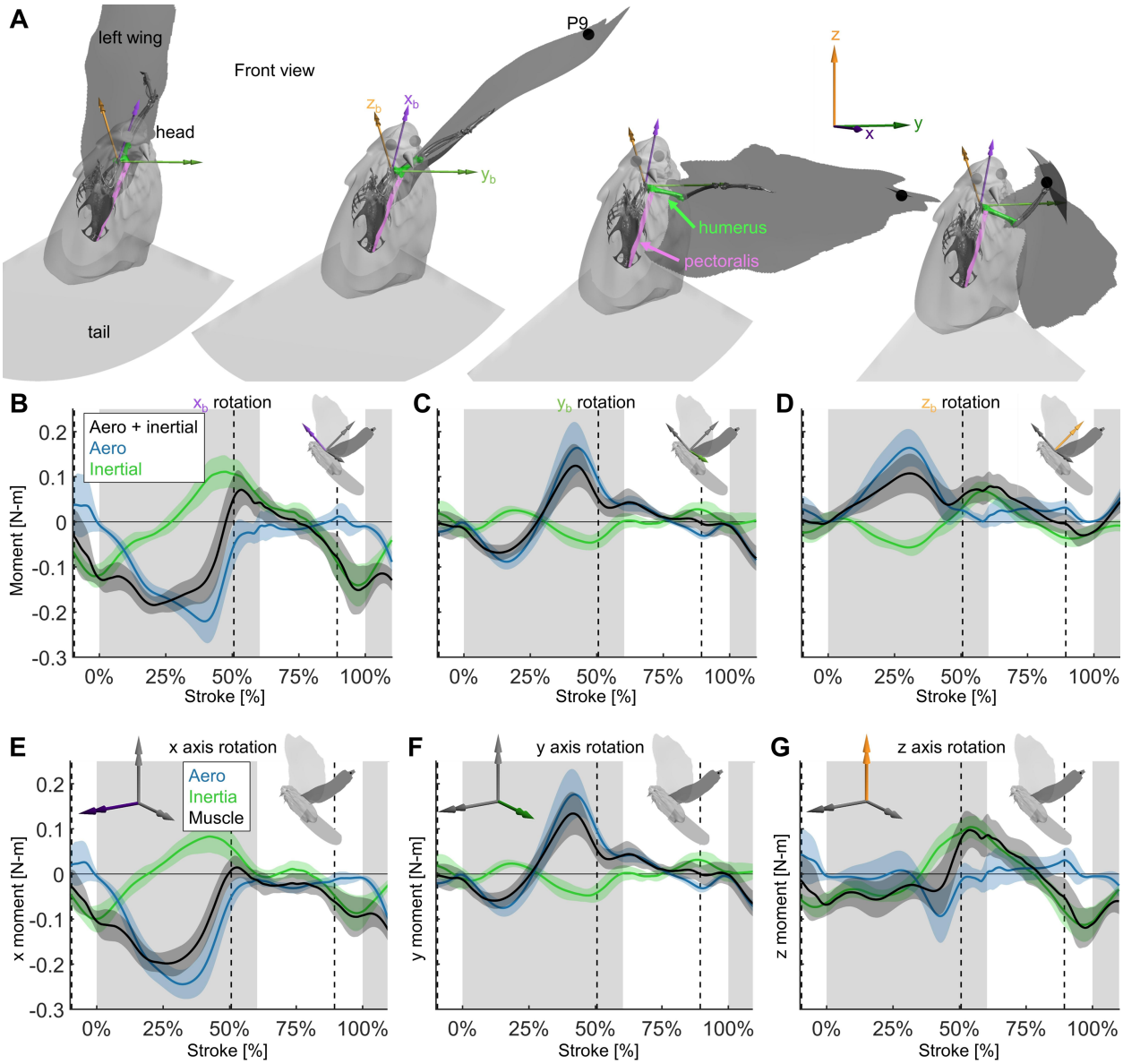

Figure S10. Extra details are added to Fig. 6 to demonstrate how the 3D angular momentum balance works. (A) The frontal view of the dove at 0%, 33%, 67%, and 100% of the downstroke is shown with the

right wing surface removed. The skeleton was positioned based on the shoulder joint and wing kinematics, with only the humerus (green), radius/ulna, and manus permitted to move relative to the body (radius/ulna and manus are used for visualization only). The skeleton was used to define a new 'body' reference frame, where the x_b axis points in the cranial direction (aligned with the thoracic vertebrae of the dove), the y_b axis points in the distal direction (aligned with the y direction in the Newtonian reference frame if the dove flies straight from the takeoff perch to the landing perch), and the z_b axis points in the dorsal direction. For visualization, the pectoralis was modeled as a path along points that are rigidly attached to the skeletal body and humerus. (B-D) Similar to the 1D power balance (Fig. 5), the 3D required muscle moment (black) is composed of the vector sum of the aerodynamic (blue) and inertial (green) 3D moments. (B) The flight muscles need to pull ventrally on the wing (negative moment in the cranial, x_b, axis) during the downstroke, to oppose lift and drag, which point vertically up (Figs. 4A, S5C). During the upstroke, inertial effects dominate, such that the flight muscles pull dorsally during stroke reversal into the beginning of the upstroke, and ventrally at the end of the upstroke. (C) In the lateral (y_b) axis, the required muscle moment is primarily due to aerodynamics rather than inertia. At the beginning of the downstroke, the wing is towards the posterior of the dove, creating a positive y_b aerodynamic torque, which is balanced by a muscle moment to supinate the wing. At the end of the downstroke, the wing is towards the anterior of the dove, so the opposite is true. (D) Because the dorsal (z_b) axis of the dove is partially pointed horizontally backwards, the lift and drag in the positive vertical direction (Fig. S5C), generate a cranial moment during the downstroke. The flight muscles generate a caudal moment during the downstroke to oppose the aerodynamic moment. (E-G) The same 3D angular momentum balance data is shown as in B-D, but in the familiar Newtonian reference frame shown in Fig. 1C. (E) Moments in the x axis. (F) Moments in the y axis. (G) Moments in the z axis.

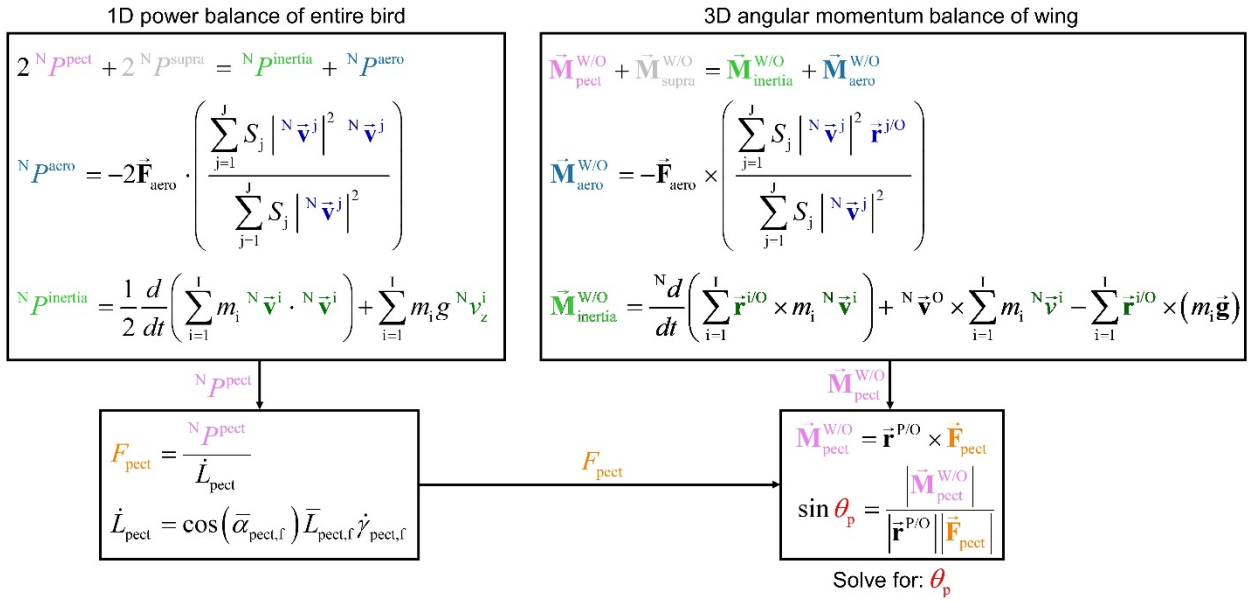

Figure S11. The two overarching dynamics balance methods that we use to analyze muscle behavior resolves different information, yet are related in their form and together provide insight into the pull angle of the pectoralis on the humerus. While the 1D power balance method resolves required muscle power, the 3D angular momentum balance method resolves the 3D direction which the pectoralis pulls on the humerus. However, the two methods are similar in that in each method, the muscle quantity (pink text) equals the sum of the aerodynamic quantity (blue text) plus the inertial quantity (green text). In this flow chart, the equations used in the main text to compute the total muscle power and moments are summarized, and their relationship is visualized, culminating in the computation of the pectoralis pull angle, θ_p (see Fig. 6C). The top left box summarizes the 1D power balance method which results in total muscle power. This can be used to solve for the pectoralis force magnitude, F_{pect}. The top right box summarizes the 3D angular momentum balance which results in total muscle moment. Based on the measured distance between the shoulder joint and the deltopectoral crest ($\vec{\mathbf{r}}^{P/O}$), we can compute the pectoralis pull angle on the humerus.

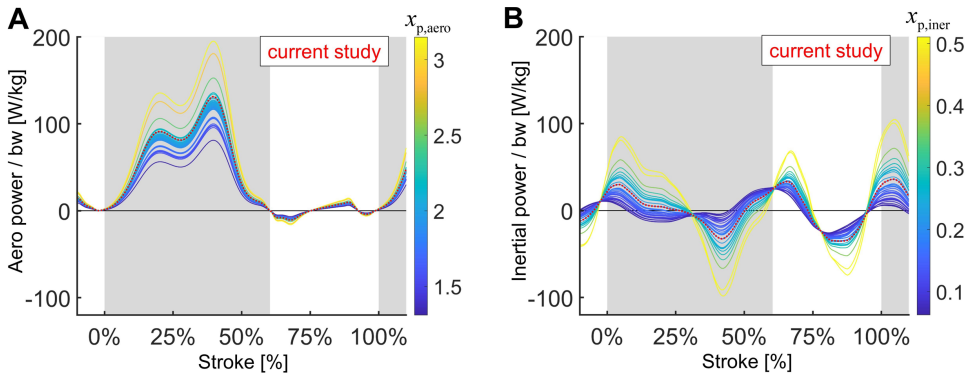

Figure S12. Extra detail is added to Fig. 7 to show that aerodynamic power scaled by bodyweight scales linearly with $x_{p,aero}$, and the inertial power scaled by bodyweight scales linearly with $x_{p,iner}$.

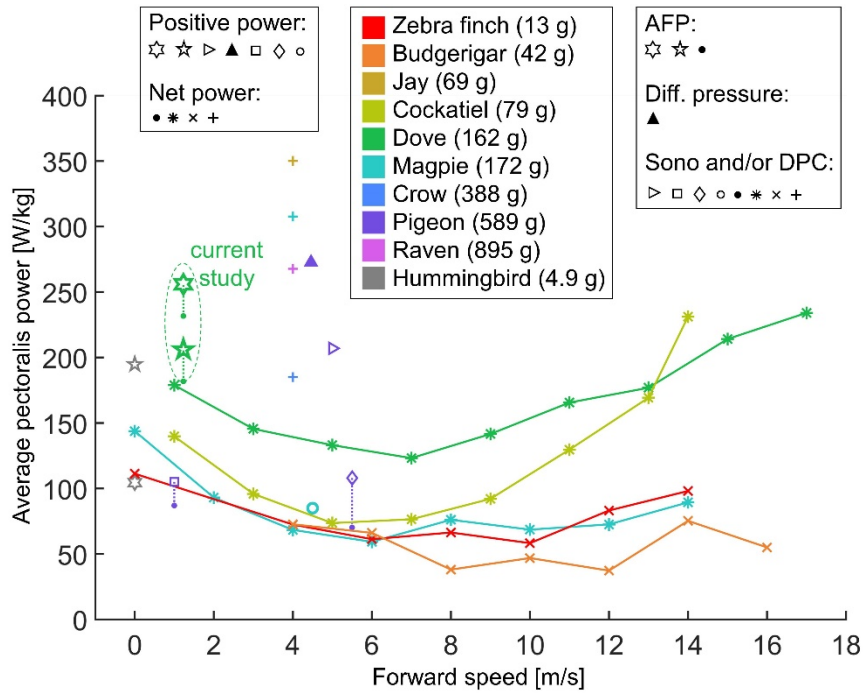

Figure S13. We compare our computed stroke-averaged pectoralis power scaled by pectoralis mass with values measured in literature using a variety of different methods, bird species, and flight speeds during level flight. The data is scattered, and the current study fits within the range of previous measurements. The type of bird corresponds with the color as labeled in the legend and follows rainbow-order from lightest (red) to heaviest (pink). Each study corresponds to a different marker-type, which can be grouped in the following manners: 1) Closed-border shapes (☆, ▷, ▲ , □, ◇, ◦) indicate that the study reported the average positive pectoralis power, while filled-in shapes (•, *, ×, +) indicate that the study

reported the average net pectoralis power. Dotted lines connect studies which reported both net and positive average power, and solid lines connect data from the same study across different flight speeds. 2) Different methods were used to measure pectoralis power. Star shapes (☆, •) indicate that the Aerodynamic Force Platform (AFP) was used to measure aerodynamic forces (includes the current study), which were used in combination with kinematics to compute muscle power. A filled in triangle (▲), indicates that differential pressure sensors on the wings were used to compute muscle power. Other shapes (▷, □, ◇, ◦,•, *, ×, +), indicate that some combination of sonomicrometry (sono) to measure muscle length, and a strain gauge (limited by high-variance calibrations of muscle stress [10]) on the Deltopectoral Crest (DPC) of the humerus was used to measure muscle force. The plotted shapes refer to the following studies:

1) Current study: AFP + kinematics (dove: green): • (net power), ☆ (5-sided-star; positive power; no energy storage), ☆ (6-sided-star; positive power; 100% energy storage).

2) Biewener *et al*. 1998 [9]: Sono + DPC (pigeon: purple): • (net power), ◇(positive power).

3) Tobalske and Biewener 2008 [5]: Sono + DPC (pigeon purple): • (net power), □ (positive power).

4) Dial *et al*. 1997 [11]: Sono + kinematics (magpie: turquoise): o (positive power).

5) Tobalske *et al*. 2003 [3]: Sono + DPC with quasi-steady aerodynamics model for calibration (dove: green, cockatiel: yellow-green, magpie: turquoise): * (net power).

6) Soman *et al*. 2005 [12]: Sono + DPC (pigeon: purple): ▷ (positive power).

7) Usherwood 2005 [40]: Differential pressure sensors on wings (pigeon: purple): ▲ (positive power).

8) Ellerby and Askew 2007 [2]: Sono *in vivo* + muscle force *in vitro* (zebra finch: red, budgerigar: orange): × (net power).

9) Jackson and Dial 2011 [10]: Sono + DPC (jay: gold, magpie: turquoise, crow: blue, raven: pink): + (net power).

10) Ingersoll and Lentink 2018 [13]: AFP + kinematics (Anna's hummingbird: gray): ☆ (net power; no energy storage), ☆ (6-sided-star; net power; perfect energy storage).

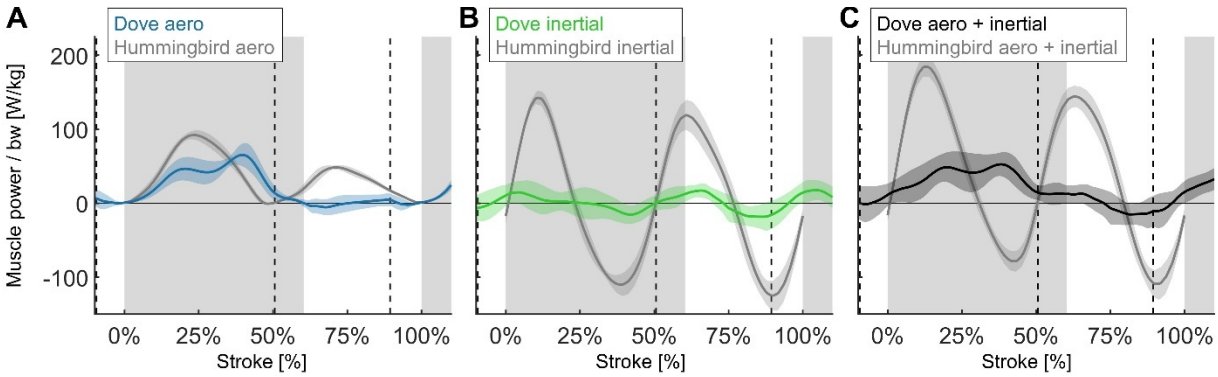

Figure S14. By comparing our computed time-resolved power for doves (Fig. 4B) to hummingbirds (also computed using the Aerodynamic Force Platform in Ingersoll and Lentink 2018 [13]), we find that the aerodynamic power during downstroke is similar, while the aerodynamic power during upstroke and the inertial power are very different. (*N* = 6 Anna's hummingbirds, *n* = 5 wingbeats each, flapping frequency = 41 Hz, *N* = 4 doves, *n* = 5 flights each, flapping frequency = 9.8 Hz; second stroke after takeoff for doves and hovering flight for hummingbirds; gray region indicates downstroke for doves; power scaled by bodyweight: bw; vertical dashed lines indicate pectoralis strain rate equals zero for doves). (A) The aerodynamic power scaled by bodyweight is similar during upstroke and downstroke for hummingbirds (gray), whereas for doves (blue), the primary aerodynamic power is during downstroke. (B) The magnitude of the inertial power scaled by bodyweight is significantly larger for hummingbirds (gray) than for doves (green). (C) The required muscle power (aerodynamic + inertial power) scaled by bodyweight is larger for hummingbirds (gray) during the majority of the stroke than for doves (black).

Supplementary Tables

Table S1. Air conditions across all 20 flights. (*N* = 4 doves; *n* = 5 flights each).

Variable	Mean ± s.d.
Air density [kg·m^{-3}]	1.191 ± 0.001
Air temperature [°C]	23.73 ± 0.28
Air pressure [kPa]	101.78 ± 0.06
Air relative humidity [%]	27.05 ± 6.75

Table S2. Measured aerodynamic and leg impulses before surgery, after surgery, and after surgery with the suspended recording cable (for recording EMG & sonomicrometry). So that horizontal and vertical impulses can be compared, gravity has been subtracted from the vertical impulse, so that while at rest, the vertical impulse is zero (horizontal and vertical impulse scaled by bodyweight, bw and integration time; bodyweight is based on the average vertical force on the takeoff perch before takeoff). These definitions for impulse match Chin and Lentink's 2017 paper on directional impulse of birds [29].

Variable	Before surgery	After surgery (no cable)	After surgery (with cable)
Total bodyweight measured by takeoff perch [g]	158.4 ± 0.8	159.1 ± 3.6	170.0 ± 1.1
Vertical takeoff impulse (perch) [-]	0.39 ± 0.03	0.34 ± 0.03	0.29 ± 0.05
Vertical aerodynamic impulse (all strokes) [-]	-0.22 ± 0.02	-0.28 ± 0.04	-0.23 ± 0.06
Vertical landing impulse (perch) [-]	0.09 ± 0.07	0.12 ± 0.15	-0.09 ± 0.13
Vertical total impulse [-]	0.03 ± 0.01	0.03 ± 0.03	0.01 ± 0.01
Vertical aerodynamic impulse (stroke 2) [-]	0.06 ± 0.04	-0.22 ± 0.03	-0.17 ± 0.06
Horizontal takeoff impulse (perch) [-]	0.81 ± 0.03	0.56 ± 0.05	0.64 ± 0.03
Horizontal aerodynamic impulse (all strokes) [-]	-0.09 ± 0.02	-0.03 ± 0.01	0.02 ± 0.03
Horizontal landing impulse (perch) [-]	-0.35 ± 0.04	-0.43 ± 0.14	-0.42 ± 0.19
Horizontal total impulse [-]	0.03 ± 0.03	0.01 ± 0.01	0.08 ± 0.01
Horizontal aerodynamic impulse (stroke 2) [-]	-0.11 ± 0.05	0.08 ± 0.04	0.15 ± 0.02

Table S3. Measured aerodynamic and leg impulses among individual doves. The definition for impulse matches Table S2.

Variable	Dove 1	Dove 2	Dove 3	Dove 4	All doves

Total bodyweight measured by takeoff perch [g]	152.6 ± 0.9	166.7 ± 3.4	170.0 ± 1.1	182.3 ± 1.7	167.9 ± 11.0
Vertical takeoff impulse (perch) [-]	0.34 ± 0.04	0.26 ± 0.11	0.29 ± 0.05	0.23 ± 0.06	0.28 ± 0.08
Vertical aerodynamic impulse (all strokes) [-]	-0.19 ± 0.03	-0.26 ± 0.09	-0.23 ± 0.06	-0.18 ± 0.06	-0.22 ± 0.07
Vertical landing impulse (perch) [-]	-0.09 ± 0.05	-0.25 ± 0.16	-0.09 ± 0.13	-0.16± 0.11	-0.15 ± 0.13
Vertical total impulse [-]	0.00 ± 0.01	-0.01 ± 0.02	0.01 ± 0.01	0.02 ± 0.01	0.01 ± 0.02
Vertical aerodynamic impulse (stroke 2) [-]	-0.05 ± 0.05	-0.21 ± 0.09	-0.17 ± 0.06	-0.13 ± 0.06	-0.14 ± 0.09
Horizontal takeoff impulse (perch) [-]	0.77 ± 0.06	0.69 ± 0.03	0.64 ± 0.03	0.44 ± 0.04	0.63 ± 0.13
Horizontal aerodynamic impulse (all strokes) [-]	-0.09 ± 0.02	-0.01 ± 0.02	0.02 ± 0.03	0.05 ± 0.02	-0.01 ± 0.06
Horizontal landing impulse (perch) [-]	-0.29 ± 0.02	-0.12 ± 0.13	-0.42 ± 0.19	-0.34 ± 0.14	-0.29 ± 0.16
Horizontal total impulse [-]	0.08 ± 0.03	0.10 ± 0.01	0.08 ± 0.01	0.08 ± 0.01	0.08 ± 0.02
Horizontal aerodynamic impulse (stroke 2) [-]	-0.09 ± 0.01	-0.03 ± 0.09	0.15 ± 0.02	0.17 ± 0.03	0.05 ± 0.13

Table S4. Measured aerodynamic forces for the second stroke after takeoff (Fig. 3). The weight of the dove is primarily supported during the downstroke. Drag partially contributes to weight support, while opposing forward aerodynamic force. The reported values are the stroke-averaged aerodynamic force measured by the Aerodynamic Force Platform (AFP), normalized by bodyweight. We compute the time-

resolved lift and drag using the measured horizontal and vertical aerodynamic forces together with the measured wing velocity. (*N* = 4 doves; *n* = 5 flights each; mean ± standard deviation).

Stroke-averaged aerodynamic force / bodyweight [%]	Entire stroke	Downstroke	Upstroke	Lift	Drag
Weight support (vertical force)	87.28 ± 9.94	76.00 ± 7.60	11.28 ± 2.81	66.17 ± 10.81	21.11 ± 4.62
Horizontal force	5.21 ± 12.60	2.52 ± 11.74	2.68 ± 1.49	32.84 ± 9.96	-27.64 ± 4.64

Table S5. We compute aerodynamic, inertial, and required muscle power based on first principals (Fig. 4), and model the effect of the amount of energy storage in the supracoracoideus (Fig. 5). The primary component of stroke-averaged net muscle power is aerodynamic, whereas the positive and negative regions of inertial power cancel. Our energy storage model predicts that the pectoralis would need to generate 24.9% ± 17.5% more power to fully power the upstroke via energy storage in the supracoracoideus. (*N* = 4 doves; *n* = 5 flights each; mean ± standard deviation).

Stroke-averaged power / pectoralis mass [W/kg]	Aerodynamic	Inertial	Muscle	Pectoralis: no energy storage	Pectoralis: 100% energy storage
Net power	210.0 ± 56.9	-1.4 ± 20.0	207.6 ± 56.6	181.8 ± 47.6	231.7 ± 59.6
Positive power	222.4 ± 51.5	80.0 ± 21.9	249.3 ± 59.8	206.0 ± 49.6	255.9 ± 62.7
Negative power	-13.5 ± 10.3	-81.4 ± 22.8	-41.7 ± 22.2	-24.2 ± 15.3	-24.2 ± 15.3
Max power	775.3 ± 179.0	348.0 ± 112.5	711.3 ± 150.7	734.5 ± 165.5	varies

Table S6. Scaling analysis (Fig. 7) parameter summary.

Variable	Scaling equation	Description	Method for acquiring
m_{body}		Body mass	Measured extant bird data from literature (31 birds)

m_{pect}		Pectoralis mass (single pectoralis)	Measured extant bird data from literature scaled isometrically to match body mass (exact match: 25 birds, close relative: 6 birds)
m_{wing}		Wing mass (single wing)	Measured extant bird data from literature (31 birds)
I_{wing}		Wing moment of inertia (single wing)	Measured extant bird data from literature (27 birds) or determined based on scaling law reported in literature: Berg & Rayner 1995 [46] (close relative: 4 birds)
$\lvert\vec{\mathbf{r}}_{\text{span}}\rvert$		Wingspan (distance from shoulder joint to wingtip; single wing)	Measured extant bird data from literature (27 birds) or measured extant bird data from literature scaled isometrically to match body mass (close relative: 4 birds)
$\lvert\vec{\mathbf{r}}_{\text{wing,cg}}\rvert$		Distance from shoulder joint to center of gravity of wing (single wing)	Measured extant bird data from literature (27 birds) or determined isometrically to match body mass (close relative: 4 birds)
S_{wing}		Wing area (single wing)	Measured extant bird data from literature (27 birds) or measured extant bird data from literature scaled isometrically to match body mass (close relative: 4 birds)

f		Wingbeat frequency	Measured extant bird data from literature (21 birds) or determined based on scaling law reported in literature: Berg & Rayner 1995 [46] (10 birds)
$m_{\text{wing,i}}$		Wing mass distribution (point masses)	Least-squares fit to match wing mass, inertia, and center of gravity data
Δt	$\propto f^{-1}$	Time step	Assumed to scale isometrically
$\vec{\mathbf{F}}_{\text{aero}}$	$\propto m_{\text{body}}$	Aerodynamic force	Assumed to scale isometrically
${}^{\text{N}}\vec{\mathbf{v}}^{\text{i}}_{\text{wing}}$	$\propto f\left\lvert\vec{\mathbf{r}}_{\text{span}}\right\rvert$	Wing velocity (distributed)	Assumed to scale isometrically
${}^{\text{N}}\vec{\mathbf{v}}_{\text{body}}$	$\propto 1$	Body velocity	Unchanged
$x_{\text{p,aero}}$	$=\left\lvert\vec{r}_{span}\right\rvert f$	Scaling parameter which dictates the aerodynamic power contribution ∝ wingtip speed	Derived (Eqn. S71)
$x_{\text{m,aero}}$	$=\left\lvert\vec{r}_{span}\right\rvert$	Scaling parameter which dictates the aerodynamic moment contribution = wingspan	Derived (Eqn. S72)
$x_{\text{p,iner}}$	$=\frac{I_{\text{wing}}}{m_{\text{body}}} f^3$ $=\frac{m_{\text{wing}}}{m_{\text{body}}}\left(\frac{r_{\text{gyr}}}{\left\lvert\vec{\mathbf{r}}_{\text{span}}\right\rvert}\right)^2\left(f\left\lvert\vec{\mathbf{r}}_{\text{span}}\right\rvert\right)^2 f$	Scaling parameter which dictates the inertial power contribution ∝ (wing mass %) (wing radius of gyration %)^2 (wingtip speed)^2 (wingbeat frequency)	Derived (Eqn. S73)

$x_{\mathrm{m,iner}}$	$= \frac{I_{\mathrm{wing}}}{m_{\mathrm{body}}} f^2$ $= \frac{m_{\mathrm{wing}}}{m_{\mathrm{body}}} \left(\frac{r_{\mathrm{gyr}}}{\lvert \vec{\mathbf{r}}_{\mathrm{span}} \rvert} \right)^2 \left(f \lvert \vec{\mathbf{r}}_{\mathrm{span}} \rvert \right)^2$	Scaling parameter which dictates the inertial moment contribution ∝ (wing mass %) (wing radius of gyration %)^2 (wingtip speed)^2	Derived (Eqn. S74)

Table S7. Scaling analysis parameters used for analyzing shifts in the timing of the pectoralis power distribution during the stoke (Fig. 7D).

Variable	Scaling equation	Description	Method for acquiring
m_{body}		Body mass	Measured extant bird data from literature (17 birds)
m_{wing}		Wing mass (single wing)	Measured extant bird data from literature (1 birds) or measured extant bird data from literature scaled isometrically to match body mass (16 birds)
$\lvert \vec{\mathbf{r}}_{\mathrm{span}} \rvert$		Wingspan (distance from shoulder joint to wingtip; single wing)	Measured extant bird data from literature (3 birds) or measured extant bird data from literature scaled isometrically to match body mass (14 birds)
f		Wingbeat frequency	Measured extant bird data from literature (17 birds)
$\mathrm{EMG}_{\mathrm{start}}$		Start of electrical activation of pectoralis (stroke %)	Measured extant bird data from literature (17 birds)
$\mathrm{EMG}_{\mathrm{end}}$		End of electrical activation of pectoralis (stroke %)	Measured extant bird data from literature (17 birds)

$F_{pect,max}$		Max force generated by pectoralis (stroke %)	Measured extant bird data from literature (12 birds)
I_{wing}		Wing moment of inertia (single wing)	Determined based on scaling law reported in literature: Berg & Rayner 1995 [46] (17 birds)
$x_{p,iner} / x_{p,aero}$	$= x_{m,iner} / x_{m,aero}$ $= \frac{I_{wing}}{m_{body} \lvert \vec{r}_{span} \rvert} f^2$ $= \frac{m_{wing}}{m_{body}} \left(\frac{r_{gyr}}{\lvert \vec{\mathbf{r}}_{span} \rvert} \right)^2 \left(f \lvert \vec{\mathbf{r}}_{span} \rvert \right) f$	Scaling parameter which dictates the aerodynamic power contribution ∝ wingtip speed	Derived

Table S8. Detailed breakdown of data from extant birds used for the scaling analysis (Fig. 7). Some data was scaled isometrically by bodyweight based on matching the species of the bird (blue). Other data was found based on published scaling relationships (green). The references corresponding to the letter plus number keys (found in columns titled Src) are in Table S10. To match some of the bird species, a close relative was used when data was missing for the original species: Close relative of Parus ater used was Parus cristatus mitratus. Close relative of Perisoreus canadensis used was Xanthoura yncas. Close relative of Pica hudsonia used was Pica pica. Close relative of Corvus brachyrhynchos used was Corvus vorone. Close relative of Alectoris rufa used was Coturnix. Close relative of Corvus corax used was Corvus vornix.

Bird		Body mass [g]		Single pectoralis mass [g]		Single wing mass [g]		Wingspan: shoulder joint to wingtip [mm]		Center of gravity dist. to shoulder joint [mm]		Single wing moment of inertia [10^6·kg·m^2]		Wing area [cm^2]		Wingbeat frequency [Hz]	
Scientific name	Common name	#	Src	#	Src	#	Src	#	Src	#	Src	#	Src	#	Src	#	Src
Parus caeruleus	Blue tit	9.5	B95	0.764	G62	0.48	B95	95	B95	18	B95	0.286	B95	42.4	B95	21.7	B95
Poephila guttata	Zebra finch	14.5	B95	0.98	T05	0.63	B95	90	B95	19	B95	0.356	B95	33	B95	27.4	B95
Parus ater	Coal tit	14.6	B95	1.016	G62	0.84	B95	112	B95	21	B95	0.673	B95	51.9	B95	18.2	B95
Erithacus rubecula	Robin	15	B95	0.904	G62	0.69	B95	108	B95	22	B95	0.581	B95	46.5	B95	16.1	B95
Delichon urbica	House martin	15.2	B95	1.006	G62	0.85	B95	140	B95	30	B95	1.348	B95	51.5	B95	9.4	B95
Fringilla coelebs	Chaffinch	19.9	B95	2.33	G62	1.1	B95	116	B95	23	B95	1.007	B95	55.8	B95	17.3	B95
Alcedo atthis	Common kingfisher	34.3	B95	2.836	G62	1.55	B95	130	B95	30	B95	2.344	B95	62	B95	15.6	B95

Bird		Body mass [g]		Single pectoralis mass [g]		Single wing mass [g]		Wingspan: shoulder joint to wingtip [mm]		Center of gravity dist. to shoulder joint [mm]		Single wing moment of inertia [$10^6 \cdot kg \cdot m^2$]		Wing area [cm^2]		Wingbeat frequency [Hz]	
Scientific name	Common name	#	Src	#	Src	#	Src	#	Src	#	Src	#	Src	#	Src	#	Src
Turdus merula	Blackbird	56.2	B95	4.48	G62	3.14	B95	184	B95	42	B95	9.115	B95	127.8	B95	8.6	B95
Sturnus vulgaris	Starling	58.1	B95	5.48	G62	3.7	B95	185	B95	41	B95	10.16	B95	120.8	B95	11.3	B95
Picoides major	Great spotted woodpecker	62.9	B95	5.6	G62	4.17	B95	190	B95	42	B95	11.15	B95	121.8	B95	10.4	B95
Turdus philomelos	Song thrush	67.6	B95	6.73	G62	3.39	B95	171	B95	33	B95	6.098	B95	103.5	B95	10.0	B95
Perisoreus canadensis	Gray jay	68.9	J11A	4.5	G62	4.48	G62	172	G62	36	B95	10.89	B95	154	G62	11.6	J11A
Alle alle	Dovekie (little auk)	100	B95	7.02	G62	5.04	B95	183	B95	46	B95	16.18	B95	65	B95	9.4	B95
Coturnix coturnix	Quail	132	B95	11.7	G62	4	B95	164	B95	37	B95	8.482	B95	91.8	B95	17.8	B95
Podiceps ruficollis	Little grebe	146	B95	5.94	G62	4.56	B95	194	B95	53	B95	20.03	B95	110.1	B95	10.2	B95
Streptopelia risoria	White Ringneck dove	161.6	CURR	14.66	CURR	8.62	CURR	217	CURR	52	CURR	35.3	CURR	182.6	CURR	9.8	CURR

Bird		Body mass [g]		Single pectoralis mass [g]		Single wing mass [g]		Wingspan: shoulder joint to wingtip [mm]		Center of gravity dist. to shoulder joint [mm]		Single wing moment of inertia [$10^6 \cdot kg \cdot m^2$]		Wing area [cm^2]		Wingbeat frequency [Hz]	
Scientific name	Common name	#	Src	#	Src	#	Src	#	Src	#	Src	#	Src	#	Src	#	Src
Scolopax rusticola	Woodcock	163	B95	20.75	G62	12.45	B95	279	B95	68	B95	84.98	B95	254.2	B95	6.9	B95
Pica hudsonia	Black-billed magpie	172.4	J11A	11	G62	12.6	G62	218	G62	46	B95	52.67	B95	277	G62	9.0	J11A
Picus viridis	Green woodpecker	179	B95	14.57	G62	11.75	B95	235	B95	51	B95	47.54	B95	231	B95	8.3	B95
Larus ridibundus	Black-headed gull	256	B95	16.33	G62	18.98	B95	461	B95	118	B95	402.5	B95	442.2	B95	3.5	B95
Accipiter nisus	Eurasian sparrowhawk	279	B95	28.47	G62	22.61	B95	355	B95	93	B95	263	B95	377	B95	4.5	B95
Columba livia	Rock dove (pigeon)	293	B95	27.63	T08	22.47	B95	323	B95	71	B95	172.7	B95	314	B95	6.7	B95
Corvus frugilegus	Rook	328	B95	24.15	G62	28.78	B95	389	B95	80	B95	326.9	B95	419.8	B95	4.0	B95
Gallinula chloropus	Grey moorhen	364	B95	22.66	G62	14.2	B95	271	B95	65	B95	95.58	B95	254.9	B95	7.2	B95
Corvus brachyrhynchos	American crow	387.6	J11A	27.6	G62	30.8	G62	302	G62	63	B95	261.3	B95	465	G62	6.4	J11A

Bird		Body mass [g]		Single pectoralis mass [g]		Single wing mass [g]		Wingspan: shoulder joint to wingtip [mm]		Center of gravity dist. to shoulder joint [mm]		Single wing moment of inertia [$10^6 \cdot kg \cdot m^2$]		Wing area [cm^2]		Wingbeat frequency [Hz]	
Scientific name	Common name	#	Src	#	Src	#	Src	#	Src	#	Src	#	Src	#	Src	#	Src
Alectoris rufa	Red-legged partridge	393	B95	39.3	G62	19.15	B95	254	B95	60	B95	100.7	B95	241.1	B95	7.7	B95
Strix aluco	Tawny owl	398	B95	18.81	G62	31.41	B95	421	B95	111	B95	578.5	B95	617.7	B95	4.5	B95
Melanitta nigra	Common scoter	569	B95	33.36	G62	38.85	B95	390	B95	108	B95	656.6	B95	422.6	B95	4.9	B95
Uria aalge	Common murre (guillemot)	691	B95	50.63	G62	31.07	B95	335	B95	100	B95	424.8	B95	241.6	B95	9.4	B95
Buteo buteo	Common buzzard	771	B95	42.6	G62	72.51	B95	590	B95	155	B95	2536	B95	1142	B95	3.2	B95
Corvus corax	Common raven	894.9	J11A	65.6	G62	67.9	G62	342	G62	72	B95	773.6	B95	829	G62	5.6	J11A
Ardea cinerea	Grey heron	2140	B95	164.9	G62	167.1	B95	830	B95	216	B95	12334	B95	1997	B95	2.6	B95

Table S9. Detailed breakdown of data from extant birds used for analyzing shifts in the timing of the pectoralis power distribution during the stoke for the scaling analysis (Fig. 7D). The same color scheme is used as in Table S8, and the close relative species used when data was missing for the original species are: Close relative of Selasphorus rufus used was Calypte anna. Close relative of Perisoreus canadensis used was

Xanthoura yncas. Close relative of Pica hudsonia used was Pica pica. Close relative of Corvus brachyrhynchos used was Corvus corone. Close relative of Alectoris chukar used was Caccabis rufa. Close relative of Corvus corax used was Corvus cornix.

Bird		Flight mode	Body mass [g]		Single wing mass [g]		Wingspan: shoulder joint to wingtip [mm]		Single wing moment of inertia [10^6·kg·m^2]		Wingbeat frequency [Hz]		Pectoralis EMG start & end time [stroke %]			Max pectoralis force time [stroke %]	
Scientific name	Common name		#	Src	#	Src	#	Src	#	Src	#	Src	Start	End	Src	#	Src
Selasphorus rufus	Rufous Hummingbird	0-10 m/s	3.4	T10	0.084	I18	45.5	I18	0.0110	B95	42	T10	-29.3	-8.8	T10		
Calypte anna	Anna's hummingbird	Hovering	4.2	D13	0.104	I18	48.8	I18	0.0159	B95	40	D13	-22.9	-14.2	D13		
Calypte anna	Anna's hummingbird	Hovering	4.9	I18	0.121	I18	51.4	I18	0.0225	I18	41	I18	-25.4	-16.0	A10	4.2	A10
Taeniopygia guttata	Zebra finch		11.1	D13	0.48	B95	82.3	B95	0.231	B95	27.1	D13	-16.5	3.0	D13		
Taeniopygia guttata	Zebra finch	Ave: ascend, 0, 2, 4 m/s	13.3	T05	0.58	B95	72	T05	0.213	B95	27	T05	-14.5	27.7	T05		
Perisoreus canadensis	Gray jay	Takeoff	68.9	J11A	4.48	G62	172	G62	10.89	B95	11.6	J11A	-9.7	30.8	J11A	30.5	J11A
Sturnus vulgaris	Starling	13.7 m/s	71.7	B92	4.55	B95	198	B95	14.97	B95	15	B92	-19.4	20.9	B92	28.4	B92
Nymphicus hollandicus	Cockatiel	7 m/s	85	H03	8.1	H04	232	H04	37.72	B95	7.64	H03	-27.9	17.1	H03	13.0	H03

Bird		Flight mode	Body mass [g]		Single wing mass [g]		Wingspan: shoulder joint to wingtip [mm]		Single wing moment of inertia [10^6·kg·m^2]		Wingbeat frequency [Hz]		Pectoralis EMG start & end time [stroke %]			Max pectoralis force time [stroke %]	
Scientific name	Common name		#	Src	#	Src	#	Src	#	Src	#	Src	Start	End	Src	#	Src
Pica hudsonia	Black-billed magpie	Takeoff	172.4	J11A	12.6	G62	218	G62	52.67	B95	9	J11A	-9.4	28.2	J11A	14.0	J11A
Pica pica	Magpie	6 m/s	174	D97	12.7	G62	219	G62	53.45	B95	8.5	D97	-35.3	9.3	D97	15.8	D97
Columba livia	Pigeon	Takeoff	309	D93	23.6	B95	329	B95	237.1	B95	9	D93	-28.1	27.2	D93	16.5	D93
Corvus brachyrhynchos	American crow	Takeoff	387.6	J11A	30.8	G62	302	G62	261.3	B95	6.4	J11A	-2.7	39.7	J11A	27.4	J11A
Columba livia	Pigeon	Level flight	441.4	J11B	33.8	B95	370	B95	441.1	B95	8.9	J11B	-17.4	26.7	J11B	26.9	J11B
Columba livia	Pigeon	Ascending flight	452	J11B	34.6	B95	373	B95	459.4	B95	8.9	J11B	-18.9	26.1	J11B	26.5	J11B
Alectoris chukar	Chukar	Adult flight	549	T17	23.9	G62	172	G62	62.72	B95	22	T17	-12.8	14.5	T17		
Columba livia	Pigeon	0-2 m/s	562	T08	43	B95	330	T08	445.9	B95	8.6	T08	-11.8	30.0	T08	24.3	T08
Corvus corax	Common raven	Takeoff	894.9	J11A	67.9	G62	342	G62	773.6	B95	5.6	J11A	-6.1	46.0	J11A	48.2	J11A

Table S10. Keys for references in Tables S8 and S9.

Abbrev	Full source
CURR	Current work
A10	[54]
B95	[46]
B92	[8]
D93	[14]
D97	[11]
D13	[55]
G62	[53]
H03	[15]
H04	[56]
I18	[13]
J11A	[10]
J11B	[57]
T05	[44]
T08	[5]
T10	[58]
T17	[59]

Acknowledgements

We thank Wren Cooperrider for his help acquiring data for this study, and Paul Mitiguy for his consultation during algorithm development related to dynamics. This work was supported by an NSF Faculty Early Career Development (CAREER) Award 1552419 to DL and motivated by NSF reviewer feedback. Additional support to study wing morphing came from AFOSR BRI award number FA9550-16-1-0182 with special thanks to B. L. Lee for leading the program. BWT was funded by the National Science Foundation grant NSF EFRI 1935216, MED was supported by a Stanford University Graduate Fellowship and DDC was supported by a Stanford Graduate Fellowship and a National Defense Science and Engineering Graduate Fellowship.

Additional information

Competing interests

David Lentink: Reviewing editor, eLife. The other authors declare that no competing interests exist.

Funding

This research was supported by the National Science Foundation (NSF) Graduate Research Fellowship under grant no. DGE-114747 to M.E.D., the Air Force Office of Scientific Research (AFOSR) under grant no. FA9550-16-1-0182, and NSF CAREER Award 1552419 to D.L., Stanford Graduate Fellowship to M.E.D. and D.D.C., National Defense Science and Engineering Graduate Fellowship to D.D.C., and NSF IOS-1838688 to B.W.T.

Author contributions

Marc E. Deetjen: Conceptualization, Resources, Data curation, Software, Formal analysis, Validation, Investigation, Visualization, Methodology, Writing—original draft, Project administration, Writing—review and editing. MED contributed to collecting and analyzing data from the dove experiments, interpreting the findings, developing all new mathematical models and derivations, and drafting the manuscript.

Diana D. Chin: Resources, Data curation, Software, Validation, Methodology, Writing—review and editing. DDC contributed to collecting and analyzing data from the dove experiments.

Ashley M. Heers: Resources, Software, Validation, Writing—review and editing. AMH contributed to developing the musculoskeletal model.

Bret W. Tobalske: Conceptualization, Resources, Data curation, Validation, Investigation, Methodology, Writing—review and editing. BWT contributed to collecting and analyzing data from the dove experiments, conducting the surgical procedure, and editing the manuscript.

David Lentink: Conceptualization, Resources, Data curation, Investigation, Supervision, Funding acquisition, Methodology, Project administration, Writing—review and editing. DL contributed to collecting and analyzing data from the dove experiments, interpreting the findings, and editing the manuscript. DL also oversaw the project.

Author ORCIDs

Marc E. Deetjen: https://orcid.org/0000-0002-6947-6408

Diana D. Chin: https://orcid.org/0000-0002-3015-7645

Ashley M. Heers: https://orcid.org/0000-0002-7635-0651

Bret W. Tobalske: https://orcid.org/0000-0002-5739-6099

David Lentink: https://orcid.org/0000-0003-4717-6815

Data availability

Raw data, processed data, and software are available from the Dryad Digital Repository: #### (will deposit data when manuscript is accepted for full review)

References

[1] D. L. Altshuler and R. Dudley, "Kinematics of hovering hummingbird flight along simulated and natural elevational gradients," *Journal of Experimental Biology*, vol. 206, no. 18, pp. 3139–3147, 2003, doi: 10.1242/jeb.00540.

[2] D. J. Ellerby and G. N. Askew, "Modulation of flight muscle power output in budgerigars Melopsittacus undulatus and zebra finches Taeniopygia guttata: in vitro muscle performance," *Journal of Experimental Biology*, vol. 210, no. 21, pp. 3780–3788, 2007, doi: 10.1242/jeb.006288.

[3] B. W. Tobalske, T. L. Hedrick, K. P. Dial, and A. A. Biewener, "Comparative power curves in bird flight," *Nature*, vol. 421, no. 23, pp. 363–366, 2003, doi: 10.1038/nature01367.1.

[4] A. M. Heers, D. B. Baier, B. E. Jackson, and K. P. Dial, "Flapping before flight: High resolution, three-dimensional skeletal kinematics of wings and legs during avian development," *PLoS One*, vol. 11, no. 4, pp. 1–24, 2016, doi: 10.1371/journal.pone.0153446.

[5] B. W. Tobalske and A. A. Biewener, "Contractile properties of the pigeon supracoracoideus during different modes of flight," *Journal of Experimental Biology*, vol. 211, no. 2, pp. 170–179, 2008, doi: 10.1242/jeb.007476.

[6] K. Liem, W. Bemis, W. F. Walker, and L. Grande, *Functional Anatomy of the Vertebrates: An Evolutionary Perspective*. Harcourt College Publishers, 2001.

[7] G. De Luliis and D. Pulera, *The Dissection of Vertebrates*. Academic Press, 2019.

[8] A. A. Biewener, K. P. Dial, and G. E. Goslow Jr., "Pectoralis Muscle Force and Power Output During Flight in the Starling," *Journal of Experimental Biology*, vol. 164, no. 1, pp. 1–18, 1992.

[9] A. A. Biewener, W. R. Corning, and B. W. Tobalske, "In vivo pectoralis muscle force-length behavior during level flight in pigeons (Columba livia)," *J Exp Biol*, vol. 201, pp. 3293–3307, 1998.

[10] B. E. Jackson and K. P. Dial, “Scaling of mechanical power output during burst escape flight in the Corvidae,” *Journal of Experimental Biology*, vol. 214, no. 3, pp. 452–461, 2011, doi: 10.1242/jeb.046789.

[11] K. P. Dial, A. A. Biewener, B. W. Tobalske, and D. R. Warrick, “Mechanical power output of bird flight,” *Nature*, vol. 390, no. 6655, pp. 67–70, 1997, doi: 10.1038/36330.

[12] A. Soman, T. L. Hedrick, and A. A. Biewener, “Regional patterns of pectoralis fascicle strain in the pigeon Columba livia during level flight,” *J Exp Biol*, vol. 208, no. 4, pp. 771–786, 2005, doi: 10.1242/jeb.01432.

[13] R. Ingersoll and D. Lentink, “How the hummingbird wingbeat is tuned for efficient hovering,” *J Exp Biol*, vol. 221, 2018, doi: 10.1242/jeb.178228.

[14] K. P. Dial and A. A. Biewener, “Pectoralis Muscle Force and Power Output During Different Modes of Flight in Pigeons,” *J Exp Biol*, vol. 176, pp. 31–54, 1993.

[15] T. L. Hedrick, B. W. Tobalske, and A. A. Biewener, “How cockatiels (Nymphicus hollandicus) modulate pectoralis power output across flight speeds,” *J Exp Biol*, vol. 206, no. 8, pp. 1363–1378, 2003, doi: 10.1242/jeb.00272.

[16] G. N. Askew and R. L. Marsh, “The mechanical power output of the pectoralis muscle of blue-breasted quail (Coturnix chinensis): The in vivo length cycle and its implications for muscle performance,” *Journal of Experimental Biology*, vol. 204, no. 21, pp. 3587–3600, 2001.

[17] P. J. Reiser, K. C. Welch, R. K. Suarez, and D. L. Altshuler, “Very low force-generating ability and unusually high temperature dependency in hummingbird flight muscle fibers,” *Journal of Experimental Biology*, vol. 216, no. 12, pp. 2247–2256, 2013, doi: 10.1242/jeb.068825.

[18] A. A. Biewener, “Muscle function in avian flight: Achieving power and control,” *Philosophical Transactions of the Royal Society B: Biological Sciences*, vol. 366, no. 1570, pp. 1496–1506, 2011, doi: 10.1098/rstb.2010.0353.

[19] A. A. Biewener and R. V. Baudinette, “In vivo muscle force and elastic energy storage during steady-speed hopping of tammar wallabies (Macropus eugenii),” *Journal of Experimental Biology*, vol. 198, pp. 1829–1841, 1995.

[20] T. J. Roberts, R. L. Marsh, P. G. Weyand, and C. R. Taylor, “Muscular force in running turkeys: The economy of minimizing work,” *Science (1979)*, vol. 275, no. 5303, pp. 1113–1115, 1997, doi: 10.1126/science.275.5303.1113.

[21] A. A. Biewener, “Muscle function in vivo: A comparison of muscles used for elastic energy savings versus muscles used to generate mechanical power,” *Am Zool*, vol. 38, no. 4, pp. 703–717, 1998, doi: 10.1093/icb/38.4.703.

[22] A. A. Biewener and T. J. Roberts, “Muscle and tendon contributions to force, work, and elastic energy savings: a comparative perspective,” *Excersice and sport sciences reviews*, vol. 28, no. 3, pp. 99–107, 2000, doi: 10916700.

[23] K. P. Dial, “Avian Forelimb Muscles and Nonsteady Flight: Can Birds Fly without Using the Muscles in Their Wings?,” *American Ornithological Society*, vol. 109, no. 4, pp. 874–885, 1992.

[24] B. W. Tobalske, “Neuromuscular control and kinematics of intermittent flight in the European starling (Sturnus vulgaris),” *J Exp Biol*, vol. 198, pp. 1259–73, 1995.

[25] L. A. Degernes and A. Feduccia, “Tenectomy of the Supracoracoideus Muscle to Deflight Pigeons (Columba livia) and Cockatiels (Nymphicus hollandicus),” *J Avian Med Surg*, vol. 15, no. 1, pp. 10–16, 2001, doi: 10.1647/1082-6742(2001)015.

[26] A. J. Sokoloff, J. Gray-Chickering, J. D. Harry, S. O. Poore, and G. E. Goslow Jr., “The function of the supracoracoideus muscle during takeoff in the European starling (Sternus vulgaris): Maxheinz Sy revisited,” *New Perspectives on the Origin and Early Evolution of Birds: Proceedings of the International Symposium in Honor of John H. Ostrom*, pp. 319–332, 2001.

[27] M. E. Deetjen, A. A. Biewener, and D. Lentink, “High-speed surface reconstruction of a flying bird using structured light,” *Journal of Experimental Biology*, vol. 220, no. 11, pp. 1956–1961, Jun. 2017, doi: 10.1242/jeb.149708.

[28] M. E. Deetjen and D. Lentink, “Automated calibration of multi-camera-projector structured light systems for volumetric high-speed 3D surface reconstructions,” *Opt Express*, vol. 26, no. 25, pp. 33278–33304, 2018, doi: 10.1364/OE.26.033278.

[29] D. D. Chin and D. Lentink, “How birds direct impulse to minimize the energetic cost of foraging flight,” *Sci Adv*, 2017.

[30] B. J. Hightower, R. Ingersoll, D. D. Chin, C. Lawhon, A. F. Haselsteiner, and D. Lentink, “Design and analysis of aerodynamic force platforms for free flight studies,” *Bioinspir Biomim*, vol. 12, no. 6, p. 064001, 2017, doi: 10.1088/1748-3190/aa7eb2.

[31] D. Lentink, A. F. Haselsteiner, and R. Ingersoll, “In vivo recording of aerodynamic force with an aerodynamic force platform: from drones to birds,” *J R Soc Interface*, vol. 12, no. 104, p. 20141283, 2015, doi: 10.1098/rsif.2014.1283.

[32] D. D. Chin and D. Lentink, “Birds repurpose the role of drag and lift to take off and land,” *Nat Commun*, vol. 10, no. 1, pp. 1–10, 2019, doi: 10.1038/s41467-019-13347-3.

[33] M. E. Deetjen, D. D. Chin, and D. Lentink, “The aerodynamic force platform as an ergometer,” *Journal of Experimental Biology*, p. jeb.220475, 2020, doi: 10.1242/jeb.220475.

[34] T. A. McMahon, *Muscles, Reflexes, and Locomotion*. Princeton University Press, 1984.

[35] T. Wolf and R. Konrath, “Avian wing geometry and kinematics of a free-flying barn owl in flapping flight,” *Exp Fluids*, vol. 56, no. 28, pp. 1–18, 2015, doi: 10.1007/s00348-015-1898-6.

[36] C. P. Ellington, “The Aerodynamics of Hovering Insect Flight. III. Kinematics,” *Philosophical Transactions of the Royal Society B*, vol. 305, pp. 41–78, 1984.

[37] R. Ingersoll, L. Haizmann, and D. Lentink, “Biomechanics of hover performance in Neotropical hummingbirds versus bats,” *Sci Adv*, vol. 4, no. 9, 2018, doi: 10.1126/sciadv.aat2980.

[38] J. W. Kruyt, E. M. Quicazan-Rubio, G. F. van Heijst, D. L. Altshuler, and D. Lentink, “Hummingbird wing efficacy depends on aspect ratio and compares with helicopter rotors,” *J R Soc Interface*, vol. 11, no. 99, pp. 20140585–20140585, 2014, doi: 10.1098/rsif.2014.0585.

[39] K. E. Crandell and B. W. Tobalske, “Aerodynamics of tip-reversal upstroke in a revolving pigeon wing,” *Journal of Experimental Biology*, vol. 214, no. 11, pp. 1867–1873, 2011, doi: 10.1242/jeb.051342.

[40] J. R. Usherwood, “Dynamic pressure maps for wings and tails of pigeons in slow, flapping flight, and their energetic implications,” *Journal of Experimental Biology*, vol. 208, no. 2, pp. 355–369, 2005, doi: 10.1242/jeb.01359.

[41] C. H. Greenewalt, “The Wings of Insects and Birids as Mechanical Oscillators,” *Proc Am Philos Soc*, vol. 104, no. 6, pp. 605–611, 1960.

[42] M. W. Bundle, K. S. Hansen, and K. P. Dial, “Does the metabolic rate-flight speed relationship vary among geometrically similar birds of different mass?,” *Journal of Experimental Biology*, vol. 210, no. 6, pp. 1075–1083, 2007, doi: 10.1242/jeb.02727.

[43] D. Lentink, “Accurate fluid force measurement based on control surface integration,” *Exp Fluids*, vol. 59, no. 22, pp. 1–12, 2018, doi: 10.1007/s00348-017-2464-1.

[44] B. W. Tobalske, L. A. Puccinelli, and D. C. Sheridan, “Contractile activity of the pectoralis in the zebra finch according to mode and velocity of flap-bounding flight,” *J Exp Biol*, vol. 208, no. 15, pp. 2895–2901, 2005, doi: 10.1242/jeb.01734.

[45] P. H. C. Eilers, “A perfect smoother,” *Anal Chem*, vol. 75, no. 14, pp. 3631–3636, 2003, doi: 10.1021/ac034173t.

[46] C. Van Den Berg and J. M. V. Rayner, “The moment of inertia of bird wings and the inertial power requirement for flapping flight,” *J Exp Biol*, vol. 198, pp. 1655–64, 1995.

[47] A. M. B. Robertson and A. A. Biewener, “Muscle function during takeoff and landing flight in the pigeon (Columba livia),” *Journal of Experimental Biology*, vol. 215, no. 23, pp. 4104–4114, 2012, doi: 10.1242/jeb.075275.

[48] R. L. Marsh, “Speed of sound in muscle for use in sonomicrometry,” *J Biomech*, vol. 49, no. 16, pp. 4138–4141, 2016, doi: 10.1016/j.jbiomech.2016.10.024.

[49] R. M. Alexander, *Animal Mechanics*, 2nd ed. London: Blackwell Scientific, 1983.

[50] D. B. Baier, S. M. Gatesy, and K. P. Dial, “Three-Dimensional, High-Resolution Skeletal Kinematics of the Avian Wing and Shoulder during Ascending Flapping Flight and Uphill Flap-Running,” *PLoS One*, vol. 8, no. 5, 2013, doi: 10.1371/journal.pone.0063982.

[51] A. K. Stowers, “Avian Inspired Morphing Wings,” Stanford University, 2017.

[52] M. Millard, T. Uchida, A. Seth, and S. L. Delp, “Flexing Computational Muscle: Modeling and Simulation of Musculotendon Dynamics,” *J Biomech Eng*, vol. 135, no. 2, p. 021005, 2013, doi: 10.1115/1.4023390.

[53] C. H. Greenewalt, “Dimensional relations for flying animals,” *Smithsonian Miscellaneous Collections*, vol. 144, no. 2, pp. 1–46, 1962, doi: 10.4324/9780203476154_chapter_13.

[54] D. L. Altshuler *et al.*, “Neuromuscular control of wingbeat kinematics in Anna’s hummingbirds (Calypte anna),” *Journal of Experimental Biology*, vol. 213, no. 14, pp. 2507–2514, 2010, doi: 10.1242/jeb.043497.

[55] E. R. Donovan, B. K. Keeney, E. Kung, S. Makan, J. M. Wild, and D. L. Altshuler, “Muscle Activation Patterns and Motor Anatomy of Anna’s Hummingbirds Calypte anna and Zebra Finches Taeniopygia guttata,” *Physiological and Biochemical Zoology*, vol. 86, no. 1, pp. 27–46, 2013, doi: 10.1086/668697.

[56] T. L. Hedrick, J. R. Usherwood, and A. A. Biewener, “Wing inertia and whole-body acceleration: an analysis of instantaneous aerodynamic force production in cockatiels (Nymphicus hollandicus) flying across a range of speeds,” *J Exp Biol*, vol. 207, no. 10, pp. 1689–1702, 2004, doi: 10.1242/jeb.00933.

[57] B. E. Jackson, B. W. Tobalske, and K. P. Dial, “The broad range of contractile behaviour of the avian pectoralis: functional and evolutionary implications,” *Journal of Experimental Biology*, vol. 214, no. 14, pp. 2354–2361, 2011, doi: 10.1242/jeb.052829.

[58] B. W. Tobalske, A. A. Biewener, D. R. Warrick, T. L. Hedrick, and D. R. Powers, “Effects of flight speed upon muscle activity in hummingbirds,” *Journal of Experimental Biology*, vol. 213, no. 14, pp. 2515–2523, 2010, doi: 10.1242/jeb.043844.

[59] B. W. Tobalske, B. E. Jackson, and K. P. Dial, “Ontogeny of flight capacity and pectoralis function in a precocial ground bird (alectoris chukar),” *Integr Comp Biol*, vol. 57, no. 2, pp. 217–230, 2017, doi: 10.1093/icb/icx050.

[60] D. D. Chin and D. Lentink, “Fluid moment and force measurement based on control surface integration,” *Exp Fluids*, vol. 61, no. 1, pp. 1–19, 2020, doi: 10.1007/s00348-019-2838-7.